Molecular dynamics simulation of structures and interfaces in amorphous/ordered composites

by

Katherine M. Sebeck

A dissertation submitted in partial fulfillment
of the requirements for the degree of
Doctor of Philosophy
(Materials Science and Engineering)
in the University of Michigan
2015

Doctoral Committee:

Professor John Kieffer, Chair
Professor Brian J. Love
Assoc. Professor Verra Sundaragaven
Professor Anthony Waas

Acknowledgments

Thank you to my ever-patient husband and family

Thank you to Professor Kieffer, Dr.Arun Uphadyay, Dr. Michael Aldridge, Mike Waters and all of the other members of the group over the years who have been there to teach and support.

Many thanks to Brock Palen, Andrew Caird, Bennet Fauber and everyone else in the CAEN CAC offices, without whom I would have spent many more hours compiling code instead of running it.

This research was made with Government support under and awarded by DoD, Air Force Office of Scientific Research, National Defense Science and Engineering Graduate (NDSEG) Fellowship, 32 CFR 168a and Science, Mathematics and Research for Transformation Defense Scholarship for Service Program (SMART). Xsede allocation #TG-DMR140036 was also used in support of this document.

Table of Contents

List of Figures

List of Tables

List of Appendices

List of Abbreviations

Abbreviation	*Meaning*
DGEBF	Diglycidyl ether of bisphenol F
DETA	Diethylene triamine
TETA	Triethylene teramine
LJ	Lennard-Jones
SICA	Size increasing clster analysis
ISS	Interfacial shear strength
MD	molecular dynamics
MC	Monte Carlo
DETDA	diethyltoluene diamine
DMM	Dynamical matrix method
pcf	pair correlation function
N20	Primary amine, unreacted
N21	Primary amine, reacted once
N1	Secondary amine, unreacted
N0	Fully reacted amine
CAR	Aromatic carbon
OPLS	Optimized potential for liquid simulations
NMR	Nuclear
DDS	3,3'-diaminodiphenyl sulfone
COMPASS	Condensed-phase optimized molecular potentials for atomistic simulation studies

PCFF	polymer consistent force field
CVFF	Consistent valence force field
NPT	Constant number, pressure and temperature
NVT	Constant number, volume and temperature
NVE	Constant number, volume and engery
DFT	Density functional theory
EAM	Embedded atom method
FCC	Face centered cubic
AMBER	Assisted Model Building with Energy Refinement
PAN	polyacrylonitrile
DCPD	Dicyclopentadiene
PMC	Polymer matrix composites
QM	Quantum mechanical
MM	Molecular mechanics
LAMMPS	Large
FFAT	Fourier Filtering of Atomic Trajectories

List of Symbols

Abbreviation	*Meaning*
$\langle r \rangle$	Mean coordination number
f	Functionality
N	Number of atoms
ρ	Density
σ_{ij}	Extent of soft-core repulsion OR stress
ε	Pair non-bonded interaction strength
K	Bulk modulus
E	Young’s Modulus
z	Elemental valency
M’	Longitudinal modulus
p_c	Critical extent of reaction
G	Shear modulus
r_{ij}	Interatomic distance
f_{ij}	Interatomic forces for atoms of type i and j
m	Mass
T_g	Glass transition temperature
k_b	Boltzmann’s constant
q	Partial charge
Q^n	Bridging oxygen coordination number

Abstract

This thesis describes molecular dynamics simulation studies of the structure-property relationships of molecular network systems, including inorganic and organic bulk amorphous systems, as well as two different amorphous polymers at the interface with ordered substrates.

A series of soda lime silicate glasses were simulated, with up to 50% total modification and varying ratios of sodium and calcium. The clustering of cations and second-neighbor connectivity affect vibrational modes and the compressibility vs. pressure behavior. Mean-field theory is unable to account for mixed modifier effects in soda lime silicates.

The structure and tensile behavior of a dynamically reacted bulk epoxy network were studied, demonstrating an improved polymerization method for continuously monitoring properties as a function of network growth, including volumetric shrinkage and internal stresses. A bifunctional epoxy resin is reacted with two aliphatic amines at room temperature, comparing simulation size, amine functionality, and stoichiometry. The elastic properties change by only 1-2 GPa during the growth of the network within the achieved degree of conversion. Tensile strength increases by ~100 MPa. Systems with surplus amine hardener reach higher degrees of epoxide conversion, but lag in formation of an infinite network.

As a simple model system for amorphous/ordered interfaces, a thin alkane film was placed onto a metallic substrate. The ordered substrate creates a layered polymer configuration within the adjacent 10 Å, as shown by density profiles, pair correlation functions, and monomer orientation statistics. This structural change also affects the mechanical properties, as the elastic moduli of nanoconfined alkane systems are higher than would be expected for a simple laminate composite, based on extrapolating from the bulk properties of the two materials.

Lastly, epoxy/carbon laminate systems were investigated, comparing different epoxy layer thicknesses and amine functionality. The cure and shrinkage behavior mimick the bulk epoxy, though the percolation of an infinite cluster is delayed. Post-annealed structures show a nearly uniform decrease in both the elastic modulus and tensile strength.

Local heterogeneity is important in predicting nanoscale mechanics for all systems investigated. Larger system size provides better accuracy in determining mechanical properties of simulated highly cross-linked network polymers.

Chapter 1. Background and Introduction

1.0. Introduction to amorphous structures and interfacial interactions

Composite materials are becoming increasingly critical to meeting performance targets in weight-sensitive applications, such as the upcoming CAFE standards for the automotive industry, or the TARDEC 30 year strategy for ground vehicles in the Army. However, in many cases, the matrix behavior in the composite cannot be accurately modeled using bulk properties alone, particularly in close proximity to reinforcing materials. Polymer matrix composites properties are typically limited by the behavior at the interface and the polymer region just beyond, often termed the interphase. Prior experimental work in the Kieffer group has demonstrated the polymer matrix near fiber reinforcement has a lower modulus than the same polymer in the bulk.[1] However, concurrent Raman scattering shows no evidence of either chemical inhomogeneities or residual stresses. Therefore, it becomes evident that there must be some alternative mechanism driving this change.

For the sake of this body of work, only simple planar, non-chemically bonded interfaces have been considered. Industrially, sizing and other fiber treatments are used to improve bonding. However, the understanding of interfacial structures at the nanoscale remains poor, even for the simplified case. Molecular dynamics simulations are particularly well suited for examining structures of this type and length scale. Quantum methods, such as density functional theory, are limited to hundreds of atoms, and despite recent advances, it is still limited in its ability to predict van der Waals interactions.[2] Molecular dynamics simulations regularly reach ten of thousands of atoms, and tens of nanometers in each dimension. By combining traditional molecular dynamics with stochastic methods, it is also possible to access time scales relevant to cure, though viscous relaxation remains beyond the effective reach of such methods.

Realistic modeling of composite materials requires not only an understanding of the behavior of each component, but of the nature of the interface and relationships between them.[3] Between two ordered materials, this can be described by lattice mismatch and orientation. When one or more component is amorphous, the key characteristics are less obvious. By first seeking to understand the relationship between amorphous structures and mechanics, we ultimately expect to understand how amorphous structures change in the presence of an ordered surface, and the corresponding effects on mechanics. Accordingly, this introduction will address theories of amorphous networks, as well as background regarding interfaces.

1.1. Introduction to Amorphous Networks

Theories of amorphous networks have evolved largely independently in polymer and inorganic glass science. The continuous random network model proposed by Zachariasen in 1932 has been the fundamental basis for much of modern theory in glass science.[4] Flory and Stockmayer's work in the 1940's is considered the origin of network theory as it applies to polymer science.[5-11]

In this thesis, we consider both rubbery and glassy polymer systems, as well as inorganic oxide glasses. While all glassy networks are amorphous, not all amorphous materials are considered glassy, based on the thermomechanical properties. We consider only those materials with a continuous random network of crosslinks as glassy, rather than those materials that derive their strength primarily through entanglements, which we will consider as rubbery.

Inherent to network theory is the idea of the network unit. In oxide glasses, this is a small arrangement of atoms, such as the SiO_4 tetrahedra or BO_3 trigonal planar structures. In polymer systems, the network unit is the monomer, which can be anywhere from 6 atoms, like ethylene, to hundreds or thousands of atoms in some block copolymers. In oxide glasses, the bonds between network units are almost universally reversible with temperature, while in most glassy polymers, such as epoxy, the bonds between network units are permanent. The description of networks mathematically is often considered within the framework of graph theory, which refers to the network units as "nodes" and the bonds between them as "edges". This is a useful method for examining the relationships between objects, as it provides a quantitative framework for discussion.

The experimental techniques for analyzing amorphous materials have evolved, in turn advancing our understanding of amorphous structures. X-ray diffraction (XRD) in amorphous materials is only able to reveal pair-pair distance information for the first few angstroms, but the lack of order is itself fundamental to the development of models of amorphous networks, particularly for inorganic glasses. [12-14] Modern improvements in detectors have expanded our view to examine behavior beyond the nearest-neighbor shells.[15-20] This has been important for developing our understanding of the medium-range structural features in glasses. In polymer science, x-ray methods have been used to identify molecular structures in the crystalline form, though the size of the network unit limits the ability to probe larger networks with XRD. Nuclear magnetic resonance spectroscope (NMR) is one of the most common methods for identifying short range structures in glasses.[21-28] NMR is equally important to the understanding of the behavior of polymer networks, and provided the evidence for entanglement.[29,30]

Spectroscopic methods, particularly infrared and Raman, can be used to monitor progression of the polymerization, by measuring the populations of specific functional groups, as well as the network strain based on shifts in peak position.[31,32] In glasses, optical spectroscopy frequencies have been highly fruitful for structural characterization.[33-40] However, fully deconvoluting the underlying structural features, particularly those associated with network modes, is difficult without coupling to other methods, mainly computer simulation.

Simulations methods, such as molecular dynamics and Monte Carlo, have been important in the development of network theory in glasses, from early simulations by Fox and Anderson, to the works of Micolaut, Boal and many others.[41-48] Simulation allows for direct counting of the population of structural moieties, and it has the ability to tune variables that are not independently accessible in experiments, so as to help differentiate the underlying causes. It is also possible to look at the local structure in amorphous materials more specifically than typically possible using experiments. Work has also been done in *ab initio* MD, including work to verify and interpret data from solid state NMR. [49-54]

The two fields of polymer and glass science have approached the description of the amorphous network from different directions, but have begun to converge on common questions and a shared framework. Concerning inorganic glass one has classically been concerned with the 'fragility' of the glass-forming liquid, i.e., the deviation from Arrhenius behavior during cooling, which strongly affects processability.[55] Theory in polymer science has typically been developed first from idealized model systems, with a growing progression toward realistic systems. For polymer science, process control is contingent upon the viscosity of the system, and the critical transition at the gelation point. Because the minimum network unit of a polymer is most complex, empirical models have dominated, typically based on the Flory-Stockmayer model outline by Stockmayer in 1943. [11] Ultimately, both are concerned with predicting the behavior of an infinite, amorphous network.

Inorganic glass theory

An immense body of work has been devoted to understanding the structure-property relationships in oxide and chalcogenide glasses. The continuous random network model proposed by Zacariasen in 1932 has been the basis of many of these models.[4] Models for network theory in glasses typically fall into two categories: mean-field based theories, which identify average network unit behavior, or theories based on the dynamical matrix methods (DMM), wherein the eigenvalues of the adjacency matrix are calculated based on the assumption of harmonic motion. However, most commercial glasses are multicomponent oxide glasses, mixing both network units and modifier cation species to regulate processing conditions. These modifier cations contribute towards network rigidity via strong non-bonding Coulomb interactions. This complicates the description of governing forces and necessitates large systems sizes for a full description, especially considering that mixed cation compositions can lead to local inhomogeneities. Consequently, much of the work in this area has focused on improving the mean-field model proposed by Thorpe and Phillips to predict the glass-forming quality as a function of chemical composition.[56-58]

This initial model for rigidity percolation used a body-bar (*i.e.*, ball and stick) network structure, computing the mean coordination of network units in systems without dangling bonds (i.e., chalcogenides) by Maxwell constraint counting to predict the fraction of zero frequency (floppy) modes. [57] The critical value of $\langle r\rangle=2.4$ was found for the mean coordination in such networks. However, the introduction of dangling bonds, such as the terminal non-bridging oxygen atoms present in many oxide glasses, presents a challenge for the basic constraint counting. The introduction of the pebble game algorithm for exploring subgraphs was one strategy, though it is not automatically generalizable to three dimensions.[58] Another method by Aramov *et.al.* was to calculate an average number of constrained bonds, where the maximum number of possible constraining bonds is reduced by the number of dangling bonds.[59]

In order to address issues of localized inhomogeneities, Maxwell constraint counting was expanded to examine medium-range ordering effects by applying constraint counting to a series of increasingly large clusters. This method is conveniently called the Size Increasing Cluster Approximation, henceforth referred to as SICA.[45] The base level of this analysis, with the minimal cluster size, is equivalent to the mean-field approximation. This modification also addresses the ring buckling mechanism, which may be a fundamental cause of the anomalous bulk modulus behavior observed in silica.[60,61]

Treatment of the cations in network modified silicates remains a difficult but critical question. Network modifiers are necessary for control over melt temperature, optical coefficients and elastic constants, as well as color and other commercially important properties. Because these compounds have unclear non-equivalent site coordination environments, their role in the network can be ambiguous, and it would be an over-simplification to assume valence bonding to the dangling oxygen atoms.[48,62,63]

However, it is noted that bond counting alone cannot accommodate the difference in bonding strength between Si-O and X^+-O. Instead of looking at a specific system, Wyart looked at elasticity in a two-dimensional harmonic spring network.[64] To differentiate from traditional rigidity percolation models, a fraction of “weak” springs are added, which while trivially rigid, have an effect on stability. This use of weak and rigid bonds may be able to better account for the behavior of cations, which can be treated as only weakly affecting the oxygen anions. This approach may also be able to better accommodate mixed cation effects.

The mixed glass former effect has been somewhat addressed in the context of chalcogenide glasses, but has not been explored in depth for oxide glasses. In part, simulations of multicomponent oxide glasses remains a difficult challenge. However, as improved NMR data becomes available to verify simulations for systems like borosilicate, it is anticipated that further modifications to the mean-field theory will be needed. Moreover, techniques such as SICA will become increasingly critical for accommodating the non-random distribution of network units. [21,65-70]

Mean field constraint theory has been effective in predicting compositions that will be good glass formers. However, the treatment of network modifying cations and mixed network former effects remains problematic. Looking beyond the first neighbor environment with such methods as SICA and considering medium range order has improved the predictive power of these models, but more complex compositions require further work.

Polymer network theory

In polymer systems, the network unit, more commonly called the monomer, is more complex than the network units of inorganic glasses. Disruption of the network is similarly more complex, with steric hindrance as a primary mechanism, rather than network scission via modifying cations. Network theory in polymers has traditionally emphasized connectivity percolation and the growth and distribution of molecular weights. This is then coupled to other models for mechanical properties, rather than using networks to directly predict these behaviors. Polymer systems are further complicated by bond irreversibility, intermolecular bonding, entanglement, effective chain length, and growth mechanisms (e.g., step-growth vs condensation polymerization). This subject has been thoroughly reviewed, and this section will instead focus on those systems which are most informative to highly cross-linked network theory.[71,72]

The Flory-Stockmayer (FS) model is as fundamental to polymer network science as the Zachariasen continuous-random network model is to glass science. Flory introduced theories for gelation in the late 30s and early 40s in a series of papers.[5-10] Flory was among the first to attempt to predict the critical gelation point, where an "infinite' network has been formed. Building on the theories introduced by Flory, Stockmayer derived theories of molecule size distribution and gel formation for various mixed monomer cases.[11] However, in all cases, two major assumptions were made: first, intramolecular (i.e., ring forming) reactions were prohibited, and second, all unreacted functional groups are considered to be equally reactive. These assumptions do prove to be effective in many cases, but even common reactions like two-part epoxies don't conform.

The primary assumptions of the FS model have been tackled by many researchers. The rate of gelation and glass transition temperature have been shown to be overestimated by the equal reactivity assumption.[73] This assumption also fails to predict crosslink density, neglecting the possibility of the formation of long chains, which crosslink later. The distribution of these lengths is important for mechanical behavior and solvent swelling.[74-77] Ring formation was addressed by Ahmad-Rolfes-Stepto glation theory with the introduction of a ring forming parameter, which compensates for the formation of links that do not increase molecular weight.[78,79]

Branching theories are one method of predicting the growth and development on network structures, used in Flory's early papers on the subject.[8,9] These theories were expanded to address the issue of elasticity by Dobson and Gordon.[80,81] They defined a subset of the network termed "elastically activated network chains," which has been used to predict vulcanization of several rubbers and the average chain length, and in turn can be used in swelling and other mechanical predictions.

As in inorganic glasses, an early approach was to use the dynamic matrix method to analyze elastic properties in a random percolating network.[82] Instead of using DMM, others have tried using Monte Carlo methods to study both connectivity and rigidity percolation as a function of polymer fractions in a 2D polymer-fluid network.[83] In this model, holes in the network are considered to be filled with fluid, and hence show a resistance to deformation. Beads are bound by either fluid or polymer tethers, with the fluid tethers having variable connectivity. Additionally, the volume of the beads is explicitly considered, unlike in most inorganic network theory calculations, which do not consider the volume of the nodes, only the connectivity.

The nature of bonding in polymer networks is particular challenge, as crosslinks may or may not be able to freely rotate, or be subject to bond bending forces.[84-86] Directly comparing fixed and freely rotating crosslinks, rigidity percolation was found to depend on the nature of the crosslink, with a lower threshold of connectivity for stiff cross-links than for free hinge links.[86] This is expected, as the number of degrees of freedom is lower in a system of fixed crosslinks, requiring fewer additional constraints to reach a rigidly constrained system.

The relationship between rigidity percolation and fracture has also been discussed for some polymer systems.[87] In this model, the Young's modulus is related to the lattice bond fraction, p, by $E \sim [p - p_c]^{\tau}$ where p_c is the critical percolation threshold and τ is the vector percolation exponent. This method, however, neglects the variation in scaling classes found for varying bonding behavior,[84] instead assuming the elasticity scaling found by DMM.[82] This discussion was further extended to discuss critical stress for fracture, and on identifying different fracture regimes, e.g., disentanglement, bond rupture and strain hardening, as a function of molecular weight, density and other commonly available data.

It is clear that rigidity in polymer networks is a more complex issue than glass networks due to the variability of networking units, but significant advances have been made. Ultimate mechanical properties are important in polymeric systems, and the ability to predict critical properties, such as shifting glass transition temperatures, can be valuable in monitoring reactions. However, sensitivity to the lattice used to build the network, hinge model at nodes, and reactivity of different functional groups mean that a general model is far from being developed.

Challenges for a unified network theory

A major challenge for a unified network theory is how to quantitatively characterize the different bonding mechanisms in an efficient way. For polymer systems, the hybridization of carbon bonds can result in a fixed hinge instead of a freely rotating link. Inorganic systems need to differentiate between the covalent bonding of the network backbone and the ionic bonding between dangling anions and cations.

Another hurdle is how to treat medium-range ordering and self-organization, particularly in more complex polymer systems. The two best suited methods seem to be size increasing cluster analysis and branching theory. These have many similarities, though the simpler network unit and uniform reactivity of inorganic glasses allows for a more precise prediction of the probabilities of various configurations. The Maxwell constraint counting used in the SICA method could be logically extended to better predict the mechanical properties of medium-range clusters within polymer structures, particularly in systems driven by self assembly mechanisms.

Atomistic simulations are a key method for improving our understanding of amorphous network mechanics. The ability to precisely enumerate the number of units and bonds is critical to validating these models. However, it is important that the mechanical properties derived from simulation be carefully validated against experimental behavior. Both polymer networks and inorganic glasses are challenging to accurately simulate, but continuing advances in hardware and algorithm have improved computational models of densely linked amorphous networks.

1.2. Introduction to interfacial theory

Composite material behaviors are innately dependent on the properties at the interface.[88] However, in addition to issues of wetting and adhesion, prior work in polymer matrix composites has shown that the matrix behavior near the interface may not match that of the bulk, a phenomenon attributed to the development of a so-called interphase.[89-102] Significant work has been done to mechanically characterize these interfaces. However, the underlying structure-property relationships associated with the interphase for planar, non-chemically bonded interfaces are not well known. In this introduction we discuss various experimental techniques for characterizing interfaces, as well as prior work in mechanics of interphases and simulations of interfaces between dissimiliar materials.

Experimental limitations in interfaces

One major challenge in the study of interfaces is geometry: these features are fundamentally buried within the sample. By mechanically removing one side or the other, artificial relaxation or other deformation mechanisms may be induced, and essentially, it becomes a study of a surface. Furthermore, many composite structures of interest occur at the boundary between ordered and disordered structures, with the more significant structural changes occurring in the disordered component. Experimental characterization of amorphous materials at length scales between nearest atomic neighbors and the bulk remains an experimental challenge.

One common method to investigate the nature of the interface is the deposition of monolayer structures on a substrate. The body of work on monolayers, particularly in the context of self-assembly, is substantial.[103] However, prior work has shown that the interphase can extend well beyond this first deposition layer. [89-102]

Spectroscopy, particularly Raman spectroscopy, is a frequently used technique for examining the chemistry at interface, and local structural changes, such as ring stretching.[104-108] One variant, surface-enhanced Raman, relies on electromagnetic enhancements, and is a valuable tool for studying nanostructured materials, though it cannot probe buried interfaces particularly well.[107] Another strategy is to use focusing optics to probe only the interface or interphase region of a sample.[1] However, the resolution of light spectroscopy is almost always limited by the focusing optics and the wavelength of the light, though techniques exist to achieve resolution below the diffraction limits. Information learned for micron scale light spectroscopy has been invaluable to our work, but cannot tell the complete story alone.

For crystalline structures and interfaces, x-ray and other diffraction methods are superb. However, in the investigation of disordered materials, it is a more difficult technique. Grazing incidence small angle x-ray scattering (GISAXS) is one of the more powerful experimental tools for analyzing polymer thin films, and has been used to study self assembly.[109-111] However, the complexity of the associated analytical solutions have limited the application of the GISAXS technique. X-ray photoelectron spectroscopy is a surface-sensitive technique for examining chemistry often used to characterize the components of a composite system, but it reveals little structural information, and cannot analyze buried interfaces.[112-118]

Another indirect analysis commonly used is to evaluate changes in the glass transition temperature as a function of film thickness or probe depth. [119-126] While a reduction in T_g as a function of thickness was shown first in polystyrene, this phenomenon has since been explored for other polymers. Notably, it is not strongly dependent on the molecular weight, but the trend instead seems primarily influenced by the favorability of the substrate. Various models have been proposed to describe this change in glass transition temperature, both for free standing films and thin polymer films on a substrate.[121,122] For example, one model presented by *Kim et. al.* uses a continuous multilayer model assumption with a fitting parameter to describe the non-monotonic rate of change as a function of thickness.Is called for, unless it is the same as previous sentence, but then start this sentence to indicate that

Mechanics of interfaces

In composite materials, reinforcement comes in a wide variety of shapes, sizes, and orientations. This includes particles, fibers, sheets, random mats of fiber, woven mats of fiber and many others. Particles can be spherical, cylindrical, faceted, or rough. Fibers also come in many geometries, not just simple cylinders. All of this means the mechanical description of composite behavior can be quite complicated.

In order to simplify the question of mechanics, the interfaces explored in this study are all planar laminates. Accordingly, the compliance tensor can be reduced to the set presented below [88]:

$$S_{ij} = \begin{bmatrix} \frac{1}{E_{11}} & \frac{-\upsilon_{12}}{E_{11}} & \frac{-\upsilon_{13}}{E_{11}} & 0 & 0 & 0 \\ \frac{-\upsilon_{21}}{E_{22}} & \frac{1}{E_{22}} & \frac{-\upsilon_{23}}{E_{122}} & 0 & 0 & 0 \\ \frac{-\upsilon_{31}}{E_{33}} & \frac{-\upsilon_{32}}{E_{33}} & \frac{1}{E_{33}} & 0 & 0 & 0 \\ 0 & 0 & 0 & \frac{1}{2\mu_{23}} & 0 & 0 \\ 0 & 0 & 0 & 0 & \frac{1}{2\mu_{13}} & 0 \\ 0 & 0 & 0 & 0 & 0 & \frac{1}{2\mu_{12}} \end{bmatrix}$$

Eq. 1.1 Compliance tensor for a planar laminate

For the sake of this investigation, the primary emphasis will be on the elastic response perpendicular to the interfacial plane. This geometry is expected to most clearly demonstrate potential effects of an interphase region. However, it inhibits the ability to study interlaminar shear strength and adhesion. Due to the limits of available resources and prior experimental results, a focus on the interphase was chosen.

The interphase was proposed as a mechanism to explain the deviation of transverse Young's moduli from the values predicted by the rule of mixtures within the Reuss and Voigt bounds.[92-94,97] The thickness of the interphase has been predicted anywhere from 30nm to 3µm, depending on the experimental technique. Experimental characterization of this region in polymer matrix composites is challenging for mechanical properties, as well as previously discussed structural characteristics.[1,3] Common techniques like micro-indetentation can result in pile-up at the interface, making it more difficult to determine the exact volume of material displaced. Non-contact light scattering techniques such as micro-Brillouin are only possible on certain materials, requiring transparency of the sample. The transition between nano- and micro- scale interphase models also remains a significant challenge in modeling these behaviors.

At the continuum scale, a number of models have been developed to describe interphase mechanics.[89-92,94,96-102] Many models have focused on the fracture mechanics, but typically address elastic properties as well.[94] The basic interphase is frequently modeled as a nonhomogeneous region, with properties varying through the thickness, while the matrix and fiber are modeled as isotropic. This is defined by an exponential scaling factor, where the interphase modulus is given by

$$E_{\text{int}} = E_0 e^{\beta x}$$

Eq. 1.2 Example interphase modulus model

where E_o and β are constants empirically determined from the geometry and stiffness properties, and x is the distance from the interface. This model assumes that the boundary conditions at the interfaces between the matrix and fiber are continuously defined, limiting the effective modulus of the interphase to a value between the moduli of two materials. Other models have been developed that do not make these assumptions of continuous boundary condition, allowing the interphase to be the softest material. A stiff interphase is preferable for improved stress transfer and inhibiting water diffusion, but more prone to brittle failure.

The nanoscale interphase is a more discrete phenomenon, as is the nature of the length scale. This nanoscale interphase is driven by surface interactions and chain immobilization. In thermoplastics this effect can have a dramatic effect on entanglement and reptation dynamics. Jancar found the interphase thickness in such materials to be typically on the order of the radius of gyration of the polymer. [93] However, in a highly cross-linked polymer network, entanglement is no longer the dominant strengthening mechanism.

While the body of work in continuum mechanics models of the interphase is substantial, the work devoted to understanding the nanoscale interphase and underlying structural characteristics are less well studied. Simulation has been a major tool for understanding these phenomena, with finite element analyses for continuum mechanics, and mixture of atomistic methods, including molecular dynamics, Monte Carlo and molecular mechanics simulations, have been used to understand nanoscale interphase properties.

Prior work in interfacial simulations

Simulation of organic/inorganic interfaces has been explored for a wide variety of systems. Much like the experimental investigations of the interface, there has been a strong emphasis on the study of monolayer behavior.[127-133] There are also a number of investigations of confined organic layers, looking at metallic, oxide, and carbon substrates.[132,134-146] The last major category is embedded particles, such as oxide nanoparticles and carbon nanotubes.[147-151] These references are hardly an exhaustive list of the current literature, but rather, represent a cross-section of papers in the field.

There are common challenges to the simulation of dissimilar systems, regardless of the geometry. The selection of a force field is a major consideration in such simulations. Polymer systems typically use softer repulsion potentials, with explicit terms defining bond distance and bond angles. Oxides are typically very sensitive to Coulomb interactions, while metals are commonly simulated with tabulated potentials, such as the embedded atom method.[152] Consequently, finding a potential or combination of potentials to effectively describe a mixed system requires a certain amount of compromise. The most common strategy is to use the most appropriate potential model for each component, and use an additional set of parameters to specifically address the interactions between them. However, defining the interactions at the interface must be done carefully, as this can strongly impact the overall behavior of the composite.

Relaxation time presents another challenge in molecular dynamics simulations. Given a typical time step is on the order of 1-2 femtoseconds, simulations are typically in the nanosecond range of total time, while most viscous response times are on the order of milliseconds or longer. Careful construction of initial configurations and use of energy minimization is necessary to relax structures. As will be seen later, the presence of an ordered surface leads to some reconfiguration of the amorphous region. It is therefore critical to allow this to occur during structure generation, rather than assuming a free surface is equivalent to the interface surface.

Another issue, which will be explored in detail in later chapters, is the effect of system size. The film thickness has obvious effects on mechanical properties, as the interphase region become a larger fraction of the thickness. However, over-restriction of the system size in the two periodic directions can result in unrealistic self-interactions, particularly for long polymer chains. For highly networked amorphous networks, such as silicate glasses, insufficiently large systems can result in premature rigidity percolation and overestimation of mechanical properties.

1.3. Goals and Overview

This thesis has two primary goals: the first is the effective simulation and characterization of amorphous networks using molecular dynamics. Secondly, with this improved understanding of amorphous structures, to better understand the impact of an interface between ordered substrates and amorphous materials on the interfacial structure and mechanics. To this end, we will examine four types of systems: inorganic glasses, bulk cross-linked epoxy, alkane/metal laminates and epoxy/graphite laminates. We seek to correlate the structure with mechanical properties in all cases.

The inorganic glasses examined are a series of sodium silicate and soda lime silicate glasses. Structure and mechanical properties will be evaluated in terms of both the total degree of network modification and the mixture of network modifying species. Specifically, the vibrational properties of the network will be examined in detail, along with Young's and bulk moduli of different systems. These results will be discussed in terms of local heterogeneity and network theory where possible.

Continuing with bulk amorphous systems, a highly cross-linked polymer system was chosen for comparison, namely an epoxy resin with aliphatic amine hardeners. Aliphatic amines were chosen due to the low degree of shrinkage observed experimentally. Two functionalities are chosen for comparison, to investigate the role of amine connectivity in network development. The effect of system size and epoxy:amine stoichiometry on structural and mechanical properties are also explored for these systems as a function of cure.

As a simple model system for interfaces between ordered and amorphous materials, a series of alkane/metal laminate systems will be studied. Four FCC metals will be used, along with three alkane chain lengths. Additionally, the interaction strength between the alkane and metal will be varied for one metal/chain length combination. Ways to quantify structural changes at the interface will be explored, as well as the changes in mechanical properties between systems of a uniform chain length.

Lastly, a series of epoxy/graphite laminate systems are presented. The same resin/hardener system is used, again varying amine functionality and system size. The structure and mechanical properties are examined as a function of cure wherever feasible. This system is chosen due to the engineering importance of carbon fiber epoxy composites. Fiber sizing is beyond the scope of the current work. The fiber surface at the length scales of molecular dynamics, for PAN fibers, can be simplified as a series of planar graphene layers.[153-158]

Molecular dynamics simulations allow us to examine the relationships between structure and properties for different bulk amorphous and amorphous/ordered laminate systems at small length scales. By better understanding how the structure of a bulk amorphous network affects mechanical properties, and how that structure changes at an interface, we hope to better understand the nature of polymer matrix composites.

1.4. References

1. Aldridge M, Waas A, Kieffer J (2014) Spatially Resolved In-Situ Elastic Modulus of Thermoset Polymer Amidst Carbin Fibers in a Polymer Matrix Composite. Composites Science and Tehcnology 98:

2. Klimes J, Michaelides A (2012) Perspective: Advances and challenges in treating van der Waals dispersion forces in density functional theory. J Chem Phys 137: 120901.

3. Llorca J, Gonzalez C, Molina-Aldareguia JM, Segurado J, Seltzer R et al. (2011) Multiscale modeling of composite materials: a roadmap towards virtual testing. Adv Mater 23(44): 5130-5147.

4. Zachariasen WH (1932) The Atomic Arrangement in Glass. J Am Chem Soc 54(10): 3841-3851.

5. Flory PJ (1936) Molecular size distribution in linear condensation polymers. Journal of the American Chemical Society 58: 1877-1885.

6. Flory PJ (1939) Kinetics of Polyesterfication: A Study of the Effects of Molecular Weight and Viscosity on Reaction Rate. Journal of the American Chemical Society 61: 3334-3340.

7. Flory PJ (1940) Molecular Size Distribution in Ethylene Oxide Polymers. Journal of the American Chemical Society 62: 1561-1565.

8. Flory PJ (1941) Constitution of three-dimensional polymers and the theory of gelation. Eighteenth Colloid Symposium 132-140.

9. Flory PJ (1941) Molecular size distribution in three dimension polymers. I. Gelation. Journal of the American Chemical Society 63:

10. Flory PJ (1942) Random Reorganization of Molecular Weight Distribution in Linear Condensation Polymers. Journal of the American Chemical Society 64: 2205-2212.

11. Stockmayer WH (1943) Theory of Molecular Size Distribution and Gel Formation in Branched-Chain Polymers. J Chem Phys 11(2): 45.

12. Mozzi RL, Warren BE (1969) The structure of vitreous silica. J Appl Cryst 2(4): 164-172.

13. Mozzi RL, Warren BE (1970) The structure of vitreous boron oxide. J Appl Cryst 3(4): 251-257.

14. Warren BE, Mozzi RL (1966) Multiple scattering of X-rays by amorphous samples. Acta Cryst 21: 459.

15. Benedetti A, Geotti-Bianchini F, Fagherazzi G, Riello P, Albertini G et al. (1994) SAXS study of the micro-inhomogeneity of industrial soda lime silica glass. Journal of Non-Crystalline Solids 167: 263-271.

16. Greaves GN (1985) EXAFS and the structure of glass. Journal of Non-Crystalline Solids 71: 203-217.

17. Biscoe J (1941) X-ray study of soda-lime-silica glass. Journal of The American Ceramic Society 24: 262-264.

18. Medda MP, Musinu A, Piccaluga G, Pinna G (1993) Na+ coordination in sodium diborate and triborate glasses with x-ray diffration. Journal of Non-Crystalline Solids 162: 128-135.

19. Gaskell PH (2005) Medium-range structure in glasses and low-Q structure in neutron and X-ray scattering data. Journal of Non-Crystalline Solids 351: 1003-1013.

20. Warren BE, Biscoe J (1938) THE STRUCTURE OF SILICA GLASS BY X-RAY DIFFRACTION STUDIES*. Journal of the American Ceramic Society 21: 49-54.

21. Gee B, Eckert H (1996) Cation Distribution in Mixed-Alkali Silicate Glasses. NMR Studies by 23Na-{7Li} and 23Na-{6Li} Spin Echo Double Resonance. The Journal of Physical Chemistry 100: 3705-3712.

22. Maewaka H, Maewaka T, Kawamura K, Yokokawa T (1991) The structural groups of alkali silicate glasses determined from 29Si MAS-NMR. Journal of Non-Crystalline Solids 127: 53-64.

23. Jones AR, Winter R, Greaves GN, Smith IH (2001) MAS NMR study of soda-lime-silicate glasses with variable degree of polymerisation. Journal of non-crystalline solids 293: 87-92.

24. Maekawa H, Yokokawa T (1997) Effects of temperature on silicate melt sructure: A high temperature 29Si NMR study of Na2Si2O5. Geochimica et cosmochimica acta 61: 2569-2575.

25. Dupree R, Holland D, McMillan PW, Pettifer RF (1984) The structure of soda-silica glasses: a MAS NMR study. Journal of Non-Crystalline Solids 68: 399-410.

26. Stebbins JF (1988) Effects of temperature and composition on silicate glass structure and dynamics: Si-29 NMR results. Journal of Non-Crystalline Solids 106: 359-369.

27. Stebbins JF, Oglesby JV, Lee SK (2001) Oxygen sites in silicate glasses: a new view from oxygen-17 NMR. Chemical Geology 174: 63-75.

28. Xue X, Stebbins JF (1993) 23 Na NMR chemical shifts and local Na coordination environments in silicate crystals, melts and glasses. Physics and Chemistry of Minerals 20: 297-307.

29. McBrierty VJ, Douglass DC (1981) Recent advances in the NMR of solid polymers. Journal of Polymer Science: Macromolecular Reviews 16: 295-366.

30. Spiess HW (1985) Deuteron NMR—a new tool for studying chain mobility and orientation in polymers. editor. Characterization of Polymers in the Solid State I: Part A: NMR and Other Spectroscopic Methods Part B: Mechanical Methods. Springer. pp. 23-58.

31. Chiang C-H, Liu N-I, Koenig JL (1982) Magic-angle cross-polarization carbon 13 NMR study of aminosilane coupling agents on silica surfaces. Journal of Colloid and Interface Science 86: 26-34.

32. Mertzel E, Koenig JL (1986) Application of FT-IR and NMR to epoxy resins. editors. Epoxy Resins and Composites II. Springer. pp. 73-112.

33. Agarwal A, Tomozawa M (1997) Correlation of silica glass properties with the infrared spectra. Journal of Non-Crystalline Solids 209: 166-174.

34. Angell CA (2004) Boson peaks and floppy modes: some relations between constraint and excitation phenomenology, and interpretation, of glasses and the glass transition. J Phys: Condens Matter 16(44): S5153-S5164.

35. Domine F, Piriou B (1983) Study of sodium silicate melt and glass by infrared reflectance spectroscopy. Journal of Non-Crystalline Solids 55: 125-130.

36. Guillot B, Guissani Y (1994) Specific features of the IR spectra of silicate glasses. Journal of molecular structure 325: 129-136.

37. Guillot B, Guissani Y (1997) Boson peak and high frequency modes in amorphous silica. Physical review letters 78: 2401-2404.

38. Sanders DM, Person WB, Hench LL (1974) Quantitative analysis of glass structure with the use of infrared reflection spectra. Applied Spectroscopy 28: 247-255.

39. Jialiang Y (1982) IR studies of alkali silicate glasses. Journal of Non-Crystalline Solids 52: 211-215.

40. Zotov N, Ebbsjö I, Timpel D, Keppler H (1997) Specific features of the IR spectra of silicate glasses. Physical review letters 78: 2401-2404.

41. Fox JR, Andersen HC (1984) Molecular dynamics simulations of a supercooled monatomic liquid and glass. The Journal of Physical Chemistry 88: 4019-4027.

42. Soules TF (1990) Computer simulation of glass structures. Journal of Non-Crystalline Solids 123: 48-70.

43. Micoulaut M (2002) Rigidity transitions and constraint counting in amporphous networks: Beyond the mean-field approach. Europhysics Letters 58(6): 830-836.

44. Trachenko K, Dove MT, Brazhkin V, Phillips JC (2003) Rigidity and logarithmic relaxation in network glasses. J Phys: Condens Matter 15: 1743-1748.

45. Micoulaut M, Phillips J (2003) Rings and rigidity transitions in network glasses. Phys Rev B 67(10):

46. Lee BM, Baik HK, Seong BS, Munetoh S, Motooka T (2006) Generation of glass SiO2 structures by various cooling rates: A molecular-dynamics study. Computational Materials Science 37: 203-208.

47. Micoulaut M, Phillips JC (2007) Onset of rigidity in glasses: From random to self-organized networks. Journal of Non-Crystalline Solids 353(18-21): 1732-1740.

48. Bauchy M, Micoulaut M (2011) Atomic scale foundation of temperature-dependent bonding constraints in network glasses and liquids. Journal of Non-Crystalline Solids 357(14): 2530-2537.

49. Pasquarello A, Hybertsen MS, Car R (1998) Interface structure between silicon and its oxide by first-principles molecular dynamics. Nature 396: 58-60.

50. Donadio D, Bernasconi M, Tassone F (2004) Photoelasticity of sodium silicate glass from first principles. Phys Rev B 70:

51. Tossell JA, Lazzeretti P (1987) Ab initio calculations of oxygen nuclear quadrupole coupling constants and oxygen and silicon NMR shielding constants in molecules containing Si瑕 O bonds. Chemical physics 112: 205-212.

52. Xue X, Kanzaki M (2000) An ab initio calculation of< sup> 17 O and< sup> 29 Si NMR parameters for SiO< sub> 2 polymorphs. Solid state nuclear magnetic resonance 16: 245-259.

53. Ispas S, Benoit M, Jund P, Jullien R (2001) Structural and electronic properties of the sodium tetrasilicate glass Na2Si4O9 from classical and ab initio molecular dynamics simulations. Phys Rev B 64:

54. Charpentier T, Ispas S, Profeta M, Mauri F, Pickard CJ (2004) First-Principles Calculation of O, Si, and Na NMR Spectra of Sodium Silicate Crystals and Glasses. J Phys Chem B 108: 4147-4161.

55. Angell CA (1995) Formation of glasses from liquids and biopolymers. Science 267: 1924-1935.

56. Thorpe MF (1983) Continuous deformations in random networks. J Non-crystalline Solids 57: 355-370.

57. Thorpe MF (1985) Rigidity percolation in glassy structures. J Non-crystalline Solids 76: 109-116.

58. Thorpe MF, Jacobs DJ, Chubynsky NV, Rader AJ (1999) Generic Rigidity of Network Glasses. In: Duxbury TA, editor. Rigidity Theory and Application. Kluwer Academic. Plenum Publishers. pp. 239-277.

59. Avramov I, Keding R, Russel C (2000) Crystallization kinetics and rigidity percolation in glass-forming melts. J Non-crystalline Solids 272: 147-153.

60. Huang L, Kieffer J (2006) Anomalous thermomechanical properties and laser-induced densification of vitreous silica. Applied Physics Letters 89: 141915.

61. Huang L, Kieffer J (2004) Amorphous-amorphous transitions in silica glass. I. Reversible transitions and thermomechanical anomalies. Physical Review B 69: 224203.

62. Kerner R, Phillips JC (2001) Quantitative principles of silicate glass chemistry. Solid State Communication 117: 47-51.

63. Micoulaut M, Malki M, Simon P, Canizares A (2005) On the rigid to floppy transitions in calcium silicate glasses from Raman scattering and cluster constraint analysis. Philosophical Magazine 85(28): 3357-3378.

64. Wyart M, Liang H, Kabla A, Mahadevan L (2008) Elasticity of Floppy and Stiff Random Networks. Phys Rev Lett 101(21):

65. Allwardt JR, Stebbins JF (2004) Ca-Mg and K-Mg mixing around non-bridging O atoms in silicate glasses: An investigation using 17O MAS and 3QMAS NMR. American Mineralogist 89: 777.

66. Balasubramanian S, Rao KJ (1995) A molecular dynamics study of the mixed alkali effect in silicate glasses. Journal of Non-Crystalline Solids 181: 157-174.

67. Cormier L, Neuville DR (2004) Ca and Na environments in Na2O-CaO-Al2O3-SiO2 glasses: influence of cation mixing and cation-network interactions. Chemical geology 213: 103-113.

68. Greaves GN (1998) Structural studies of the mixed alkali effect in disilicate glasses. Solid State Ionics 105: 243-248.

69. Karlsson C, Zanghellini E, Swenson J, Roling B, Bowron DT et al. (2005) Structure of mixed alkali/alkaline-earth silicate glasses from neutron diffraction and vibrational spectroscopy. Physical Review B 72: 064206.

70. Lee SK, Stebbins JF (2003) Nature of Cation Mixing and Ordering in Na-Ca Silicate Glasses and Melts. J Phys Chem B 107: 3141-3148.

71. Dusek K, Prins W (1969) Structure and Elasticity of Non-Crystalline Polymer Networks. editors. Advances in Polymer Science, Volume 6. pp. 1-102.

72. Stauffer D, Conigllio A, Adam M (1982) Gelation and Critical Phenomena. In: Dusek K, editor. Advances in Polymer Science 44. pp. 103-158.

73. Rohr DF, Klein MT (1990) Modeling Diffusion and Reaction in Cross-Linking Epoxy-Amine Cure Kinetics: A Dynamic Percolation Approach. Ind Eng Chm Res 29: 1210-1218.

74. Doi M (1995) Introduction to Polymer Physics. Oxford: Claredon Press.

75. Flory PJ (1979) Molecular theory of rubber elasticity. Polymer 20: 1317-1320.

76. Freed KF, Pesci AI (1989) Computation of the Cross-Link Dependence of the Effective Flory Interaction Parameter Chi for Polymer Networks. Macromolecules 22: 4048-4050.

77. Rodriguez F, Cohen C, Ober C, Archer LA (2003) Principles of Polymer Systems. Taylor & Francis.

78. Ahmad Z, Stepto RFT (1980) Approximate theories of gelation. Colloid & Polymer Sci 258: 663-674.

79. Rolfes H, Stepto RFT (1993) A development of Ahmad-Stepto gelation theory. Makromol Chem, Macromol Symp 76: 1-12.

80. Dobson GR, Gordon M (1965) Theory of Branching Processes and Statistics of Rubber Elasticity. J Chem Phys 43(2): 705.

81. Dobson GR, Gordon M (1964) Configurational Statistics of Highly Branched Polymer Systems. J Chem Phys 41(8): 2389.

82. Kantor Y, Webman I (1984) Elastic Properties of Random Percolating Systems. Physical Review Letters 52(21): 1891-1894.

83. Boal DH (1993) Rigidity and connectivity percolation in heterogeneous polymer-fluid networks. Phys Rev E 47(6): 4604-4606.

84. Head D, MacKintosh F, Levine A (2003) Nonuniversality of elastic exponents in random bond-bending networks. Phys Rev E 68(2):

85. Sahimi M, Arbabi S (1993) Mechanics of disordered solids. II. Percolation on elastic networks with bond-bending forces. Physical Review B 47(2): 703-712.

86. Wilhelm J, Frey E (2003) Elasticity of Stiff Polymer Networks. Phys Rev Lett 91(10):

87. Wool RP (2005) Rigidity percolation model of polymer fracture. J Polym Sci B Polym Phys 43(2): 168-183.

88. Christensen RM (2005) Mechanics of Composite Materials. Mineola, New York: Dover Publications.

89. Ayatollahi MR, Shadlou S, Shokrieh MM (2010) Multi-scale modeling of nonlinear mechanical behavior of polymer/SWNT nanocomposites: Investigation of interphase. Enabling Science and Nanotechnology (ESciNano), 2010 International Conference on: 1-2.

90. Chaboche JL, Girard R, Schaff A (1997) Numerical analysis of composite systems by using interphase/interface models. Computational Mechanics 20: 3-11.

91. Chang YS, Lesko JJ, Case SW, Dillard DA, Reifsnider KL (1994) The Effect of Fiber-Matrix Interphase Properties on the Quasi-Static Performance of Thermoplastic Composites. Journal of Thermoplastic Composite Materials 7: 311-324.

92. Fisher FT, Brinson LC (2001) Viscoelastic interphases in polymer–matrix composites: theoretical models and finite-element analysis. Composites Science and technology 61: 731-748.

93. Jancar J (2008) Review of the role of the interphase in the control of composite performance on micro- and nano-length scales. J Mater Sci 43: 6747-6757.

94. Kaw AK, Selvarathinam AS, Besterfield GH (1992) Comparison of interphase models for a crack in fiber reinforced composite. Theoretical and Applied Fracture Mechanics 17: 133-147.

95. Kim J-K, Sham M-L, Wu J (2001) Nanoscale characterisation of interphase in silane treated glass fibre composites. Composites Part A: applied science and manufacturing 32: 607-618.

96. Li JY (2000) Thermoelastic behavior of composites with functionally graded interphase: a multi-inclusion model. International journal of solids and structures 37: 5579-5597.

97. Papanicolaou GC, Paipetis SA, Theocaris PS (1978) The concept of boundary interphase in composite mechanics. Colloid and Polymer Science 256: 625-630.

98. Reifsnider K, Stinchcomb W, Dillard D, Swain R, Jayaraman K (1992) Role of Interfaces and Interphases in the Evolution Mechanics of Material Systems.

99. Reifsnider KL (1994) Modelling of the interphase in polymer-matrix composite material systems. Composites 25: 461-469.

100. Subramanian S, Lesko JJ, Reifsnider KL, Stinchcomb WW (1996) Characterization of the Fiber-Matrix Interphase and its Influence on Mechanical Properties of Unidirectional Composites. Journal of Composite Materials 30: 309-332.

101. Wang Q, Chiang F-P (1996) Experimental characterization of interphase mechanical properties of composites. Composites Part B: Engineering 27: 123-128.

102. Yi S, Pollock GD, Ahmad MF, Hilton HH (1995) Effective transverse Young’s modulus of composites with viscoelastic interphase. AIAA journal 33: 1548-1550.

103. Israelachvili JN (2011) Intermolecular and Surface Forces. Elsevier.

104. Galiotis C (1991) Interfacial studies on model composites by laser Raman spectroscopy. Composites science and technology 42: 125-150.

105. Liu Y-C, McCreery RL (1995) Reactions of organic monolayers on carbon surfaces observed with unenhanced Raman spectroscopy. Journal of the American Chemical Society 117: 11254-11259.

106. Moskovits M, DiLella DP, Maynard KJ (1988) Surface Raman spectroscopy of a number of cyclic aromatic molecules adsorbed on silver: selection rules and molecular reorientation. Langmuir 4: 67-76.

107. Moskovits M (2005) Surface-enhanced Raman spectroscopy: a brief retrospective. J Raman Spectrosc 36: 485-496.

108. Rusli R, Eichhorn SJ (2008) Determination of the stiffness of cellulose nanowhiskers and the fiber-matrix interface in a nanocomposite using Raman spectroscopy. Appl Phys Lett 93: 033111.

109. Lee B, Park I, Yoon J, Park S, Kim J et al. (2005) Structural Analysis of Block Copolymer Thin Films with Grazing Incidence Small-Angle X-ray Scattering. Macromolecules 38: 4311-4323.

110. Metzger TH, Kegel I, Paniago R, Lorke A, Peisl J et al. (1998) Shape, size, strain and correlations in quantum dot systems studied by grazing incidence X-ray scattering methods. Thin Solid Films 336: 1-8.

111. Zhang J, Posselt D, Smilgies DM, Perlich J, Kyriakos K et al. (2014) Lamellar Diblock Copolymer Thin Films during Solvent Vapor Annealing Studied by GISAXS: Different Behavior of Parallel and Perpendicular Lamellae. Macromolecules 47: 5711-5718.

112. Atanasoska L, Anderson SG, Meyer III HM, Lin Z, Weaver JH (1987) Aluminum/polyimide interface formation: An x-ray photoelectron spectroscopy study of selective chemical bonding. Journal of Vacuum Science & Technology A 5: 3325-3333.

113. Burkstrand JM (1981) Metal-polymer interfaces: Adhesion and x-ray photoemission studies. Journal of Applied Physics 52: 4795-4800.

114. Gerenser LJ (1988) An x-ray photoemission spectroscopy study of chemical interactions at silver/plasma modified polyethylene interfaces: Correlations with adhesion. Journal of Vacuum Science & Technology A 6: 2897-2903.

115. Grunthaner FJ, Grunthaner PJ, Vasquez RP, Lewis BF, Maserjian J et al. (1979) High-Resolution X-Ray Photoelectron Spectroscopy as a Probe of Local Atomic Structure: Application to Amorphous Si O 2 and the Si-Si O 2 Interface. Physical Review Letters 43: 1683.

116. Pan DH, Prest Jr WM (1985) Surfaces of polymer blends: X-ray photoelectron spectroscopy studies of polystyrene/poly (vinyl methyl ether) blends. Journal of applied physics 58: 2861-2870.

117. Sherwood PMA (1990) Auger and X-ray photoelectron spectroscopy. Chichester, England.

118. Thomas HR, O'Malley JJ (1979) Surface studies on multicomponent polymer systems by X-ray photoelectron spectroscopy. Polystyrene/poly (ethylene oxide) diblock copolymers. Macromolecules 12: 323-329.

119. Fischer H (2002) Thermal Probe Surface Treatment of a Bulk Polymer: Does a Surface Layer with a Lower Glass Transition Than the Bulk Exist? Macromolecules 35: 3592-3595.

120. Fragiadakis D, Pissis P, Bokobza L (2005) Glass transition and molecular dynamics in poly (dimethylsiloxane)/silica nanocomposites. Polymer 46: 6001-6008.

121. Kim JH, Jang J, Zin W-C (2000) Estimation of the Thickness Dependence of the Glass Transition Temperature in Various Thin Polymer Films. Langmuir 16: 4064-4067.

122. Kim JH, Jang J, Zin W-C (2001) Thickness Dependence of the Glass Transition Temperature in Thin Polymer Films. Langmuir 17: 2703-2710.

123. Onard S, Martin I, Chailan J-F, Crespy A, Carriere P (2011) Nanostructuration in Thin Epoxy–Amine Films Inducing Controlled Specific Phase Etherification: Effect on the Glass Transition Temperatures. Macromolecules 44: 3485-3493.

124. Sun Y, Zhang Z, Moon K-S, Wong CP (2004) Glass transition and relaxation behavior of epoxy nanocomposites. J Polym Sci B Polym Phys 42: 3849-3858.

125. Tress M, Erber M, Mapesa EU, Huth H, Müller J et al. (2010) Glassy Dynamics and Glass Transition in Nanometric Thin Layers of Polystyrene. Macromolecules 43: 9937-9944.

126. Yang Z, Clough A, Lam C-H, Tsui OKC (2011) Glass Transition Dynamics and Surface Mobility of Entangled Polystyrene Films at Equilibrium. Macromolecules 44: 8294-8300.

127. Bareman JP, Cardini G, Klein ML (1988) Characterization of structural and dynamical behavior in monolayers of long-chain molecules using molecular-dynamics calculations. Physical review letters 60: 2152-2155.

128. Carpenter IL, Hehre WJ (1990) A molecular dynamics study of the hexane/water interface. Journal of Physical Chemistry 94: 531-536.

129. van Buuren AR, Marrink SJ, Berendsen HJC (1993) A molecular dynamics study of the decane/water interface. The Journal of Physical Chemistry 97: 9206-9212.

130. Raut JS, Sholl DS, Fichthorn KA (1997) Molecular-dyanmics simulation of structures and dynamics of n-butane adlayers on Pt(111). Surface Science 389: 88-102.

131. Yasuoka K, Gao GT, Zeng XC (2000) Molecular dynamics simulation of supersaturated vapor nucleation in slit pore.

132. Harmandaris VA, Daoulas KC, Mavrantzas VG (2005) Molecular dynamics simulation of a polymer melt/solid interface: Local dynamics and chain mobility in a thin film of polyethylene melt adsorbed on graphite. Macromolecules 38: 5796-5809.

133. Ghorai PK, Glotzer SC (2007) Molecular Dynamics Simulation Study of Self-Assembled Monolayers of Alkanethiol Surfactants on Spherical Gold Nanoparticles. Journal of Physical Chemistry C 111: 15857.

134. Smit B (1988) Molecular-dynamics simulations of amphiphilic molecules at a liquid-liquid interface. Physical Review A 37: 3431-3433.

135. Sok RM, Berendsen HJC, van Gunsteren WF (1992) Molecular dynamics simulation of the transport of small molecules across a polymer membrane. Journal of Chemical Physics 95: 4699.

136. Teppen BJ, Yu CH, Miller DM, Schäfer L (1998) Molecular dynamics simulations of sorption of organic compounds at the clay mineral/aqueous solution interface. Journal of Computational Chemistry 19: 144-153.

137. Bizzarri AR, Cannistraro S (2002) Molecular Dynamics of Water at the Protein– Solvent Interface. J Phys Chem B 106: 6617-6633.

138. Priezjev NV, Darhuber AA, Troian SM (2005) Slip behavior in liquid films on surfaces of patterned wettability: Comparison between continuum and molecular dynamics simulations. Physical Review E 71: 41608.

139. Olgun U, Kalyon DM (2005) Use of molecular dynamics to investigate polymer melt-metal wall interactions. Polymer 46: 9423-9433.

140. Song M, Chen L (2006) Molecular Dynamics Simulation of the Fracture in Polymer-Exfoliated Layered Silicate Nanocomposites. Macromolecular Theory and Simulations 15: 238-245.

141. Lamas EJ, Balbuena PB (2006) Molecular dynamics studies of a model polymer-catalyst-carbon interface. Electrochimica Acta 51: 5904-5911.

142. Giro R, Caldas MJ (2007) Calcium deposition on poly (para-phenylene vinylene): Molecular dynamics simulations. Physical Review B 76: 161303.

143. Hu M, Shenogin S, Keblinski P (2007) Molecular dynamics simulation of interfacial thermal conductance between silicon and amorphous polyethylene. Applied Physics Letters 91: 241910.

144. Giro R (2008) Atomistic molecular dynamics study of interface formation: Al on poly (p-phenylene vinylene).

145. Niavarani A, Priezjev NV (2008) Rheological study of polymer flow past rough surfaces with slip boundary conditions. J Chem Phys 129: 144902.

146. Heinz H, Farmer BL, Pandey RB, Slocik JM, Patnaik SS et al. (2009) Nature of molecular interactions of peptides with gold, palladium, and Pd-Au bimetal surfaces in aqueous solution. J Am Chem Soc 131: 9704-9714.

147. Smith GD, Bedrov D, Li L, Byutner O (2002) A molecular dynamics simulation study of the viscoelastic properties of polymer nanocomposites. The Journal of Chemical Physics 117: 9478.

148. Smith JS, Bedrov D, Smith GD (2003) A molecular dynamics simulation study of nanoparticle interactions in a model polymer-nanoparticle composite. Composites Science and Technology 63: 1599-1605.

149. Brown D, Mele P, Marceau S, Alberola ND (2003) A molecular dynamics study of a model nanoparticle embedded in a polymer matrix. Macromolecules 36: 1395-1406.

150. Gee RH, Maxwell RS, Balazs B (2004) Molecular dynamics studies on the effects of water speciation on interfacial structure and dynamics in silica-filled PDMS composites. Polymer 45: 3885-3891.

151. Adnan A, Sun CT, Mahfuz H (2007) A molecular dynamics simulation study to investigate the effect of filler size on elastic properties of polymer nanocomposites. Composites Science and Technology 67: 348-356.

152. Leach A (2001) Molecular Modeling: Principles and Applications. Prentice Hall.

153. Lin SS (1990) Oxygen concentration on surfaces of carbon fibers. Journal of Vacuum Science & Technology A: Vacuum, Surfaces, and Films 8: 2412-2416.

154. Tang L-G, Kardos JL (1997) A Review of Methods for Improving the Interfacial Adhesion Between Carbon Fiber and Polymer Matrix. Polymer Composites 18: 100.

155. Mangun CL, Benak KR, Daley MA, Economy J (1999) Oxidation of activated carbon fibers: effect on pore size, surface chemistry, and adsorption properties. Chem Mater 11: 3476-3483.

156. Dilsiz N, Wightman JP (1999) Surface analysis of unsized and sized carbon fibers. Carbon 37: 1105-1114.

157. Oberlin A, Bonnamy S, Lafdi K (1998) Structure and Texture of Carbon Fibers. editors. Carbon Fibers. New York, New York: Marcel Dekker. pp. 85-160.

158. Sherwood PMA (1996) Surface analysis of carbon and carbon fibers for composites. Journal of Electron Spectroscopy and Related Phenomena 81: 319-342.

Chapter 2. Bulk Inorganic Amorphous Networks

2.0. Synopsis

The study of inorganic glasses is key to our understanding of the nature of amorphous solids. The comparatively simple network units of inorganic systems allow us to more readily correlate the structures obtained in simulation with available experimental data. In this section, a series of sodium silicate and soda lime silicate structure have been prepared using molecular dynamics simulations. Overall structural characteristics, mechanical properties, and vibrational spectra have been examined for a series of compositions, exploring the effects of total cation modification and the balance of cation species.

The probability densities of the occurrence of silica structural units and cation clusters were determined as a function of the glass composition. Mean-field rigidity theory was shown to be unable to differentiate between glasses with identical silica content but different cation mixing. Moreover, second shell neighbor behavior was only minimally changed by mixing of the cation species.

The IR spectra have been successfully derived from simulations for several glass compositions. A method for correlating local structures to vibrational modes is used to investigate the nature of the 960 cm^{-1} wavenumber peak in the IR spectra of soda lime silicate glasses, demonstrating an unexpectedly strong contribution from motions of the bridging oxygen along the asymmetric stretching mode.

The bulk and Young's moduli were determined for modified silicate glasses. The minima in bulk modulus with increasing pressure, called the silica anomaly, was eliminated through addition of network modifiers to a degree that depends on the mixing of cation species. While the Young's modulus decrease with increasing silica content, which is in agreement with experiment, whereas mixing cation species has a non-trivial effect on mechanical properties.

2.1. Prior Work in Silicate Glass

Silicate glass is critical to technologies in a vast range of applications, from electronics to construction, to packaging, vehicles, and chemistry labs. However, the amorphous nature of oxide glasses present many challenges for experimental characterization. Simulation is a powerful tool for understanding the nature of structure-property relationships in such glasses.

Vibrational spectroscopy and scattering techniques are the most commonly used experimental tools for probing the fundamental nature of non-crystalline structures. Infrared absorption spectroscopy is based on the ability of the glass to convert the energy of photon into heat by allowing charge dipoles to be excited into resonance at specific frequencies, while in Raman scattering the absorbed energy is reemitted at a different frequency due to changes in the structural moiety's polarizability associated with its deformation (also called vibronic excitation). These resonance and vibronic excitation frequencies are characteristic of the geometry of structural building blocks and their prevailing bond strengths, and the spectral signal can therefore serve to identify these units. Prior studies for amorphous SiO_2 and various silicates have been conducted with both Raman [1,2] and infrared[1,3] spectroscopies, but spectra are sometimes difficult to fully resolve and analyze. Vibrational modes in the higher frequency region are classically associated with localized vibrations of bonds within the SiO_4 tetrahedra. Several similar peak positions are seen in the various silica polymorphs, as well as in other silicate glass systems, but there are clear spectral differences. When compared to crystalline structures, the vibrational spectra of glasses show broad spectral bands, reflecting the lack of structural clarity.

Another common experimental technique is nuclear magnetic resonance (NMR) spectroscopy, used to identify short-range structures in glasses.[4-11] More advanced techniques have been used to study cation distribution and coupling for mixed cation species silicate glasses.[4] X-ray and neutron scattering in amorphous materials is used to examine pair correlations, and was fundamental to the development of initial models of amorphous networks.[12-14] Modern improvements in detectors have allowed some investigation of medium-range characteristics.[15-21] The structure factors derived from these scattering techniques are also a metric for validating structures simulated by atomistic methods.

Several classical molecular dynamics simulation studies of the vibrational modes of a-SiO_2 have been previously reported.[22-27] We have devised a technique for furthering vibrational analysis of atomic trajectories obtained from simulations of silica and sodium silicate glasses.[28] Unlike for ordered crystalline systems, it is not feasible to calculate all vibrational modes by diagonalizing the dynamical matrix corresponding to an amorphous structure, for one because of the required system size, and two because of inevitable displacements from the ground state configuration, giving rise to imaginary frequencies. For comparison, harmonic approximation assignments can be made for isolated structures, such as planar rings.[29] However, these isolated structures do not account for the constraints on their vibrational motion due to being connected to a larger network. Few molecular dynamics models have been able to accurately reproduce spectra beyond a narrow range, though more success has been seen in replication of Raman spectra than infrared spectra.[23,26,27] The potential model originally developed by Huang and Kieffer accounts for a wide range of possible vibrational behaviors, as will be further discussed in the section on computational procedures [30].

Soda lime silicate glasses constitute the basis for the most commonly used oxide glasses in industrial applications. Control over the mixing of the cation species allows engineers to control processing conditions and final properties. However, the role of modifiers in the behavior of the network remains poorly understood, despite a wide variety of methods and studies.[4,21,31-35] It is clear that the mixing of network-modifier cations alters the environment of the non-bridging oxygen. For some properties, such as ion conductance, a non-monotonic trend is observed upon gradual cation type substitution, with a mixture of species being more advantageous than single modifier cation type compositions, while for properties like modulus, the behavior is fairly linear.[36]

This work seeks to examine the effect of network modification in silicate glasses, as well at the effect that mixing the modifier type, i.e., monovalent vs. divalent, has on glass structure and properties. To this end, a series of silicate, sodium silicate, and soda lime silicate glass structures have been prepared by molecular dynamics simulation. The force fields used for the simulations are validated by replicating the relevant crystal structures and IR spectra, when available. Local network structures and cation clustering will be examined and discussed in terms of rigidity theory. Mechanical properties are also scrutinized, with the Young's modulus determined for most compositions, and the bulk modulus determined only for sodium silicate and a constant calcium:sodium ratio series of soda lime silicates.

2.2. Computational Methods

Models to simulate the structure and properties of silica and various silicates have evolved from using nominal valence ionic charges to adjustable fractional charges, which more effectively account for the partial covalent nature of the Si-O bonds. Central force potentials have been long since shown to effectively reproduce equilibrium structures and structural instabilities.[37,38] However, accurate representation of dynamical properties such as phonon dispersion and IR spectra require the implementation of three-body interactions to account for the directional character of covalent bonds.[30]

Furthermore, multicomponent silicate glasses containing network modifiers can posses up to three species of oxygen: bridging O^0, non-bridging O^-, and free oxygen, O^{2-}. These species are characterized by the number of bonds, and accordingly, have different charges. In the simulations presented here, it is not *a priori* known what the final coordination state of a particular oxygen atom will be, and it may change over the course of the simulation. By allowing this factor to evolve according to the physics of the simulation, spatial fluctuations of chemical composition are possible, and the structure is not pre-determined by the assignment of oxygen speciation.

The potential developed by Haung and Kieffer was specifically developed to replicate the dynamical properties as well as the equilibrium structures.[30] The potential includes a standard Coulomb term, a Born-Huggins-Mayer repulsive term and a directional covalent term capable of accommodating multiple coordination states dynamically.[39,40] A charge transfer term controls the balance between the ionic and covalent character of atomic interactions. The magnitude of charge transfer between atoms upon rupture or formation of bonds is dependent on the electronegativity difference between species and the ionization potential. A continuously differentiable charge transfer term is used. The potential energy for a given particle is defined as:

$$\Phi_i = q_i \sum_{j=1}^{N} \frac{q_j}{4\pi\varepsilon_0 r_{ij}} + \sum_{i=1}^{NC} C_{ij} e^{(\sigma_i + \sigma_j - r_{ij}) \cdot \rho_{ij}} + \sum_{j=1}^{NC-1} \sum_{k=j+1}^{NC} (\varphi_{ij} + \varphi_{ik}) e^{-\gamma_{ijk}(\bar{\theta} - \theta_{ijk})^2}$$

Eq. 2.1. Potential energy per particle in the FLX potential

where ε_0 is the dielectric constant of vacuum, r_{ij} is the interatomic distance, and q_i is the charge. The charge of an atom is evaluated according to $q_i = q_i^{\varnothing} - \sum_{j=1}^{NC} (\delta_{ij} \zeta_{ij})$, where q_i^{ϕ} is the charge of the isolated atom and $\zeta_{ij} = \left(1 + e^{b(r_{ij} - a)}\right)^{-1}$ is the previously mentioned charge transfer function, *a* and *b* are empirical parameters.

Electroneutrality is assured by requiring that the fractional charge transferred between bonding partners $\delta_{ij} = -\delta_j$. The term $\left(\varphi_{ij} + \varphi_{ik}\right) e^{-\gamma_{ijk}\left(\bar{\theta} - \theta_{ijk}\right)^2}$, where $\varphi_{ij} = -C_{ij}\left(\kappa_{ij}/\eta_{ij}\right)\zeta_{ij} e^{\left(\lambda_{ij} - r_{ij}\right)\eta_{ij}}$, $C_{ij} = A_{ij}\left[1 + (z_i/n_i) + (z_j + n_j)\right)^{-}$-, and z_i is the valence, and n_i is the number of electrons in the outer shell of atom i, models covalent bonding by acting in the radial and angular direction, as defined by triplets of particles.

The long-range Coulomb interactions are evaluated using the Ewald summation method. The magnitude of the attractive covalent terms is modulated by the angular term, $e^{-\gamma_{ijk}(\overline{\theta}-\theta_{ijk})^2}$, which is symmetric with respect to an equilibrium bond angle $\overline{\theta}$ between the bond vectors r_{ij} and r_{ik}. In this potential model, both Columbic and three-body terms are complementary, as controlled by the charge transfer function.

The potential parameters for binary silicates were first optimized to reproduce the experimentally observed structure and IR spectra of α-cristobalite. These potential parameters were then adopted for interactions involving silicon and oxygen to simulate crystalline sodium disilicate. The optimization of the three additional pair interactions, Na-Na, Na-Si and Na-O, was based on reproducing the structure and density of known crystalline structures. A comparison between β-$Na_2O{\cdot}2SiO_2$ structures determined by x-ray diffraction.[41] measurements and obtained from simulation using optimized parameters is shown in Figure 2.1. The α and γ angles, as well as the a and b lattice vector lengths in the relaxed structure from simulations coincide with the experimentally measured ones, while the magnitudes for β and c differ by 4.8% and 3.1%, respectively. The addition of calcium for soda lime silicates was validated by fitting to known IR spectra for float glass compositions. All potential parameters for FLX are presented in Appendix A Table A-1.

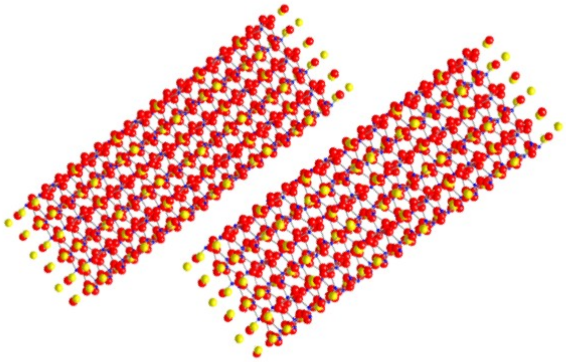

Figure 2.1. Snapshots for $Na_2O.2SiO_2$ (Top) ideal (Bottom) relaxed for 10 ps at 300 K during parameter fitting procedure for crystalline state.

Simulations are performed with fully periodic boundary conditions and approximately 3,000 atoms. Specific numbers of atoms for each composition are presented in Table 2.1. Glasses are randomly initialized at temperatures well in excess of melting, with the specific temperature depending on composition. Structures are then cooled in a stepwise ramp-equilibration procedure, with 100K between steps. The resultant cooling rate is ~10^9 K/ps.

Table 2.1 Number of atoms used in various glass compositions simulated

Label	Si atoms	O atoms	Na atoms	Ca atoms
α-cristobalite	1000	2000	-	-
v-SiO$_2$	1000	2000	-	-
β- sodium disilicate	512	1280	512	-
v-sodium disilicate	1024	2560	1024	-
50-50	500	1500	1000	-
60-40	600	1600	800	-
70-30	700	1700	600	-
80-20	800	1800	400	-
90-10	900	1900	200	-
60-10-30	660	1760	220	330
60-20-20	660	1760	440	220
60-30-10	600	1600	600	100
70-10-20	770	1870	220	220
70-20-10	700	1700	400	100
80-10-10	800	1800	200	100

2.3. Silicates

Structure

In a pure silica glass, each silicon atom is bonded to four oxygen atoms, each of which is bonded to a second silicon atom, forming an infinite random network in accordance with Zachariasen's continuous random network model.[42] However, the introduction of non-networking forming oxides, such as Na_2O and CaO (soda and lime, respectively), disrupts this infinite network, resulting in dangling, or non-bridging oxygen atoms. The disruption of the network is typically quantified in terms of the Q^n number, the number of bridging oxygen atoms bonded to a given silicon atom. This is also measurable by NMR spectroscopy, and hence a good metric for comparison.[4-11,43-45] The distribution of Q^n species for the compositions studied are presented in Figure 2.2.

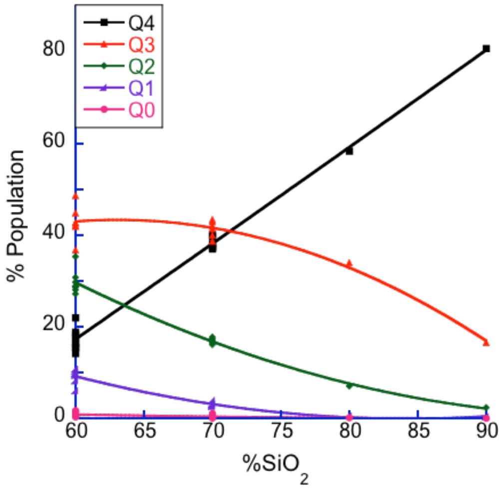

Figure 2.2. Distribution of Qⁿ species for a series of silicate glasses as a function of silica composition.

The amount of Q^4 silicon (black squares) in the network increases almost linearly with the fraction of silica present in the system, with some variation due to cation mixing. The amount of Q^3 silicon (red triangles) is more strongly affected by the balance of network modifiers, as can been seen by the spread in values for 60% silica and 70% silica glasses. Only in the 60%silica case is the Q^2 silicon (green circles) population greater than 20%. While small amounts of Q^1 (purple right triangles) and Q^0 (pink circles) are present in the highly modified glasses; at over 70% silica, these configurations are no longer observed.

In mean-field theory, it is assumed that only covalent bridging links are rigid, and only the first neighbor behavior contributes.[46] Based on the abundances of the Q^n species, it is possible to calculate the concentration of rigid links in the system, which is given by:

$$p = \frac{\langle n \rangle}{\langle v \rangle}$$

Eq. 2.2 Concentration of rigid links in a glass network

where *p* is the concentration of rigid links, *n* is the number of constrained bonds for a given network unit, and *υ n* is the maximum number of constrained bonds for that network unit (4 for silica). The average value of *n* for the system can be calculated by:

$$\langle n \rangle = \sum_{i=0}^{4} \%Q_i * i$$

Eq. 2.3 Average number of constrained bonds in a silicate network

The results for the average concentration of rigid links compared to the ratio of cation species for the glass compositions simulated are presented in Figure 2.3, showing the lack of sensitivity of this value to the mixture of network modifiers.

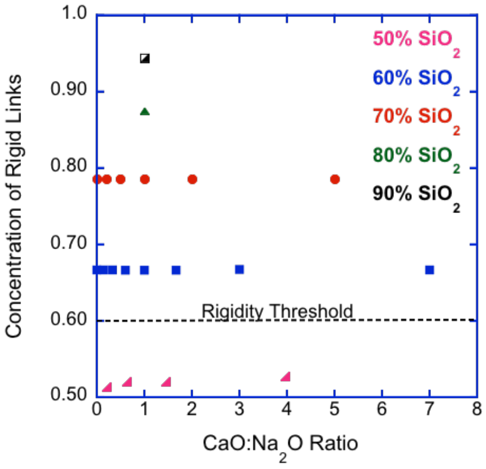

Figure 2.3. The concentration of rigid links is given as a function of cation ratio for glasses with 50% SiO_2 (pink right triangles), 60% SiO_2 (blue squares), 70%SiO_2 (red circles), 80% SiO_2 (green equilateral triangles) and 90% SiO_2 (black half-filled square)

According to rigidity percolation theory, the transition between a "rigid" and "floppy" network occurs at $\langle n \rangle$=2.4, or *p*=0.60. This is shown in Figure 2.3 as a dashed line. This occurs somewhere between 50 %SiO_2 and 60 %SiO_2 in sodium and soda lime silicate glasses according to the Q^n populations. It is important to recall that the rigidity, or elastic, percolation, is not the same as the more classical connectivity percolation. Elastic percolation indicates the onset of non-zero elastic constants and typically requires a significantly higher concentration of bonding in the network.[46] However, it is clear from Figure 2.2 that this simplified model fails to capture the effect of mixed modifier types, which can change the elastic modulus by as much as 30% in a 70.5% SiO_2 glass.[36]

Looking beyond the first neighbor shell, the connectivity of the second neighbor shell was determined by summing the Q^n numbers of the nearest connected silicon neighbors for each silicon atom in the system, not counting the bond to the central silicon. Accordingly, the maximum possible second shell connectivity value of 12 (a Q^4 silicon surrounded by Q^4 silicon atoms). Results for a series of sodium silicate glasses are presented in Figure 2.4(a) and glasses with varying cation ratios in Figure 2.4(b).

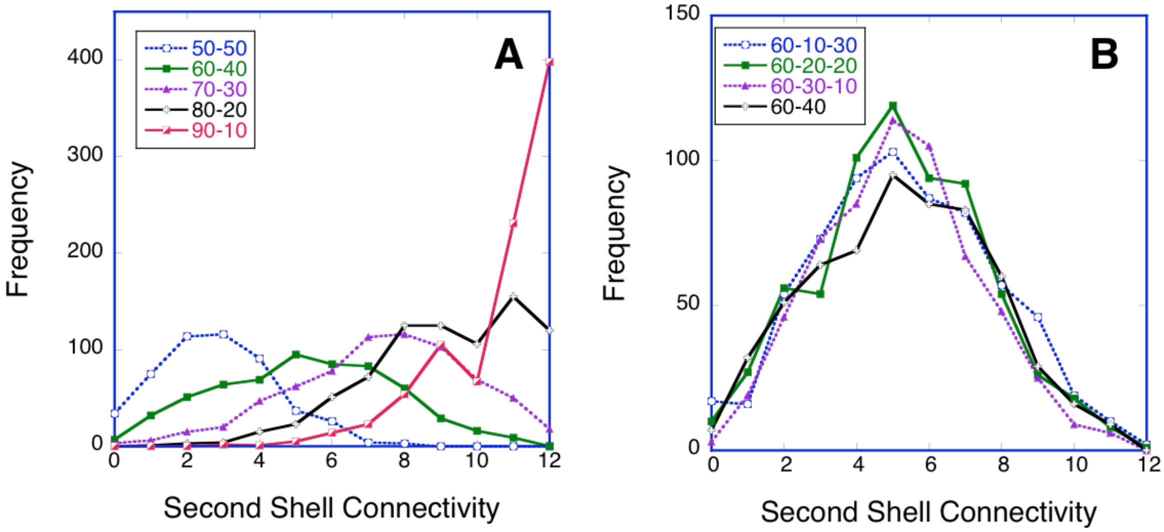

Figure 2.4. Distribution of second shell connectivity for silicon atoms in various glasses, comparing (a) total modification and (b) mixed modifier effects.

Looking at Figure 2.4(a), we see that as the degree of modification is increased, the average second shell connectivity is decreased, as expected. The transition is most dramatic between 80% and 90% silica, with the majority of silicon atoms having a fully connected second shell for 90% silica. The varying cation ratio, shown in Figure 2.4(b), has no obvious systematic effect on the average second shell connectivity, or the distribution of configurations. An average second shell connectivity of ~5 is seen for all compositions, with no silicons having a fully connected second shell. The lack of variation in systems of mixed cation types indicates that even by including second shell behavior, examination of the silica backbone alone is not enough to explain differences in rigidity.

In addition to the structure of the covalent network, the spatial distribution of the cation species affects many properties, including mechanics. We now examine the tendency for cations to form clusters. Cation cluster size was determined by using a cutoff criterion, with the cation-cation coordination to determine the cutoff. Pairs of sodium atoms were given a cutoff of 3.0 Å, while for Na-Ca and Ca-Ca pairs we used a cutoff of 3.5 Å. The size of the largest continuous group of cations (*i.e.,* cluster), normalized by the total number of cations in the system, was determined for each glass composition, presented in Figure 2.5.

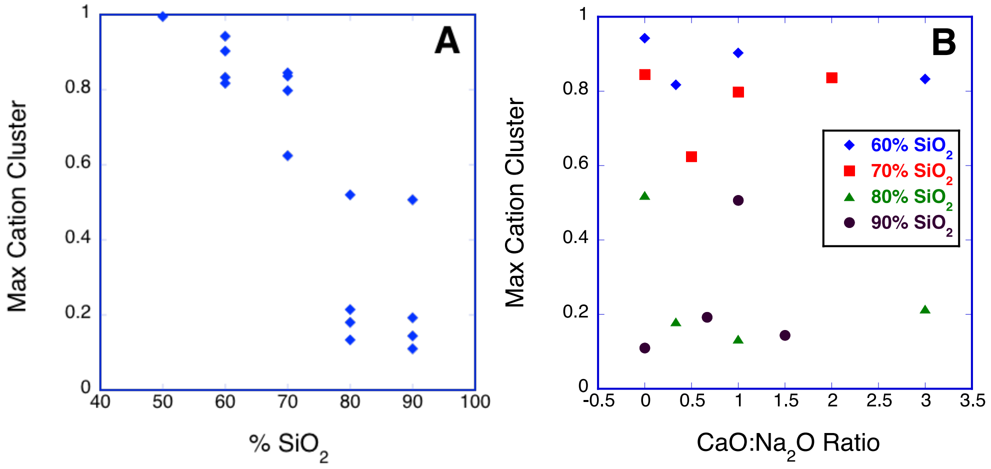

Figure 2.5: The largest continuous group of cations found according to a cutoff criteria of 3.0Å for Na-Na pairs and 3.5Å for Na-Ca and Ca-Ca pairs, normalized by the number of cations present in the glass for (a) percent silica with variable cation types and (b) CaO:Na_2O ratio with variable silica quantities

A higher value for this maximum continuous cluster indicates that the cations are dispersed throughout the system, whereas a lower value indicates the cations are forming more distinct clusters that are isolated from one another. Looking at Figure 2.5(a), there are clearly more discrete clusters in system with fewer cations. However, looking at the same data in terms of the cation ratios, in Figure 2.5(b), there is no obvious correlation between the dispersal of the cations and the balance of sodium and calcium. The propensity to form clusters can also be predicted by the balance of Q^n species, specifically the equilibrium constant of the Q^3 species.[47]

The Q-species balance equation is given by:

$$2Q^n \leftrightarrow Q^{n-1} + Q^{n+1}$$

Eq. 2.4 Q-species balance

with the corresponding equilibrium constant given by:

$$k_n = \frac{\left[Q^{n-1}\right] \cdot \left[Q^{n+1}\right]}{\left[Q^n\right]^2}$$

Eq. 2.5 Q-species equilibrium constant

Given a fixed concentration of silica within the system, this implies that if two silica atoms of $n=3$ were to switch coordination, the resulting product would be one Q^2 and one Q^4 silicon. In order to have regions that are alkali rich or silicate rich, the respective concentrations of Q^2 and Q^4 will be large. However, if the ions are more evenly distributed, there will be a higher equilibrium value of Q^3 silicon in the glass. Therefore, a high value for the k_3 equilibrium constant means that the system is more likely to segregate, with silicate-rich regions containing high concentrations of Q^4 and alkali-rich regions of Q^2, with less Q^3. It is generally observed this constant is higher in simulations than in experiments. The k_3 equilibrium constants for sodium and soda lime silicate glasses are shown in Figure 2.6.

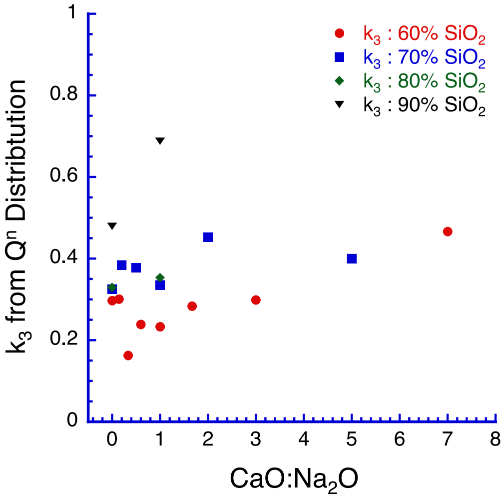

Figure 2.6. Equilibrium constant for Q^3 formation presented as a function of cation ratio for various sodium silicate and soda lime silicate glasses.

In a sodium silicate glass ($CaO:Na_2O=0$), the k_3 constant increases with silica content. For an even modifier ratio ($CaO:Na_2O=1$), the k_3 constant shows the same increasing trend. Looking at glasses of a single silica composition, the k_3 constant shows a compositional minimum with the introduction of calcium, before increasing at high amounts of CaO, indicating that calcium-rich glasses are more likely toform alkali-rich regions. This shift in properties at a particular cation ratio is echoed in other structural measures, such as the radial distribution function.

Additionally, non-random mixing of certain cation combinations, such as sodium and calcium, has been observed by NMR.[4,5,10,33,35] The presence of calcium is known to alter the motion of sodium, and is typically termed the *mixed cation effect*. The coordination environments of cation species in various simulated glasses are presented in Figure 2.7.

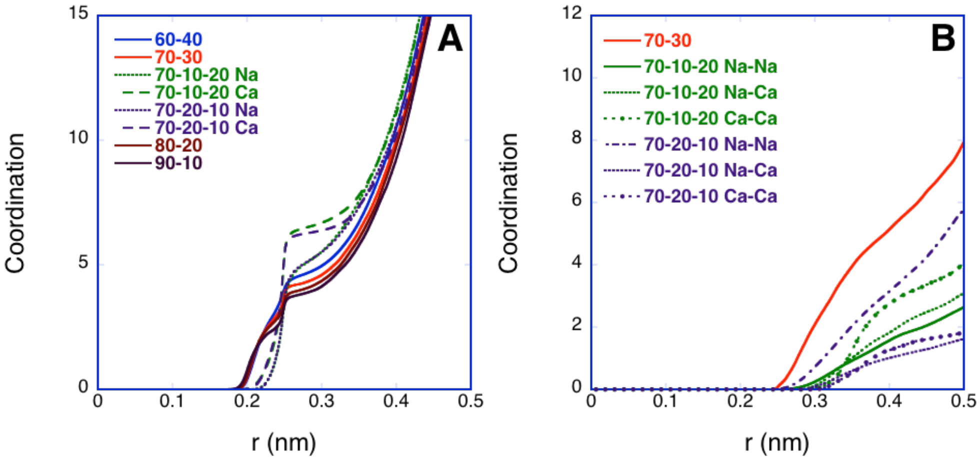

Figure 2.7. Coordination of (a) cations by oxygen for various soda lime silicate and sodium silicate glass compositions (60-40, 70-30, 70-10-20, 70-20-10, 80-20,90-10) and (b) of cation by other cations in three soda lime silicate and sodium silicate glasses (70-10-20, 70-20-10 and 70-30)

Calcium atoms typically have a higher oxygen coordination, as shown in Figure 2.7(a), but not quite double. While there are variations in the total Na-O coordination as a function of the amount of silica, the structure remains fairly uniform. The cation-cation coordinations, in Figure 2.7(b), show an expected increase in Na-Na coordination as overall modification is increased. In both soda lime silicate glasses, the number of like neighbors (Na-Na or Ca-Ca) is higher than would be expected given a random distribution of cations. This is most obvious in the 70 SiO_2-10 Na_2O- 20CaO glass, where the number of cation atoms of each species are equal, but calcium is mostly coordinated with other calcium atoms.

Mechanical Properties

While glass is weak and brittle in tension, under compression it has a substantial strength-to-weight ratio. We are interested in two primary mechanical properties for glasses: the compressive Young's modulus, and the bulk modulus (or its reciprocal, the compressibility). Silicate glasses are known for having anomalous bulk modulus – pressure relationship, wherein increased compression results in increased compressibility below a pressure threshold.[36,39,48] However, modification of the glass composition is known to alter this behavior.

Compressive pressure was gradually applied uniaxially to the prepared glass systems, alternating ramping and equilibration steps, up to a maximum of 2 GPa. The Young's moduli were then determined from the slope in the pressure vs. box dimension data, and the results are plotted in Figure 2.8.

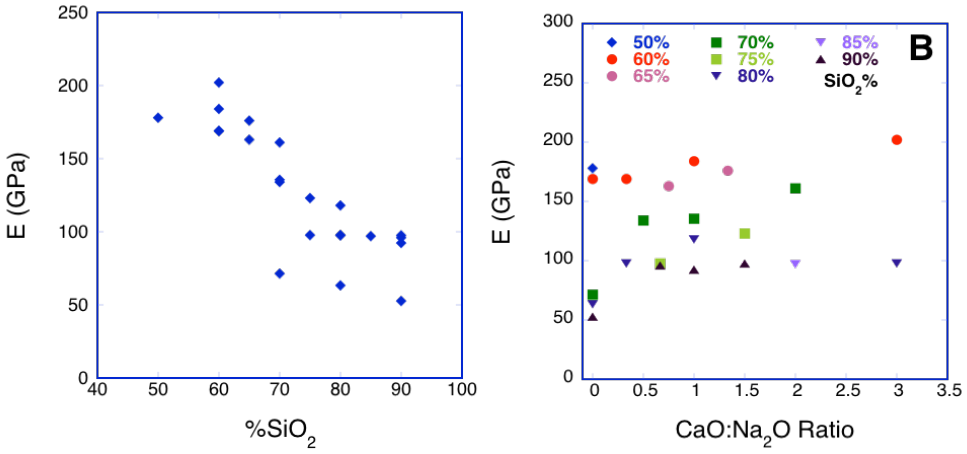

Figure 2.8. Compressive Young's moduli determined from simulation for various glasses as a function of (a) silica content and (b) cation ratio

While the simulated value of the Young's modulus is somewhat high, the general trend of decreasing elasticity with increasing silica content in Figure 2.8(a) is in agreement with experimental data. The experimentally known trend of increasing modulus with increasing CaO:Na$_2$O ratio is also observed in the simulated glass compositions, as shown in Figure 2.8(b). Looking specifically at the 70% silica composition (dark green squares), we see an approximately 50% increase in the Young's modulus between low and high CaO-to-Na$_2$O ratio. Experimentally, an increase of ~30% is seen.[36]

Similar to the aforementioned procedure, to determine the bulk modulus of a series of glass compositions the hydrostatic pressure was gradually increased in the NPT ensemble at a temperature of 300K. Bulk modulus values are then calculated from the slope of the density vs. pressure curves using short line segment fits between multiple points to determine the slope. The original density curves and bulk modulus curves are presented for sodium silicate glasses in Figure 2.9(a) and (b), respectively, and soda lime silicate glass density and bulk modulus are presented in Figure 2.9(c) and (d).

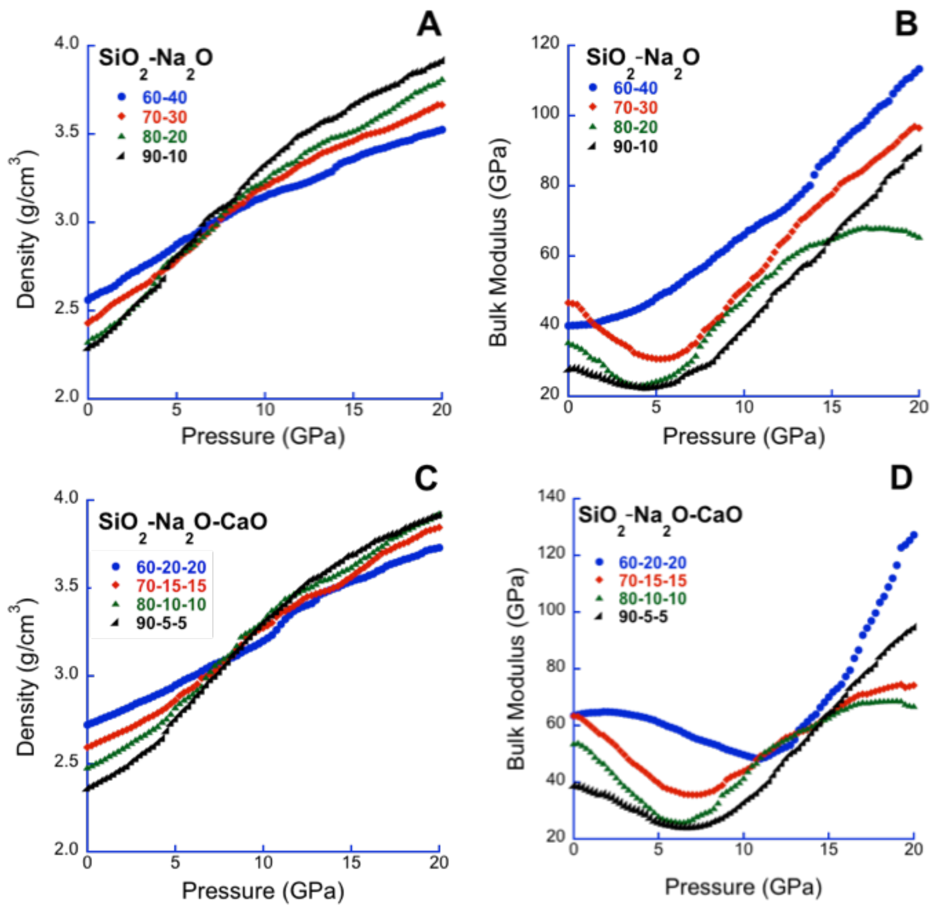

Figure 2.9. (a) Density-pressure curves for binary silicate glasses, (b) bulk modulus as a function of pressure in binary silicate glasses, (c) density-pressure curves for soda lime silicate glasses with even cation mixing and (d) bulk modulus- pressure curves for soda lime silicate glasses with even cation mixing

The behavior of the soda lime silicate glasses is less clear in that the anomalous regime shifts to higher pressures, but it does not disappear. This may be in part due to the role of the divalent cation in the mechanical response of the network. For the same fraction of silicon, substitution with Na_2O results in a higher proportion of cations than substitution with CaO. One of the proposed mechanisms for the suppression of the silica anomaly is the collapse of ring structures.[39,48] The introduction of cation species may inhibit such a deformation. Further analysis of the preferred sites of cations beyond the scope of this document would be required to verify this hypothesis.

Spectral Analysis by Fourier Filtering

For a selection of the above compositions, we have applied a unique method of spectral analysis based on Fourier filtering of atomic trajectories (FFAT) to identify the motion associated with a particular frequency band.[49] The IR absorption spectra can be calculated from the time evolution of the dipole moment, and the correlation function yields the frequency-dependent complex dielectric constant:

$$\varepsilon(\omega) = 1 + 4\pi\chi(\omega) = \int_{\infty}^{-\infty} \langle \dot{\mu}(0) \cdot \mu(t) \rangle e^{i\omega t} \, dt = \varepsilon'(\omega) - i\varepsilon''(\omega)$$

Eq. 2.6 Frequency dependent complex dielectric constant

where ε' is the real and ε'' the imaginary part of the dielectric constant.[50] The angular brackets represent a time average, which is achieved by choosing a large number of instants in the course of a simulation as time origins. This then yields the computed intensity, according to:

$$I(\omega) = \frac{h\varepsilon''}{8\pi^3 \left(1 - e^{-h\omega / 2\pi k_B T}\right)}$$

Eq. 2.7 IR frequency dependent spectral intensity

where ω is angular frequency, the imaginary part of the dielectric constant (ε'')is taken from the frequency-dependent complex dielectric constant above, *h* is Planck's constant and k_B is Boltzmann's constant. The IR spectrum is typically computed over 10,000 time steps under the constant pressure ensemble.

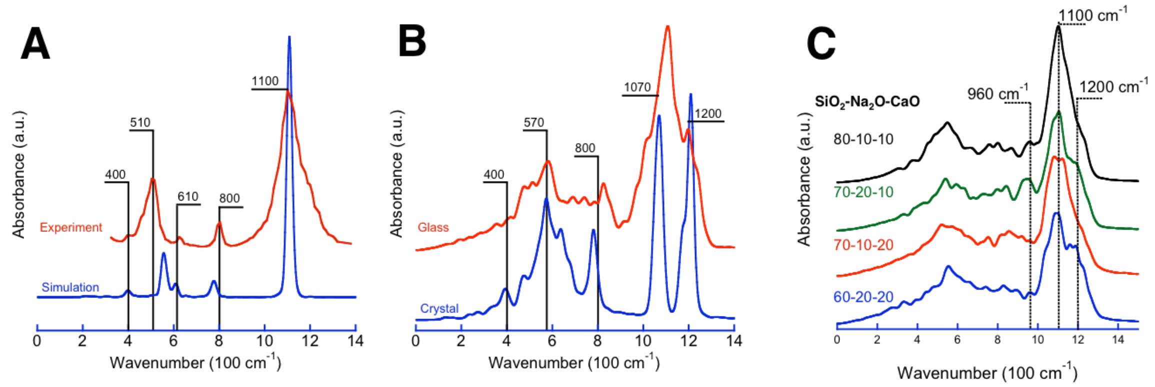

Figure 2.10. Total IR spectra for (a) simulated and experimental cristobalite(b) simulated sodium disilicate crystal and glass and (c) four soda lime silicate compositions. Major peaks are labeled for all spectra.

The computed IR spectra are presented in Figure 2.10. As can be seen in Figure 2.10(a), the computed spectrum (blue) for cristobalite silica has much sharper features than the experimental spectrum (red) for the same polymorph. This is attributed to the lack of a surface or other defect modes that result in peak broadening. It is also similar to the broadening when comparing a crystalline system to a glassy system, as can be seen for sodium disilicate in Figure 2.10(b). The crystalline system, in blue, shows two distinct peaks at 1070 cm^{-1} and 1200 cm^{-1}, whereas the glass shows a broad peak with shoulders. The peak at 1070 cm^{-1} in sodium disilicate and 1100 cm^{-1} in pure silica and most soda lime silicates is assigned to the Si-O-Si stretch mode.[1,3] The 1200 cm^{-1} peak in sodium disilicate and soda lime silicate glass is classically assigned to non-briding oxygen modes.[3,51-54] Figure 2.9(c) shows the simulated IR spectra for a series of soda lime silicate glasses. An additional peak is seen at 960 cm^{-1} as a weak shoulder, which has been assigned as non-bridging oxygen stretching in calcium silicates.[1,55,56] Interestingly, this mode does not correlate well with the quantity of non-bridging oxygen in our system. Additionally, the differences in peak intensity between 70-20-10 and 70-10-20 indicate a difference due to cation mixing, as the two compositions contain identical fractions of non-bridging oxygen. Lower wavenumber peaks are assigned to various modes including ring breathing, but there is typically less consensus on these assignments.

Rather than assigning spectral features via normal mode analysis of a static structure, our method uses a Fourier filtering procedure to isolate the atomic motions responsible for a particular frequency range, including those arising from anharmonic effects. A schematic of the method is presented in Figure 2.11.

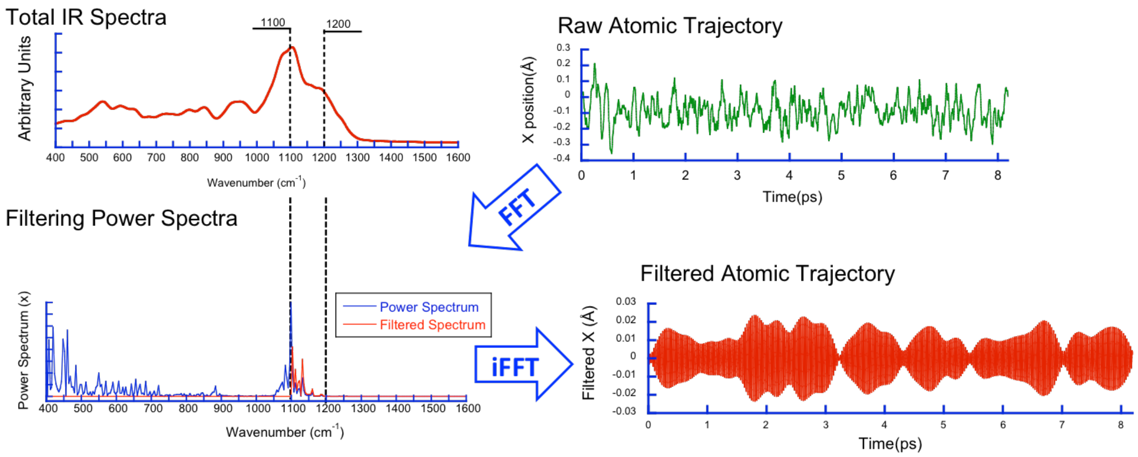

Figure 2.11. Schematic of the procedure used for the Fourier filtering of atomic trajectories

We first identify a band of interest in the IR spectrum, and a subset of atoms that make up an IR active structural unit of interest. This choice is informed by group symmetry, but in principle could be arbitrary. In molecular dynamics, it is straightforward to record the position of each atom as a function of time, making a trajectory that is inherently a composite of all vibrational modes in which a given atom can participate. The trajectory is recorded over several picoseconds to provide adequate statistical sampling.

The x-coordinate of the trajectory of one atom is shown to demonstrate the transformation process. Trajectories are first Fourier transformed to yield their full vibrational spectrum, which typically contains more peaks than the IR spectrum, reflecting the entire motion of this atom, rather than only those motions resulting in fluctuating dipoles. We then filter the spectral region of interest using narrow rectangular windowing functions, zeroing the real and imaginary components of the Fourier spectrum outside of this window. The inverse Fourier transform of the filtered spectrum ultimately yields the atomic trajectories associated with this frequency range, and thus the modes of motion corresponding to the selected spectral band. We can identify the type and symmetry of the mode through transformation or projection of the filtered trajectories onto a coordinate system whose axes mostly coincide with those of the point symmetry group and average positions of the atomic cluster under examination.

For a bridging oxygen site, the anti-symmetric stretch, bend and rock directions become the x, y and z axes for this oxygen, respectively. For the non-bridging case, the modes are defined as a symmetric bond stretching mode, and wagging mode for all other directions. The new axes are created from arbitrary wagging vectors chosen to maintain orthogonality with the Si-O bond vector. These directions are schematically presented in Figure 2.12.

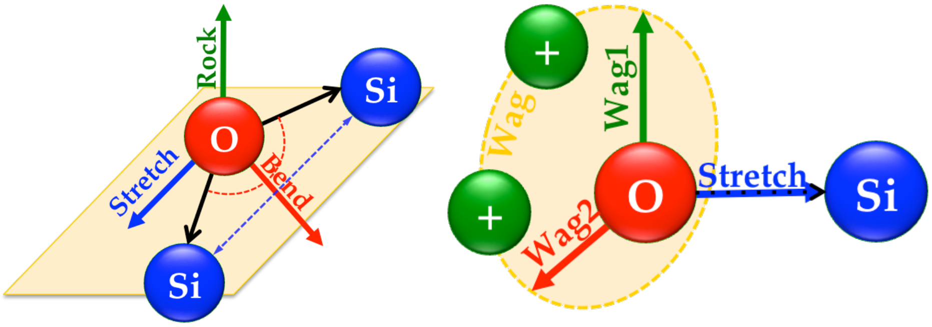

Figure 2.12. Schematic showing the projected coordinate system definitions for a bridging oxygen site (left) and non-bridging oxygen site (right).

The velocity components for each mode are now easily determined and from these we can calculate the thermal energy of each mode of the filtered trajectory. This analysis is carried out and averaged for a statistically representative number of similar structural units. Using this information, we generate a deconstructed spectrum to reveal the modal energy as a function of wavenumber, scaled by the relative population of the BO and NBO species. Given the sample sizes used, the statistical error associated with our analysis is generally less than one percent, and therefore error bars are not explicitly included in the diagrams showing our results.

This analysis was first tested on pure silica and sodium disilicate, in both the crystalline and amorphous form. The amount of energy contributed by each vibrational mode as a function of frequency is presented in Figure 2.13. As can be seen in Figure 2.13 (a) and (b), results for pure silica, in both the crystalline and vitreous forms, agree well with prior experimental assignments of the major peaks.[57,58] Stretching of the bridging oxygen clearly is responsible for the 1100 cm^{-1} spectral band. Figure 2.13 (c) and (d) show the sodium disilicate systems. The FFAT analysis shows that the large peak at ~1100 cm^{-1} corresponds to asymmetric stretching of the bridging oxygen. The higher frequency band at 1200 cm^{-1} is attributed to the non-briding oxygen, with a mix of modes active for the vitreous sodium disilicate, and only the symmetric stretching mode active in the crystal.

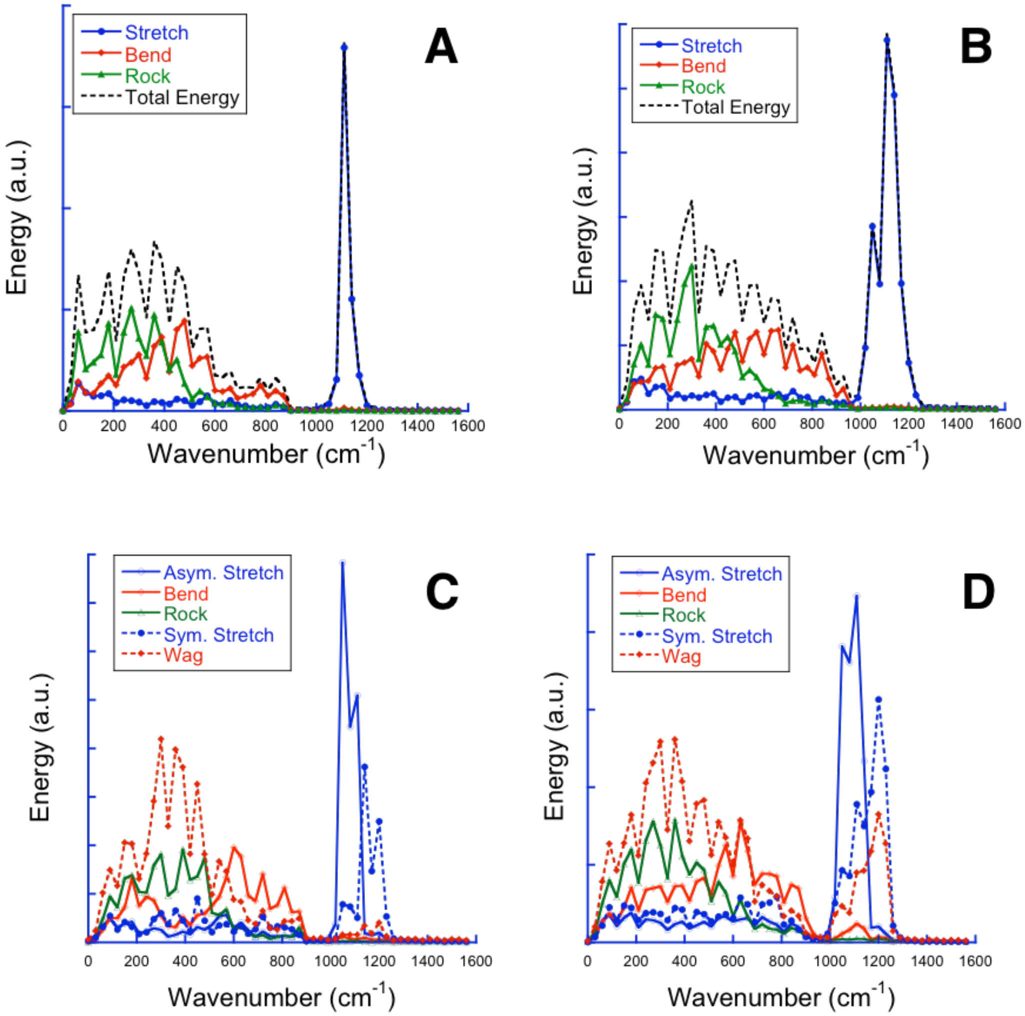

Figure 2.13. Spectral analysis by a Fourier filtered atomic trajectory to identify vibrations contributing to peaks in the (a) silica crystal, (b) silica glass, (c) sodium disilicate crystal and (d) sodium disilicate glass. Bridging oxygen contributions are presented as solid lines, and non-bridging contribution are shown as dashed lines.

By comparison, the vibrational behavior of ternary compositions is more complex. Figure 2.14 shows the FFAT analysis results for four soda lime silicate glasses, including three different amounts of silica, with two cation ratios for the systems containing 70% silica. The 70% silica compositions were chosen to examine the 960 cm^{-1} peak more closely, as there is a significant difference in the sharpness of this peak depending on the calcium-to-sodium oxide ratio.

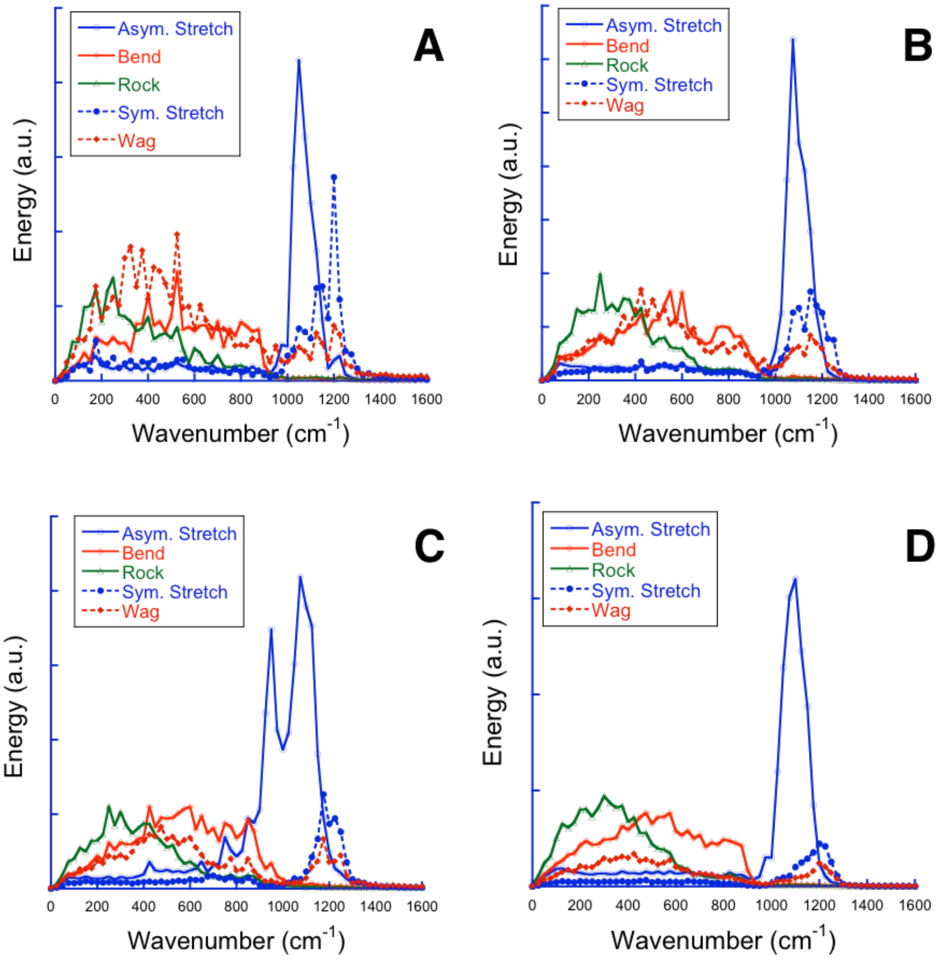

Figure 2.14. Spectral analysis by FFAT to identify vibrational modes in (a) 60% SiO_a-20%Na_2O-20%CaO (b) 70-10-20 (c) 70-20-10 and (d) 80-10-10 glasses. Bridging oxygen contributions are presented as solid lines, and non-bridging contribution are shown as dashed lines.

The assignments for the 1100 cm^{-1} and 1200 cm^{-1} peaks are unchanged from the sodium disilicate results, as expected. Comparing Figure 2.14(a), the 60% silica glass, and Figure 2.13(d), the 80% silica glass, there is an obvious and expected decrease in the contributions of non-bridging modes. Of greater interest is the behavior of the peak at 960 cm^{-1}. which as shown previously in Figure 2.10(c), decreases in intensity both with total degree of modification and increasing the amount of sodium versus calcium, though attributed classically to non-bridging modes. Comparing Figure 2.14(b) and (c), which show a weak 960 cm^{-1} mode and the strongest observed 960 cm^{-1} peak, respectively, there is a clear Si-O-Si asymmetric stretching mode in Figure 2.14(c). This is unexpected, as this mode has been traditionally assigned to non-bridging oxygen.

To further understand this result, we isolate the effect of second shell neighbors on the vibrational modes. Specifically, examining the asymmetric stretching mode, the vibrational energy is further deconvoluted based on the Q^n species between which the oxygen atom in question forms a bridge. Results for the same four soda lime silicate glasses discussed previously are presented in Figure 2.15.

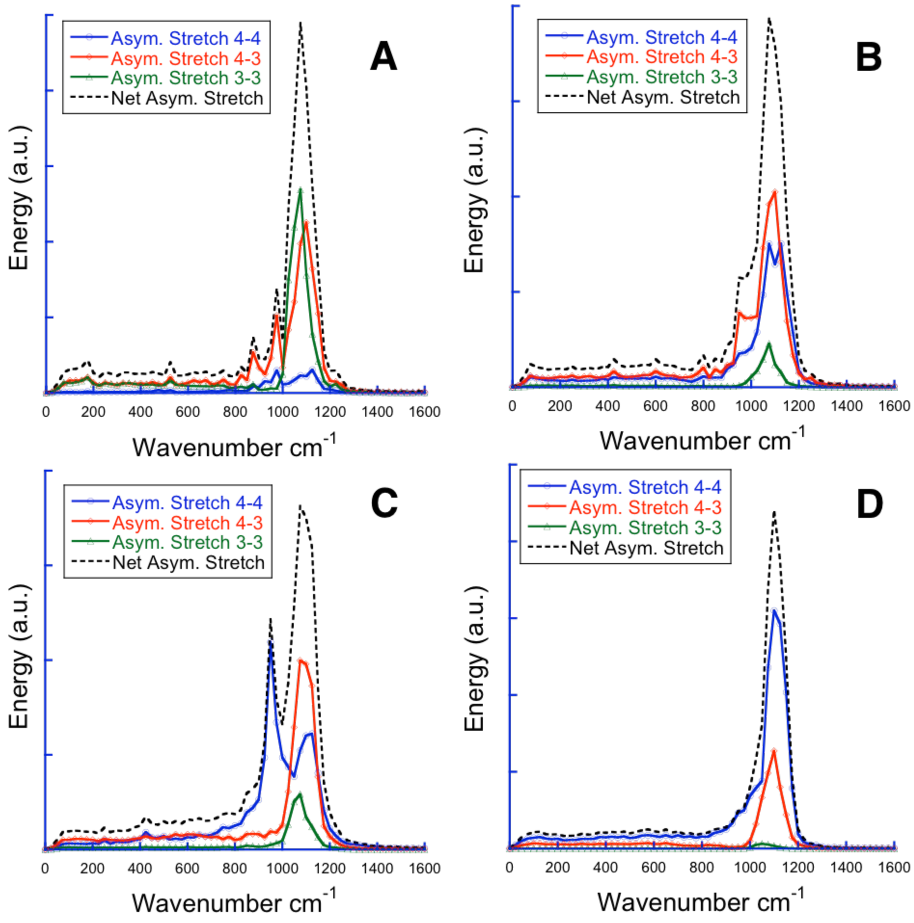

Figure 2.15. Analysis of the asymmetric stretching mode in (a) 60% SiO_a-20%Na_2O-20%CaO (b) 70-10-20 (c) 70-20-10 and (d) 80-10-10, for two Q^4 silicon (blue) a mixed Q^4 and Q^3 silicon (red) and two Q^3 silicon (green) compared to the net energy associated with the asymmetric stretching mode (black, dashed).

For the glass containing 60% silica, shown in Figure 2.15(a), the energy contributions from the different second shell pairings agree well with the relative concentrations of such pairs. In this case, the small shoulder at 960 cm^{-1} seems to come mostly from the asymmetric Q^4-Q^3 pair. This is also seen in the glass with 70% silica, containing less sodium, as shown in Figure 2.15(b). Unexpectedly, the 960 cm^{-1} peak in Figure 2.15(c) is largely attributed to the balanced Q^4-Q^4 pair. This is also seen for the 80% silica glass in Figure 2.14(d). It is possible that this peak is indicative of anharmonic effects in the network, which would explain the lack of a clearly identifiable structural moiety responsible for vibrations in this regime. It is also possible that the cation environment of the oxygen atom has a significant effect, which would require significant further characterization.

2.4. Summary and Conclusions

We have studied a series of silicate glasses in the sodium silicate and soda lime silicate families with a three-body charge transfer potential. Structure, mechanical properties, and vibrational properties are analyzed.

Mean-field rigidity theory is unable to account for mixed modifier effect in soda lime silicate glasses, indicating that short-range ordering of the covalent network is largely unaffected. This is further confirmed by the analysis of the second shell connectivity, which shows only minor variations with changes to the ratio of cation species. The cation clustering behavior was also studied, but no clear trends were identified as a function of cation type mixing ratios. However, some evidence of non-random mixing was observed in soda lime silicates, revealing a tendency to form unlike cation pairs.

The compressive Young's modulus was calculated by applying a constant pressure. Observed trends were generally in agreement with available experimental data. The bulk modulus behavior was also calculated for several sodium silicate and soda lime silicate glasses. As the amount of silica is decreased, the anomalous modulus minimum at elevated pressures vanishes between 70% and 60% silica. The substitution of calcium for sodium was less effective at eliminating the anomalous behavior. Further characterization of the cation sites could shed more light on this behavior.

The IR spectra were computed and analyzed. To further understand the structural moieties responsible for the vibrational behavior, a Fourier Filtered Atomic Trajectory method was applied and presented. Results for peaks in pure silica and sodium disilicate glasses agree well with prior investigations. However, the shoulder observed at 960 cm^{-1}, which is typically attributed to non-bridging oxygen, is shown to be related to an asymmetric stretching of the Si-O-Si unit. Further analysis of the speciation of the silica atoms was not directly conclusive. However, it indicating a possible anharmonic behavior of the network leading to the development of this vibrational mode.

The amorphous state of inorganic matter remains a complex area of study with many open questions. One suggestion for future work is further exploration of the local neighborhood of the cation species, particularly as it relates to their position within rings.

2.5. References

1. Handke M, Mozgawa W (1993) Vibrational spectroscopy of amorphous silicates. Vibrational Spectroscopy 5: 75-84.

2. Zotov N, Ebbsjö I, Timpel D, Keppler H (1997) Specific features of the IR spectra of silicate glasses. Physical review letters 78: 2401-2404.

3. Ferraro JR, Manghnani MH (1972) Infrared absorption spectra of sodium silicate glasses at high pressures. Journal of Applied Physics 43: 4595-4599.

4. Gee B, Eckert H (1996) Cation Distribution in Mixed-Alkali Silicate Glasses. NMR Studies by 23Na-{7Li} and 23Na-{6Li} Spin Echo Double Resonance. The Journal of Physical Chemistry 100: 3705-3712.

5. Maewaka H, Maewaka T, Kawamura K, Yokokawa T (1991) The structural groups of alkali silicate glasses determined from 29Si MAS-NMR. Journal of Non-Crystalline Solids 127: 53-64.

6. Jones AR, Winter R, Greaves GN, Smith IH (2001) MAS NMR study of soda-lime-silicate glasses with variable degree of polymerisation. Journal of non-crystalline solids 293: 87-92.

7. Maekawa H, Yokokawa T (1997) Effects of temperature on silicate melt sructure: A high temperature 29Si NMR study of Na2Si2O5. Geochimica et cosmochimica acta 61: 2569-2575.

8. Dupree R, Holland D, McMillan PW, Pettifer RF (1984) The structure of soda-silica glasses: a MAS NMR study. Journal of Non-Crystalline Solids 68: 399-410.

9. Stebbins JF (1988) Effects of temperature and composition on silicate glass structure and dynamics: Si-29 NMR results. Journal of Non-Crystalline Solids 106: 359-369.

10. Stebbins JF, Oglesby JV, Lee SK (2001) Oxygen sites in silicate glasses: a new view from oxygen-17 NMR. Chemical Geology 174: 63-75.

11. Xue X, Stebbins JF (1993) 23 Na NMR chemical shifts and local Na coordination environments in silicate crystals, melts and glasses. Physics and Chemistry of Minerals 20: 297-307.

12. Mozzi RL, Warren BE (1969) The structure of vitreous silica. J Appl Cryst 2(4): 164-172.

13. Mozzi RL, Warren BE (1970) The structure of vitreous boron oxide. J Appl Cryst 3(4): 251-257.

14. Warren BE, Mozzi RL (1966) Multiple scattering of X-rays by amorphous samples. Acta Cryst 21: 459.

15. Benedetti A, Geotti-Bianchini F, Fagherazzi G, Riello P, Albertini G et al. (1994) SAXS study of the micro-inhomogeneity of industrial soda lime silica glass. Journal of Non-Crystalline Solids 167: 263-271.

16. Greaves GN (1985) EXAFS and the structure of glass. Journal of Non-Crystalline Solids 71: 203-217.

17. Biscoe J (1941) X-ray study of soda-lime-silica glass. Journal of The American Ceramic Society 24: 262-264.

18. Medda MP, Musinu A, Piccaluga G, Pinna G (1993) Na+ coordination in sodium diborate and triborate glasses with x-ray diffration. Journal of Non-Crystalline Solids 162: 128-135.

19. Gaskell PH (2005) Medium-range structure in glasses and low-Q structure in neutron and X-ray scattering data. Journal of Non-Crystalline Solids 351: 1003-1013.

20. Warren BE, Biscoe J (1938) THE STRUCTURE OF SILICA GLASS BY X-RAY DIFFRACTION STUDIES*. Journal of the American Ceramic Society 21: 49-54.

21. Karlsson C, Zanghellini E, Swenson J, Roling B, Bowron DT et al. (2005) Structure of mixed alkali/alkaline-earth silicate glasses from neutron diffraction and vibrational spectroscopy. Physical Review B 72: 064206.

22. Wilson M, Madden PA, Hemmati M, Angell CA (1996) Polarization Effects, Network Dynamics, and the Infrared Spectrum of Amorphous SiO_ {2}. Physical review letters 77: 4023-4026.

23. Guillot B, Guissani Y (1997) A Molecular Dynamics Study of the Vibration Spectra of Silica Polyamorphs. Molecular Simulation 20: 41-61.

24. Guillot B, Guissani Y (1997) Boson peak and high frequency modes in amorphous silica. Physical review letters 78: 2401-2404.

25. Taraskin SN (2007) Infrared absorption in glasses and their crystalline counterparts. Journal of Physics: Condensed Matter 19: 415113.

26. Pasquarello A, Car R (2007) Dynamical Charge Tensors and Infrared Spectrum of Amorphous SiO2. Physical Review Letters 79: 1766-1770.

27. To TT, Bougeard D, Smirnov KS (2008) Molecular dynamics study of the vibrational pattern of ring strucutures in the Raman spectra of vitreous silica. Journal of Raman Spectroscopy 39: 1869-1877.

28. Upadhyay AK, Sebeck K, Kieffer J (2012) Spectral mode assignment for binary silicate glasses using molecular dynamics simulations. Journal of Non-Crystalline Solids 358: 3348-3354.

29. Mihailova B, Zotov N, Marinov M, Nikolov J, Konstantinov L (1994) Vibrational spectra of rings in silicate glass. Journal of Non-Crystalline Solids 168: 265-274.

30. Huang L, Kieffer J (2003) Molecular dynamics study of cristobalite silica using a charge transfer three-body potential: Phase transformation and structural disorder. J Chem Phys 118: 1487.

31. Balasubramanian S, Rao KJ (1995) A molecular dynamics study of the mixed alkali effect in silicate glasses. Journal of Non-Crystalline Solids 181: 157-174.

32. Greaves GN (1998) Structural studies of the mixed alkali effect in disilicate glasses. Solid State Ionics 105: 243-248.

33. Allwardt JR, Stebbins JF (2004) Ca-Mg and K-Mg mixing around non-bridging O atoms in silicate glasses: An investigation using 17O MAS and 3QMAS NMR. American Mineralogist 89: 777.

34. Cormier L, Neuville DR (2004) Ca and Na environments in Na2O-CaO-Al2O3-SiO2 glasses: influence of cation mixing and cation-network interactions. Chemical geology 213: 103-113.

35. Lee SK, Stebbins JF (2003) Nature of Cation Mixing and Ordering in Na-Ca Silicate Glasses and Melts. J Phys Chem B 107: 3141-3148.

36. Narottam B, Doremus RH (1986) Elastic Properties. editors. Handbook of Glass Properties. Elsevier. pp. 306-336.

37. Tse JS, Klug DD (1991) The structure and dynamics of silica polymorphs using a two-body effective potential model. J Chem Phys 95(12): 9176.

38. VAN BEEST BWH, KRAMER GJ, VAN SANTEN RA (1990) FORCE-FIELDS FOR SILICAS AND ALUMINOPHOSPHATES BASED ON ABINITIO CALCULATIONS. Phys Rev Lett 64(16): 1955-1958.

39. Huang L, Kieffer J (2004) Amorphous-amorphous transitions in silica glass. I. Reversible transitions and thermomechanical anomalies. Physical Review B 69: 224203.

40. Huggins ML, Mayer JE (1933) Interatomic distances in crystals of the alkali halides. The Journal of Chemical Physics 1: 643-646.

41. Pant AK (1968) A reconsideration of the crystal structure of-Na2Si2O5. Acta Crystallographica Section B: Structural Crystallography and Crystal Chemistry 24: 1077-1083.

42. Zachariasen WH (1932) The Atomic Arrangement in Glass. J Am Chem Soc 54(10): 3841-3851.

43. Dupree R, Holland D, Williams DS (1986) The structure of binary alkali silicate glasses. Journal of Non-Crystalline Solids 81: 185-200.

44. Schneider J, Mastelaro VR, Zanotto ED, Shakhmatkin BA, Vedishcheva NM et al. (2003) Qn distribution in stoiciometric silicate glasses: thermodynamic calculations and 29Si high resolution NMR measurements. Journal of Non-Crystalline Solids 325: 164-178.

45. Mayerhofer TG, Shen Z, Leonova E, Eden M, Kriltz A et al. (2008) Consolidated silica glass from nanoparticles. Journal of Solid State Chemistry 181: 2442-2447.

46. Thorpe MF (1985) Rigidity percolation in glassy structures. J Non-crystalline Solids 76: 109-116.

47. Machacek J, Gedeon O (2003) Q-species in alkali-disilicate glasses. Ceramics- Silikaty 47: 45-49.

48. Huang L, Kieffer J (2006) Anomalous thermomechanical properties and laser-induced densification of vitreous silica. Applied Physics Letters 89: 141915.

49. Anderson DC, Kieffer J, Klarsfeld S (1993) Molecular dynamic simulations of the infrared dielectric response of silica structures. J Chem Phys 98: 8978.

50. Brawer SA (1984) Theory of relaxation in viscous liquids and glasses. J Chem Phys 81: 954.

51. Abo-Naf SM, El Batal FH, Azooz MA (2003) Characterization of some glasses in the system SiO2, Na2O· RO by infrared spectroscopy. Materials chemistry and physics 77: 846-852.

52. Guillot B, Guissani Y (1994) Specific features of the IR spectra of silicate glasses. Journal of molecular structure 325: 129-136.

53. Khalil EMA, ElBatal FH, Hamdy YM, Zidan HM, Aziz MS et al. (2010) Infrared absorption spectra of transition metals-doped soda lime silica glasses. Physica B: Condensed Matter 405: 1294-1300.

54. Lee YK, Peng YL, Tomozawa M (1997) IR reflection spectroscopy of a soda-lime glass surface during ion-exchange. Journal of non-crystalline solids 222: 125-130.

55. De Sousa Meneses D, Malki M, Echegut P (2006) Optical and structural properties of calcium silicate glasses. Journal of Non-Crystalline Solids 352: 5301-5308.

56. Jialiang Y (1986) Further studies on the IR spectra of silicate glasses. Journal of Non-Crystalline Solids 84: 114-119.

57. HANDKE M (1986) VIBRATIONAL-SPECTRA, FORCE-CONSTANTS, AND SI-O BOND CHARACTER IN CALCIUM SILICATE CRYSTAL-STRUCTURE. Appl Spectrosc 40(6): 871-877.

58. Simon I, McMahon HO (1953) Study of the structure of quartz, cristobalite, and vitreous silica by reflection in infrared. Journal of Chemical Physics 21: 23.

Chapter 3. : Structure and mechanics of highly crosslinked bulk network structures

3.0. Synopsis

A series of bulk epoxy systems using a low-shrinkage aliphatic amine hardener were studied. One epoxy resin, diglycidal ether of bispenol F (DGEBF) and two amine hardeners, diethylentriamine (DETA) and triethyleneteramine (TETA) were selected. The effects of system size, amine functionality, and overall stoichiometry on structure and mechanical properties were explored.

Structures were generated using an iterative reaction-relaxation molecular dynamics approach. Bonds within a given cutoff radius are generated at regular time intervals, with a probability term correcting for the different reactivities of primary and secondary amines. The new topology is the relaxed to eliminate induced stresses using molecular dynamics, and the procedure repeats. This method balances the need for rapid structure generation with the desire to follow a natural progression of the cure and the need to minimize residual stresses.

The density and molecular weight were monitored as a function of degree of cure. The observed shrinkage behavior is in good agreement with experiment, and consistent across most system sizes, functionalities, and stoichiometries. Small systems were shown to have greater sensitivity to the initial configuration of monomers, in terms of density, molecular weight, and dispersity. While amine-rich systems reached higher degrees of conversion of the epoxide resin, network percolation was delayed, with the development of an effectively infinite cluster instead tied to the average number of amine links.

Visualization of the network formation showed that the DGEBF resin monomers tend to cluster together, which may account for the higher proportion of unreacted monomers as cure progresses. Network formation is accompanied by only small changes in the pair correlation functions that can be clearly attributed to the breaking and forming of bonds. Some residual stress development during cure; as a function of cure, a slight net tensile stress arises in the system. However, the development of stresses was still less than expected, as the opening of the oxirane group acts in competition with shrinkage forces.

The elastic modulus and necking behavior were calculated as a function of cure for each epoxy system. While elastic properties were only minimally improved by the addition of network bonds within the range of cure studied, the necking strength improved with greater conversion. Also quantified was void formation, which exhibits a nucleation and growth behavior, with nucleation dominating at low degrees of conversion, and more dramatic growth behavior as the network is formed.

3.1.Introduction to Cross-linked Polymer Systems

Industrial use of polymer matrix composite is increasing to address needs for lightweighting, while maintaining mechanical performance. This is particularly critical where fuel efficiency is a major performance metric, such as automotive, aerospace, and military applications. While there are a variety of classes of composite materials, polymer matrix composites typically have better elasticity and processability than ceramic or metal matrix composites, as well as lower production costs. One of the most common matrix materials in industrial polymer matrix composites is epoxy. Two part epoxy resins come in a variety of chemistries, allowing control over the processing temperature, cure rate, and shrinkage. These polymers also have good toughness, strength, and a relatively resistant to chemical attack.

In applications where tolerances are critical and residual stresses need to be minimized, the volumetric change on cure is a major concern, typically leading to the use of aliphatic amines.[1-4] Most commercial hardeners are a blend of multiple functionalities and chain lengths, but the exact chemistry is typically proprietary. The epoxy resins tend to be less varied, with the diglycidal ethers of bisphenol A and bisphenol F (commercially known as EPON 828 and 862, respectively) as two of the more commonly studied. To this end, we have chosen a room-temperature curing resin-hardener system with one epoxy resin, diglycidal ether of bisphenol F (DGEBF) and two aliphatic amines, diethylenetriamine (DETA) and trietheyleneteteramine (TETA), shown in Figure 3.1.

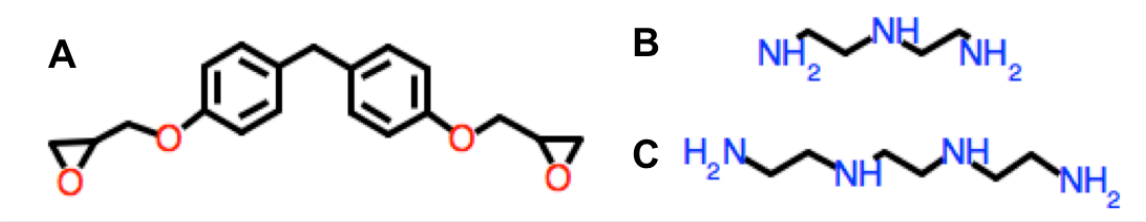

Figure 3.1. (a) diglycidal ether of bisphenol F (b) diethylenetriamine and (c) trietheyleneteteramine

In prior experimental work, the Kieffer group has examined the development of mechanical properties during the curing of highly cross-linked polymer networks.[5-9] Two different polymerization mechanisms were studied: ring-opening metathesis polymerization (ROMP) in dicyclopentadiene (DCPD) and a step-growth polymerization in a two-part epoxy resin. In prior computational work the curing of DCPD has already been explored. One key finding was that replication of the ring-opening mechanism is critical to predicting the development of mechanical properties during cure. It is therefore important that realistic structures be generated first before accurate property predictions can be expected. The epoxy resin system studied by Alrdidge *et. al.* used DGEBF and a proprietary commercial aliphatic amine hardener blend, Epicure 9553.

One common issue with the studies reported in the existing literature is system sizes used were rather small. Many of these studies use fewer than 200 monomers, often employing closed commercial codes that do not provide adequate methods for polymerization.[10-19] Even these small systems are achieved through periodic replication of small units, which are then linked together and result in a falsely ordered structure. A surprising number of authors chose not to report this information at all, at best giving the density and box volume, leaving the calculations as an exercise for the reader. Systems containing fewer than 400 monomers may simply not be sufficient to reflect amorphous network structures.

In our prior experience with inorganic glasses, 1000 network units were typically required to avoid system size effects. Percolation theory also suggests that the critical number of bonds formed for connectivity is incorrectly predicted by small systems.[20,21] However, polymer systems typically have large, more flexible network units. Accordingly, it is possible that these systems may be less sensitive to spatial constraint than oxide glasses or theoretical lattices. To verify sensitivity to spatial constraint, we conduct a study of mechanical properties and network topology as a function of system size.

The nature of highly cross-linked polymer networks may also be affected by the functionality and backbone structure of the monomers chosen. Polymer network theory as pioneered by Flory and Stockmayer has long discussed the critical degree of cure at which gelation occurs as a function of the functionality of the monomers.[22] However, the nature of the backbone is also known to affect the mechanics of the polymer network.[23,24]

The last several years have seen a dramatic increase in the number of studies of epoxy and epoxy composites using molecular dynamics simulations and atomistic modeling.[25-45] Given the engineering importance of these materials, this is hardly a surprising development. Newer simulations have improved in terms of the system sizes, and expand the breadth of epoxy chemistries explored. Properties under conditions such as creep, high strain rate fracture, compressive loading and cyclic loading have been studied. Simulations of adhesion and interfacial properties will be discussed in later chapters. Much prior work in epoxy simulations has been performed with aromatic amines, such as diethyltoluenediamine

(DETDA), with a single type of amine used in the vast majority of simulations. Some simulations of aliphatic amines have been performed, but typically using a closed commercial code, limiting their reproducibility. Table 3.1 shows a summary of many of the epoxide resin and hardener combinations found in literature, indicating the force field used and number of monomers or atoms when possible.

Table 3.1: Summary of epoxy-resin combinations simulated using MD found in the literature

Hardener/ Epoxy Resin		DGEBA	DGEBF	Other
Aliphatic	DDA	PCFF* [46] (U/A)		
	EDA	COMPASS*[12] (150)		COMPASS*, BPA (66) [47]
	DETA	COMPASS* [14] (35) [38] (140), Network MC* [48] (U/A),QM [49] (1), OPLS-UA [44] (672), AMBER [43] (U/A)	AMBER [43] (U/A)	AMBER, TGDDM [43] (U/A)
	TETA	COMPASS[19] (168)	PCFF* [10] (U/A) [39](280), COMPASS* [19] (168),	
	TMAB	Amber [50,51] (308)		
	Jeffamines (APTA)	PCFF [52] (6000 atoms), AMBER [42](1458), [53] (225)	PCFF [52] (6000 atoms), Dreiding [33] (1536)	
Alicyclic	MDA	COMPASS* [11] (32 monomers), "Network" MC* [48] (U/A), COMPASS* [34] (89)		
	AEP	COMPASS* [15] (25)		
	Cymel			PCFF* [18] (100)
Aromatic	DDS	CG Amber [54](324), OPLS-UA [44] (672), CVFF [29,41] (107), AMBER [43] (U/A), [28] (U/A)	Dreiding [55,56] (1536) [33,40] (1536), AMBER [43] (U/A)	TGDDM-Amber [57] (343), [43] (U/A)
	DEDTA		GPUMD LJ [58](2186), COMPASS* [59] (1 monomer), CVFF [60] (384), OPLS-UA [61-	

			65] (648 [61-64]) 21,288 atoms [65] (384 [66])	
	IPD	COMPASS*, Dreiding* [16,17] (36 ,24)		
	MPDA	Network MC* [48] (U/A), AMBER [43] (U/A)	AMBER [43] (U/A)	TGDDM AMBER [43] (U/A)
Other/ Unknown		LJ CG [67,68] [32](4800), *ab*LJ [69], resin only COMPASS* [25]Jeffamine+MCA Amber [26](4080)	REBO [70], Dreiding (APB13, TREN) [33] (1536)	Non-amine OPLSAA [13] (192), Mixed amine COMPASS* [71,72] (56), COMPASS* BPA/Xylox (U/A) [73], COMPASS* BPA/Novolac [74] (756), [45] (180,000 atoms), Vinyl esters COMPASS[75] (89), SU-8 Dreiding/CVFF/PCFF [36] 40), CG LJ BPA/Novalac [35]

**Indicates simulations were conducted with a closed commercial code*

In the present work we will compare epoxies cured using two different aliphatic amines separately and using blends thereof. While the majority of studies mentioned use a single amine, many commercial hardeners like Epicure 9553 are a blend of amines. Furthermore, the effect of stoichiometry will also be investigated. Many industrial applications adjust the blend of resin and hardener to achieve the desired properties and processing times.[76] It is expected that with a system in stoichiometric balance, topological constraints will prevent conversion of the epoxide groups in the system. Results of the cure experiments by the Kieffer group showed that excess hardener beyond the manufacturer epoxide equivalent weight recommendations results in higher overall conversion as measured by the decrease in the fraction of remaining epoxide groups.[8]

Many researchers interested in the mechanical properties of epoxy networks have used various *a priori* or black box methods to create a network structure that is then later analyzed. However, we are interested in the structure and mechanical properties as the network develops, making it necessary to employ an iterative reaction-relaxation algorithm. The efficiency and efficacy of several algorithms was investigated by Knox *et. al.*[52] Four main classes were identified: one-by-one, all-at-once, lattice-based construction and cutoff-controlled. The one-by-one algorithm is notoriously inefficient, but effectively avoids excessive residual stresses. High performance is seen with all-at-once method, while the cutoff-controlled algorithm class provides a good compromise. Lattice-based constructions may not realistically reflect the network-topological degrees of freedom of an amorphous material, particularly in cases with a mix of rigid and flexible monomers, like a two-part epoxy.

Within these iteratively grown epoxy networks, it has been shown that in addition to updating typical topology, simulation of proper charge behavior is necessary.[55,56,66] The reaction between the epoxide ring and amine group results in the formation of a highly polar hydroxyl group. However, rather than using a charge-equilibration method, which is typically very computationally expensive, a one-time charge update is performed during the other topological updates associated with bond formation for each reaction. This accounts for the changes associated with the formation of the hydroxyl group, and is justified by the consistency in the charge transfers for various dimer and trimer structures computed with *ab initio* methods, discussed further in computational methods.

We are concerned with three main effects: system size, functionality, and stoichiometry. System size and functionality is simultaneously addressed by simulating multiple system sizes for each of the three amine combinations. The effect of stoichiometry is studied for a single functionality and system size, looking at both the over-abundance and shortage of available hardener.

3.2. Computational Methods

Several popular force fields for polymeric simulation were examined for use. In the case of the Amber95 and COMPASS potentials, we were unable to find parameters for key molecular groupings published in the literature, such as the epoxide rings.[77-80] Authors implementing COMPASS have almost exclusively done so within Materials Studio, a closed commercial code, which also limits the methods of polymerization that can be implemented. The reactive potential, ReaxFF also failed to reproduce the epoxide rings effectively when monomers were tested, with rings opening almost immediately.[81] More recently, one group has used this potential to study pyrolysis in non-crosslinked homopolymerized DGEBA systems, but their parameter modifications were unavailable at the onset of this project. Also considered were the Dreiding, CVFF and OPLS-AA potentials, which had all of the necessary parameters and have been previously used for epoxy simulations.[82-90]

The epoxide monomer, DGEBF, and two hardener monomers, DETA and TETA, were tested for stability, using initial configurations from the PubChem Compounds database.[91] While the oxirane group was stable with all potentials, the Dreiding and CVFF potentials showed significant buckling of the benzene rings of the DGEBF monomer. Additionally, the aliphatic amines were most stable in OPLS-AA according to the rate of change in the potential energy. The potential parameters we used are summarized in Appendix A, Table 2-5.

Partial charges were determined by *ab intio* methods using the Gaussian09 software and the HF/6-31G(d) exchange correlation for all three monomer structures, the reaction of the secondary amine site with DGEBF, the first reaction of the primary amine site with the DGEBF monomer and the second reaction of the primary amine site with an additional DGEBF monomer.[92] These reacted structures were first created and relaxed in the LAMMPS molecular dynamics (MD) software package, to reduce convergence time.[93] It was determined that partial charge changes upon reaction could effectively be limited to those atoms within a range of 4 nearest-neighbor sites of the newly formed bond. While the initial partial charges of the DETA and TETA monomers differ, the magnitude of the change in partial charges upon reaction showed little difference, allowing us to use consistent values for the charge transfer throughout our simulations. Charge neutrality is of course maintained throughout. The changes in partial charge upon reaction are presented in Figure 3.2. The complete information for partial charges and changes thereof is available in Appendix B.

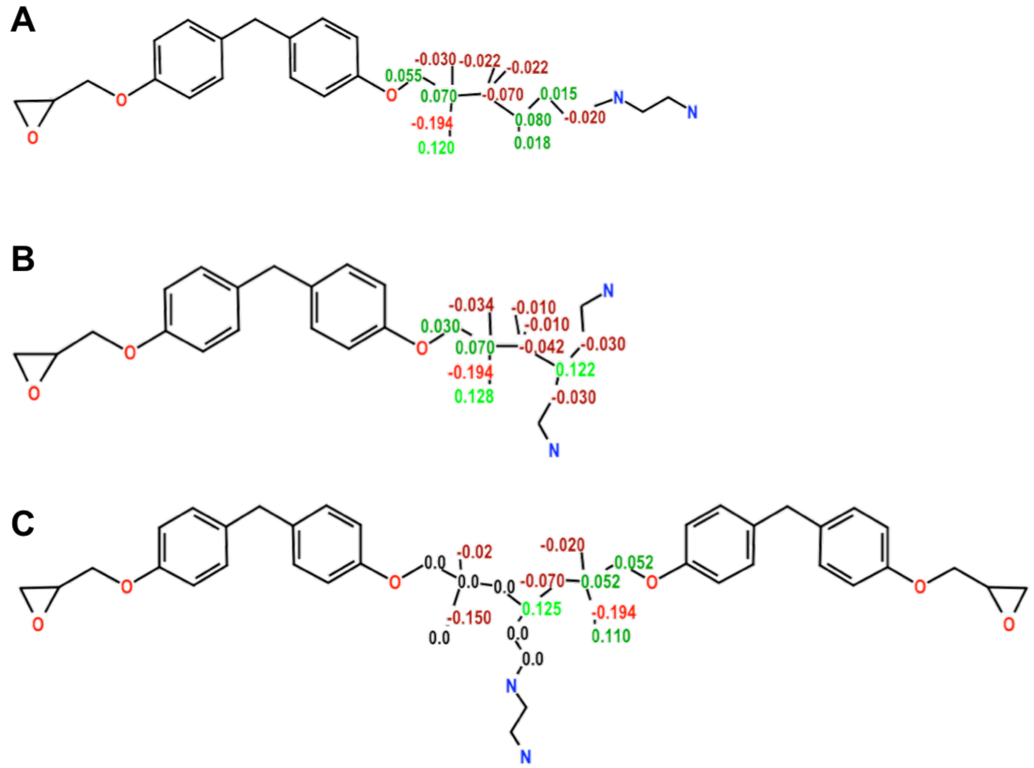

Figure 3.2. Changes in atom charge due to reaction of the epoxide and amine groups for (a) first reaction of the terminal amine, (b) reaction of the secondary amine and (c) second ration of the terminal amine. The same magnitudes are used for both DETA and TETA monomers. Green indicates a positive shift, red indicates a negative change in the partial charge.

Our simulations use a variant of the cutoff polymerization algorithm first proposed by Varshney *et. al.*[60] In the literature, the predominant amine species studied are aromatic, which have only a single type of amine site. In aliphatic amines, there are two sites: primary amine sites, with two hydrogen bonds available for reaction, and secondary amine sites, which start with a single hydrogen bond. It is well known from experimental kinetics studies that the reactivity of these two sites is not equal.[94] Therefore, we add a probability term to limit the rate of secondary amine reactions. The overall polymerization flow chart is presented in Figure 3.3.

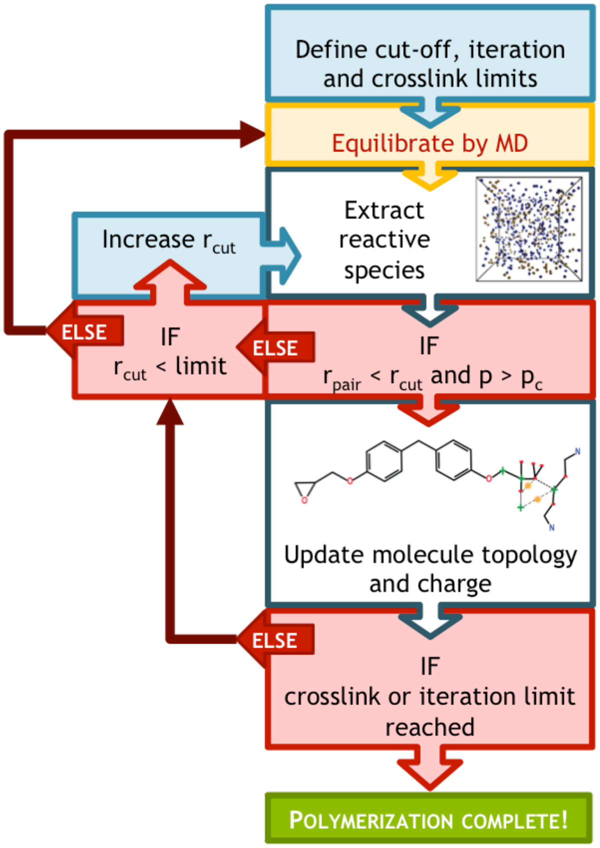

Figure 3.3. Flow chart of the dynamic polymerization algorithm used to generate epoxy networks.

The cut-off distance is defined, starting at a value roughly double the equilibrium bond length. Limits are then defined for the maximum cutoff, step size between cutoff increments, number of iterations, and maximum number of crosslinks to be formed. The structure is relaxed under constant pressure conditions at 300K using LAMMPS. The data associated with these reactive species are then extracted from the relaxed structure. The code then iterates through all reactive site pairs, calculating the separation distance. By extracting only the subset of atoms relevant to this reaction, the computational expense of this search is greatly reduced. If the separation distance is less than the cutoff value, a random number is generated to represent the probability of reaction. The critical probability of reaction is defined according to the functional group. As mentioned previously, the cut-off distance algorithm implemented by Varshney does not differentiate between functional groups, as was reasonable given the nature of the system implemented.[60] However, for a wide variety of commercially relevant polymers, it is necessary to differentiate the reactivity of functional groups.

Once a reactable pair has been identified, the bond lists are searched in order to identify all neighboring atoms participating in the bond, angles and dihedral angles that need to be updated. For these epoxy systems, a minimum of 56 parameters must be updated during a single epoxy-amine reaction. Again, we search only the relevant subsets, such as atom type or bond type. Atomic charges are also updated in accordance with Gaussian calculations of monomer, dimer and trimer states. These topology updates are summarized in Appendix C.

After topology updates are completed, the search continues through the remaining reactive site pairs. If no reactable pairs are identified within the given cutoff distance and the cutoff is below the upper limit, this value is increased, and the process repeats. By incrementally raising the cutoff term during each bond forming iteration, rather than immediately using the largest acceptable value, we prioritize the reaction of pairs with lower separations, which are physically more probable. Furthermore, by removing fully reacted carbon and nitrogen sites from their respective subsets, the computational time required for the polymerization routine is gradually reduced through the course of the simulation.

The percentage of computing time used by the Python code on average during the first 10 iterations of polymerization was determined for four system sizes, from 8,670 atoms to 75,336 atoms. Results are presented in Table 3.2.

Table 3.2. CPU time used by Python in first 10 polymerization iterations

System Size (atoms)	System Size (monomers)	% CPU-time used by Python
8670	476	0.82
22760	952	1.17
47100	1190	2.51

75336	2380	4.10

For small systems, computational time is almost entirely dependent on the large LAMMPS calculation, while initializing and looping through neighbor lists become more significant in larger structures. This is because while the LAMMPS code scales approximately linearly, the polymerization code scales between O(N) and O(N^2). This scaling allows us to reach system sizes that are larger than the majority of the published literature.

Bulk epoxy systems are being explored in terms of system size, starting with systems of 8,670 atoms and ~240 monomers to systems of 94,200 atoms and 2400 monomers. The role of amine functionality is addressed by simulating systems containing only DETA (f=5.0), only TETA (f=6.0) and an even a mixture thereof (f=5.5). The effects of stoichiometry are explored for the ~1200 monomer TETA system. Three random starting geometries have been created for each initial system size/chemistry, allowing for better statistics and averaging.

Initial structure generation was a particular challenge. Unlike for long-chain polymers, Theodorou and Suter's random walk chain method is not particularly applicable here.[95] Instead, a low-density system of unreacted monomers was generated by inserting monomers at random positions and orientations within a pre-allocated box, and rejecting insertions that would result in overlap as defined by a cutoff criterion. This is shown schematically in Figure 3.4.

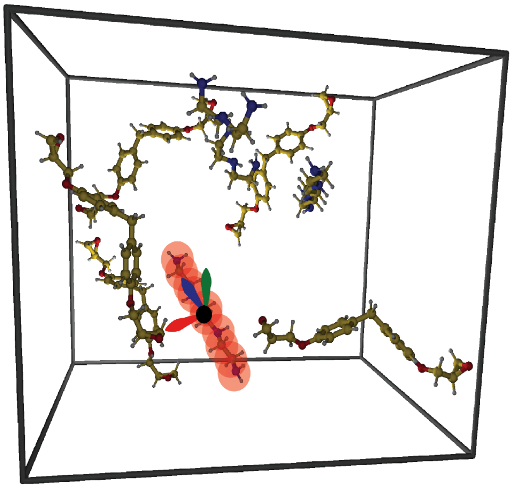

Figure 3.4. Schematic demonstrating the insertion of a monomer into a box with radial cutoff checks for overlap with previous atoms.

To densify this structure, an extended molecular dynamics relaxation and compression sequence was applied. The initial densification is performed with a time step of 0.5fs, with minimization under a pressure of 100 atm, followed by a constant deformation at elevated temperature, held at constant pressure at that temperature, before being cooled under pressure and ultimately relaxed to atmospheric. Use of a shorter relaxation sequence resulted in structures of a lower density, which failed to achieve expected degrees of reaction. Moreover, the inclusion of voids can result in problematic mechanical property analysis.

Mechanical properties were determined within the NPT ensemble, using a constant deformation rate of 10^7/s. This is a very high strain rate compared to the experiment, but slower strain rates are unfeasible due to the long simulation times required. This strain rate and ensemble was determined by comparing various techniques in the literature, and selected according to magnitude of the pressure fluctuations and the quality of fit of the elastic regime. Stresses are determined using the virial stress definition as implemented in the LAMMPS code.[96] The stress-strain curves presented show time-average data for clarity, but elastic properties are computed using all available data points.

Simulations were run using a combination of high performance computing resources provided by the University of Michigan Center for Advanced Computing and Xsede, the Extreme Science and Engineering Discovery Environment, supported by NSF and maintained by the Texas Advanced Computing Center.

3.3. Results and Discussion

Structure During Network Growth

Characterizing the structure of a bulk polymer network can be challenging, as polymeric networks have large network units compared to inorganic glass systems, which can result in more complexity. The flexibility of the amine chains is another challenge. Typical metrics for polymer systems include density, pair correlation functions, and molecular weight. In addition to these metrics, some analogies to commonly used methods to quantify inorganic glasses have been applied, such as tracking the connectivity of network units. Whenever possible, the structural evolution during cure is tracked. However, given the number of systems prepared during the course of this study, it is not always be feasible to present all results and a representative example will be presented.

For the low-shrinkage two-part epoxy resins, a volume change of 1-2% during the curing process is a reasonable expectation. The uncured structure was compressed to a target density of ~1.2g/cm^3, based on experimental values, with some expected variations due to the use of the nVT ensemble. The density is then monitored as a function of the degree of conversion to ensure the expected shrinkage is observed. Results for the density as a function of cure are presented in Figure 3.5.

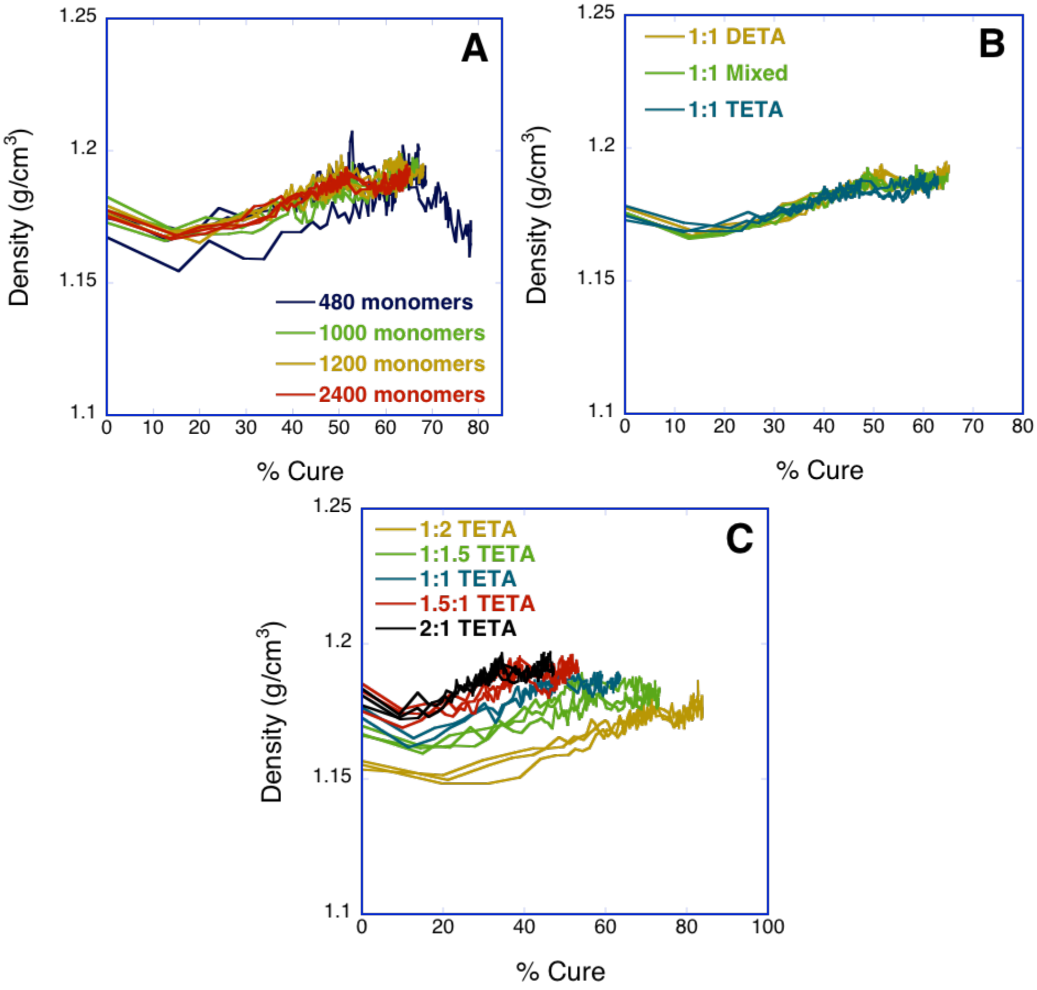

Figure 3.5. Overall density as a function of cure for (a) different system sizes, (b) amine functionalities and (c) overall stoichiometry, indicating the resin-to-hardener ratios.

In Figure 3.5(a), almost all of the systems simulated follow the same densification trend, showing an initial decrease in density from the liquid state to the start of cure, with the density increasing after the first cure iteration. The net volume change ranges from 0.9% to 1.7%. The exception is of one of the three initial configuration of the smallest system size. The system started at a lower initial density, failing to achieve the same condensation seen in the other 23 configurations simulated with the resin-to-hardener stoichiometry balanced. It also shows anomalous behavior above 65% cure, showing a decrease in density. This particular system is also an outlier in several other analyses, but is included to show the sensitivity of the simulations to initial configuration and size. The shrinkage behavior is even more consistent for the different amine functionalities, as seen in Figure 3.5(b). The differences in initial densities of the different stoichiometries, seen in Figure 3.5(c), largely reflect the different densities of the two monomer types. However, the amine rich system, 1:2 TETA (gold), shows a more gradual densification with cure than the amine poor 2:1 TETA system (black).

As another way to examine the bulk structure, the pair correlation functions are a valuable method for verifying the distribution of bond lengths and non-bonded pairs in a system. This was calculated for the intermediate size of the DETA systems, with 1200 monomers, during the progression of cure, presented in Figure 3.6.

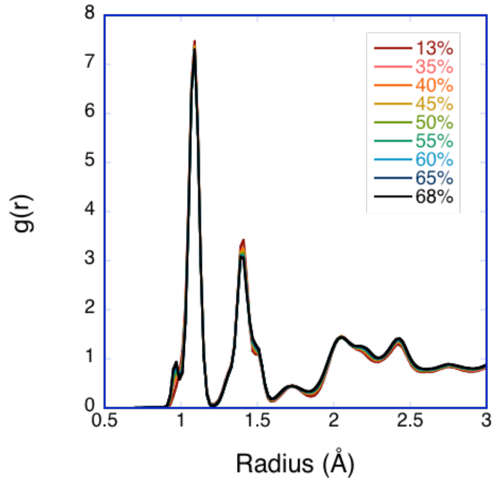

Figure 3.6. The bulk pair correlation function of a 1200 monomer DETA system as cure progresses

Only the first three angstroms are shown, as differences between the different degrees of conversion are negligible at larger separations. As cure progresses, a shoulder begins to appear at 0.9Å, associated with the formation of the hydroxyl group. The peak at 1.4Å decreases in magnitude, while the shoulder at 1.5Å increases as the oxirane rings are opened and the average C-O equilibrium length increases. The addition of C-N bonds during polymerization is less obvious, as they are at the same equilibrium distance as the bonds inherent to the aliphatic amines.

Another common experimental method for monitoring the polymerization process is to track the molecular weight of the system. While there are several different ways to define the average molecular weight, the mass-average molecular mass is used in a number of models for predicting the mechanical behavior of polymer materials.[24]. It is defined according to Eq. 3.1 as:

$$\overline{M}_w = \frac{\sum_i N_i M_i^2}{\sum_i N_i M_i}$$

Eq. 3.1. Mass-average molecular weight

where N_i is the number of molecules of mass M_i for a given size, i. This is computed as a function of cure for each system, and presented in Figure 3.7.

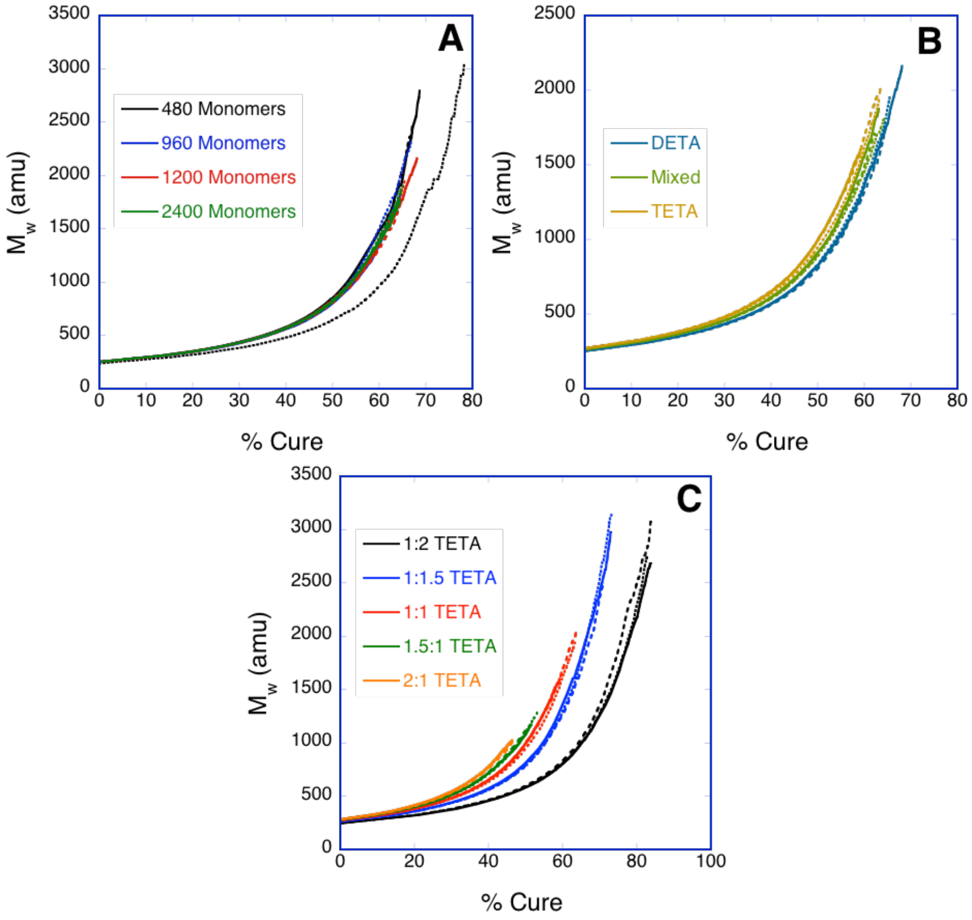

Figure 3.7. The mass-average molecular weight as a function of cure for (a) different system sizes, (b) amine functionalities and (c) overall stoichiometry, indicating the resin-to-hardener ratios. Three different initial configurations are shown for each chemistry.

Molecular weight increases slowly initially, before dramatically increasing between 40% and 50% cure in stoichiometrically balanced systems. This occurs at the expected onset of gelation according to Flory-Stockmayer models. The different system sizes, in Figure 3.7(a), show little variation, except for the one system, which was previous identified as an outlier for having a lower density. Amine functionality, presented in Figure 3.7(b), again shows only minor variations. As expected, the slightly longer aliphatic chain has a slightly higher molecular weight at an equivalent degree of cure. Meanwhile, changing the stoichiometry of the system affects the molecular weight evolution most significantly, as shown in

Figure 3.7(c). In systems with more epoxide resin than amine hardener M_W begins to increase at lower degrees of cure than stoichiometrically balanced systems, while amine-rich systems do not show a dramatic increase in M_W until over 60% cure.

These average values alone do not tell the complete picture of network growth. In order to examine the proportions of small clusters to large clusters, the molecular weight dispersity was also determined as a function of cure. The dispersity of a polymer network is defined in Eq. 3.2 as

$$Đ_M = \frac{M_w}{M_n}$$

Eq. 3.2 Definition of dispersity of molecular weights

where mass-average molar mass is defined previously in Eq. 3.1, and number-average molar mass is defined by Eq. 3.3 as:

$$\overline{M_n} = \frac{\sum_i N_i M_i}{\sum_i N_i}$$

Eq. 3.3. Number average molecular weight

with M_i and N_i as previously defined. The calculated dispersity values as a function of cure are presented in Figure 3.8.

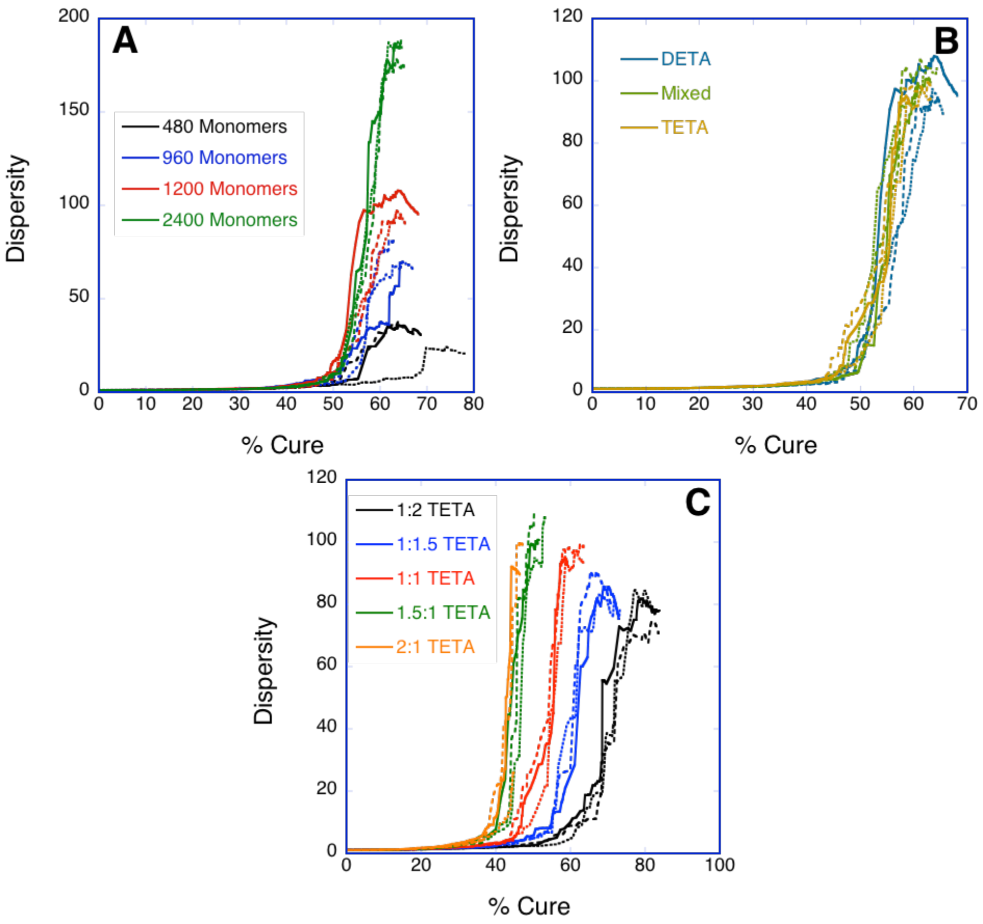

Figure 3.8. The computed dispersity as a function of cure for (a) different system sizes, (b) amine functionalities and (c) overall stoichiometry indicating the resin-to-hardener ratios. Three initial configurations are shown for each resin and hardener chemistry.

Our values for dispersity are unphysically high, as the small, finite nature of our systems results in erroneous statistical behavior. The finite population sizes, particularly at high degrees of conversion, result in a greater divergence of the two methods of computing average weight than would be seen However, it is still a useful way to compare network growth between systems. The four different system sizes in Figure 3.8(a) almost all show a rapid increase in dispersity around 50% cure, which then begins to decrease around 60% cure. A large value in dispersity indicates a biomodal mixture of small and very large clusters, and this rapid increase is associated with the initial formation of an infinite cluster, where the majority of the mass of the system now belongs to that single molecule. The inflection corresponds to point where new bonds are joining smaller clusters to the infinite cluster, reducing the total number of molecules. This trend continues for the different amine functionalities, shown in Figure 3.8(b). However, changing the ratio between resin and hardener has the strongest effect on dispersity. In resin-rich mixtures, the amount of resin converted before the formation of an infinite cluster than in resin-poor mixtures. Even at relatively low degree of epoxide conversion, the resin-rich systems show this characteristic increase. On the other hand, the amine-rich system does not form the infinite cluster until almost 70% conversion of resin. This indicates that even though the conversion of the oxirane groups is accelerated by the addition of more hardener, network formation is delayed.

Molecular dynamics simulations make it possible to perform more specific analyses of the molecular weights of the system. For a 1200 monomer DETA system, we examine the cumulative distribution of the molecule sizes of one system as cure progresses. The data in Figure 3.9 represents the fraction of system's mass that is accounted for up to the molecular weight given by the abscissa values.

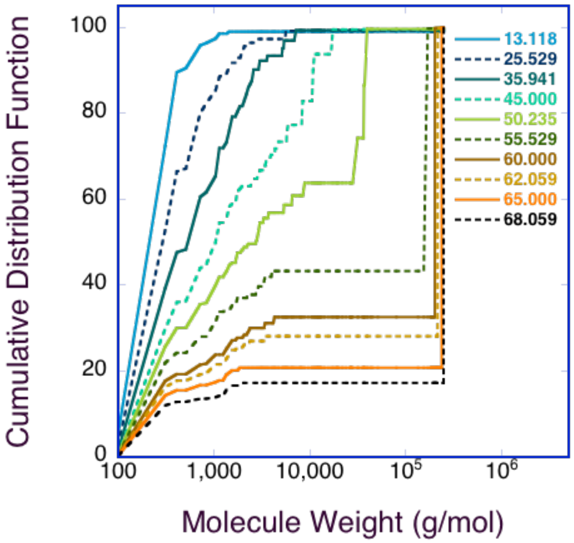

Figure 3.9. Normalized cumulative distribution of the molecular weight in the system at various degrees of cure in the 1200 monomer 1:1 DGEBF:DETA system.

The lowest two masses represent the two monomer species of the system, which are depleted as cure progresses. For systems which are only beginning to cure, there is a fairly continuous distribution of sizes, while at higher cures, we can see a bimodal behavior, with molecules either being unreacted monomers, or part of the large “infinite” cluster. This is apparent by the horizontal segment in the cumulative distribution function. Below 50% cure, there is a fairly continuous distribution of sizes. Beyond 50% cure, which is the expected onset of gelation accordingly to Flory-Stockmayer theory, there is a distribution of smaller clusters, and a large continuous cluster that continues to grow as cure continues. This agrees with the results of the dispersity analysis, where there was a sudden increase at the same point.

The different stoichiometries showed the most variable behavior in terms of both their evolution of mass-average molecular mass and dispersity. This is demonstrated for an amine-rich system, a stoichiometrically balanced system, and an amine poor system, as shown in Figure 3.10.

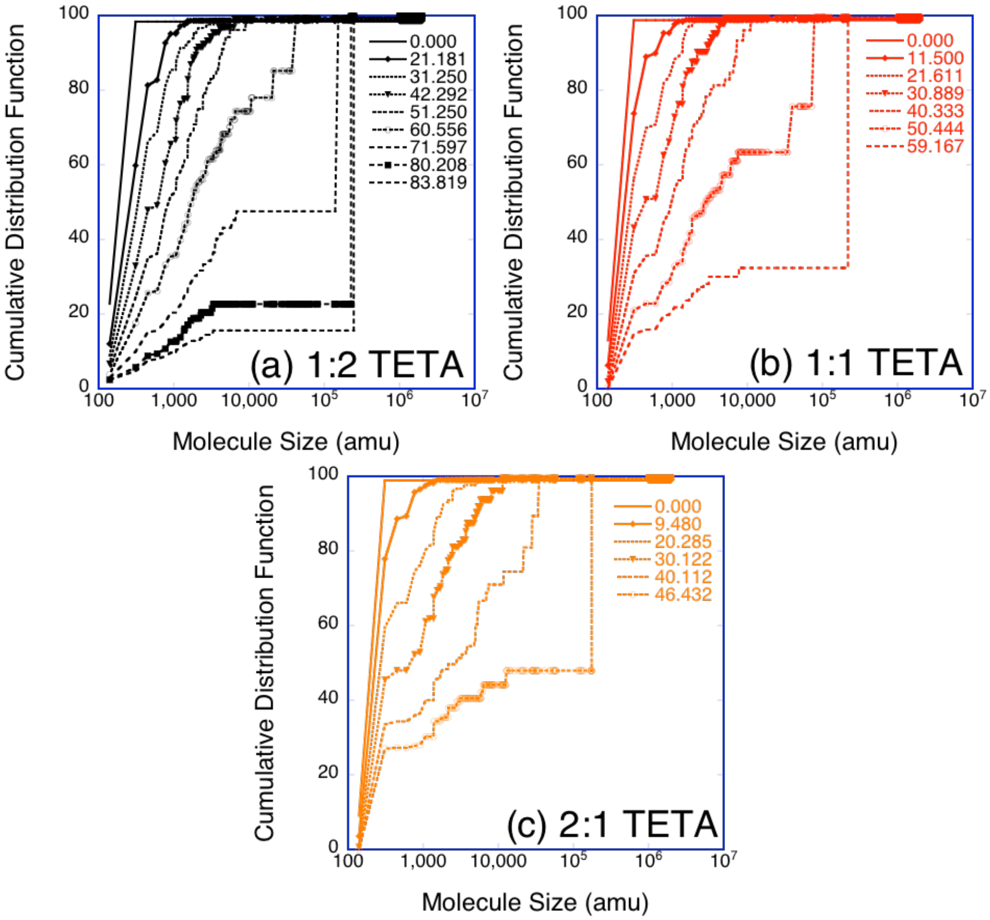

Figure 3.10. Cumulative distribution of molecules of mass, *M_i*, at various degrees of cure for (a) amine-rich (b) balanced (c) amine poor

The cumulative distribution of molecular weights is shown for approximately every 10% change in cure, up to the maximum available degree of cure for each system. In agreement with the previous dispersity results, the amine-rich system, in Figure 3.10(a), has a fairly continuous distribution of sizes until nearly 70%, when it transition into a bimodal size distribution. For the system in which resin and hardener concentrations are balanced (Figure 3.10b), the transition to bimodal distribution occurs just above 50% cure, while for the amine-poor system (Figure 3.10c) the transition is already manifest at 46% cure.

In all cases, the smaller polyfunctional amine monomer seems to be depleted more rapidly than the epoxide resin. Tracking the number of monomers in the system in Figure 3.11, we can verify that the amine hardener is more rapidly depleted than epoxide resin, given stoichiometric mixing.

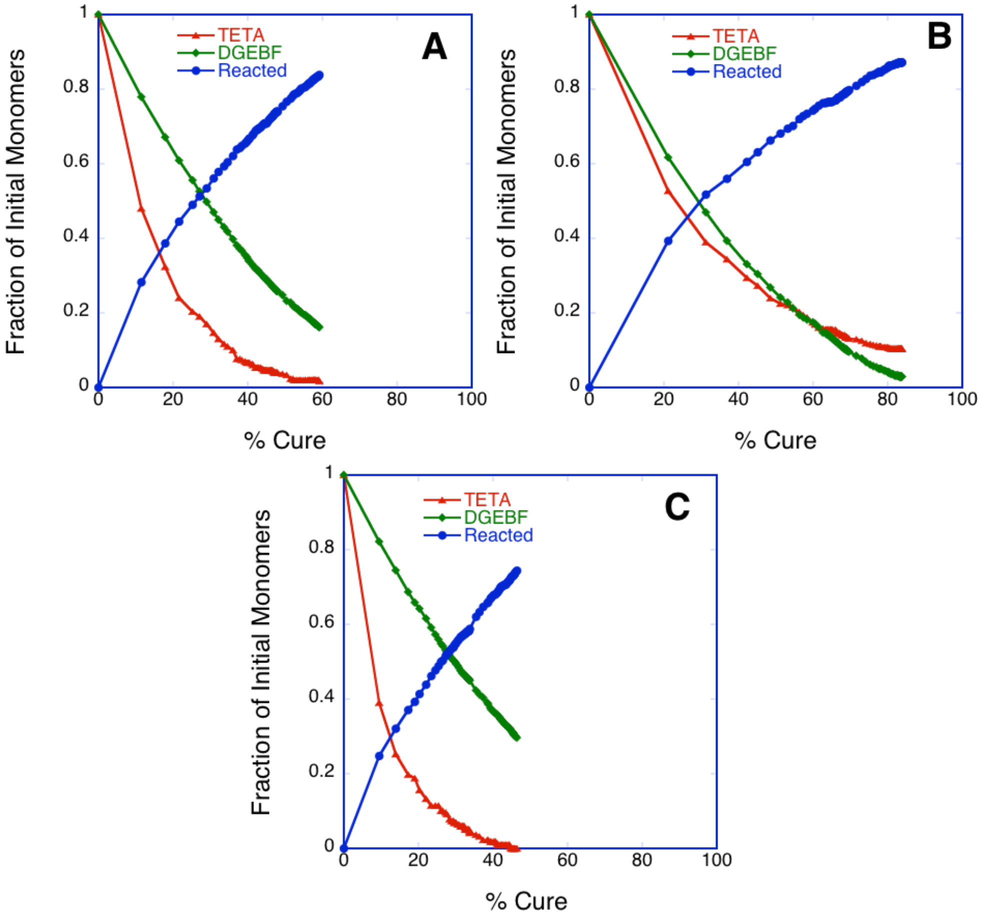

Figure 3.11. The number of monomer molecules in the system for unreacted TETA hardener(red triangles), unreacted DGEBF resin (green diamonds) and cumulative number of reacted monomers (blue circles) for (a) 1:1 DGEBF:TETA (b) 1:2 DGEBF:TETA and (c) 2:1 DGEBF:TETA

Even at fairly high degrees of conversion, there are completely unreacted DGEBF molecules. In the amine rich system, with twice as many available amine functional groups as epoxide groups, the amine depletes at almost the same rate as DGEBF. However, in the stoichiometrically balanced and amine poor cases, the TETA is rapidly depleted, leaving substantial amounts of unreacted DGEBF monomer in the system. This indicates that while it is theoretically possible for the amine monomer to form up to six links, this is a very uncommon situation. This is also reflected in the examination of amine connectivity. The number of TETA monomers with a particular number of links as a function of cure is presented in Figure 3.12.

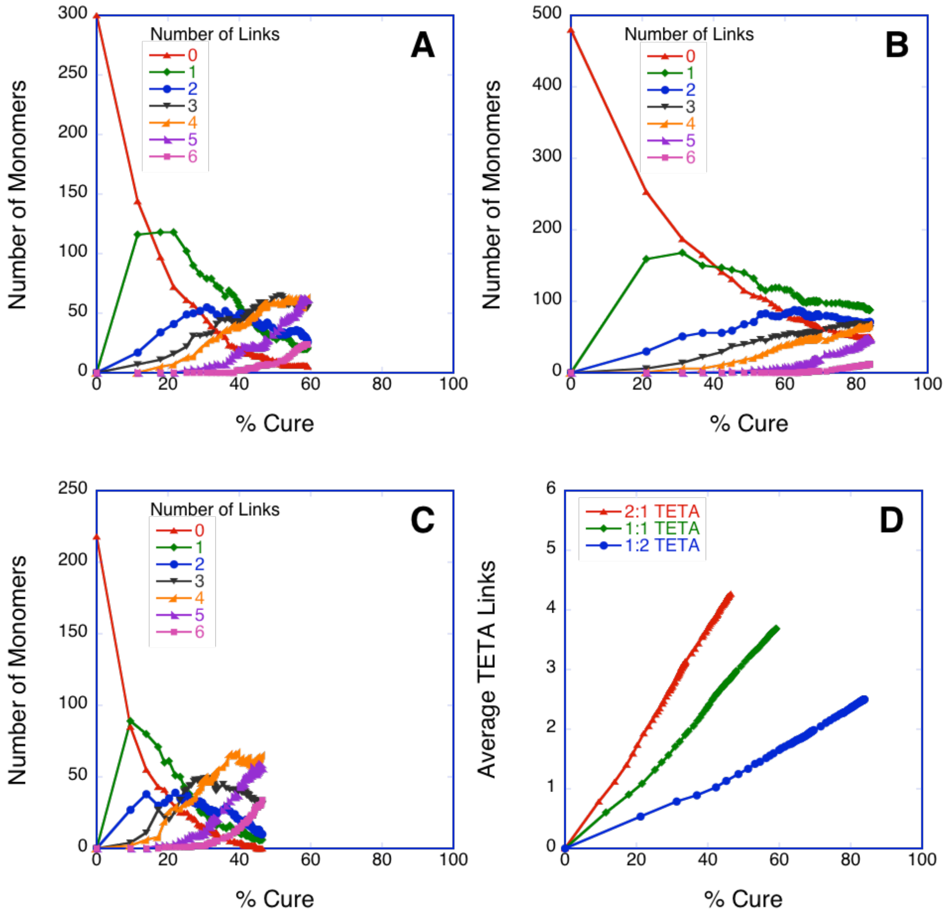

Figure 3.12. The number of reacted amine sites for a given monomer for (a) 1:1 TETA (b) 1:2 TETA (c) 2:1 TETA and (d) average amine connectivity for the three systems.

The behavior of the unreacted TETA monomer has been discussed previously in Figure 3.11. In the evenly mixed and amine-poor systems, shown in Figure 3.12(a) and (c), the number of monomers that have reacted only once reaches a maximum very quickly, and is rapidly depleted as additional sites react. Moreover, it seems that these monomers are more likely to react a second time, even though reactivity favors the first reaction of the terminal amine site. A similar maximum is also seen for the amine monomers with two links, at 30% cure. At this point, we expected cross-links to start forming, rather than simply continued chain growth. In contrast, the amine-rich system shown in Figure 3.12(b) has a gradual depletion of singularly bonded amine monomers, and maintains substantial fractions of amines with only two links at high degrees of cure. As expected, the number of fully reacted amines is highest in the amine-poor 2:1 TETA system, with almost no fully converted amine observed in the amine-rich 1:2 TETA system.

An amine monomer can be considered a "cross-link" when 3 or more bonds are formed, joining multiple chains together, instead of simply increasing the effective chain length. The stoichiometrically balanced and amine-poor cases both show cross-links forming at relatively low cure, while the amine rich case does not start to form cross-links until later in the cure process. To summarize the connectivity of the amine, the average number of links per monomer is shown in Figure 3.12(d). The average behavior is linearly related to the degree of cure, and the ratio between the slopes of these lines is proportional to the ratio in amine quantity. However, it is still useful to recall what this might indicate for mechanical behavior, with more amine-rich structures reaching cure sooner, but possibly reaching final mechanical properties more gradually. Additionally, the amine-rich systems are more likely to see long chains form between cross-links, which may affect the ultimate mechanical properties.

The network growth can also be qualitatively monitored through visual inspection, by rendering only those monomers in the system that have partially or completely reacted. The color indicates the size of the molecule, with the largest molecules in blue, intermediate sizes in gray and red for the smallest molecules. Snapshots are shown for several stages in the cure process in Figure 3.13.

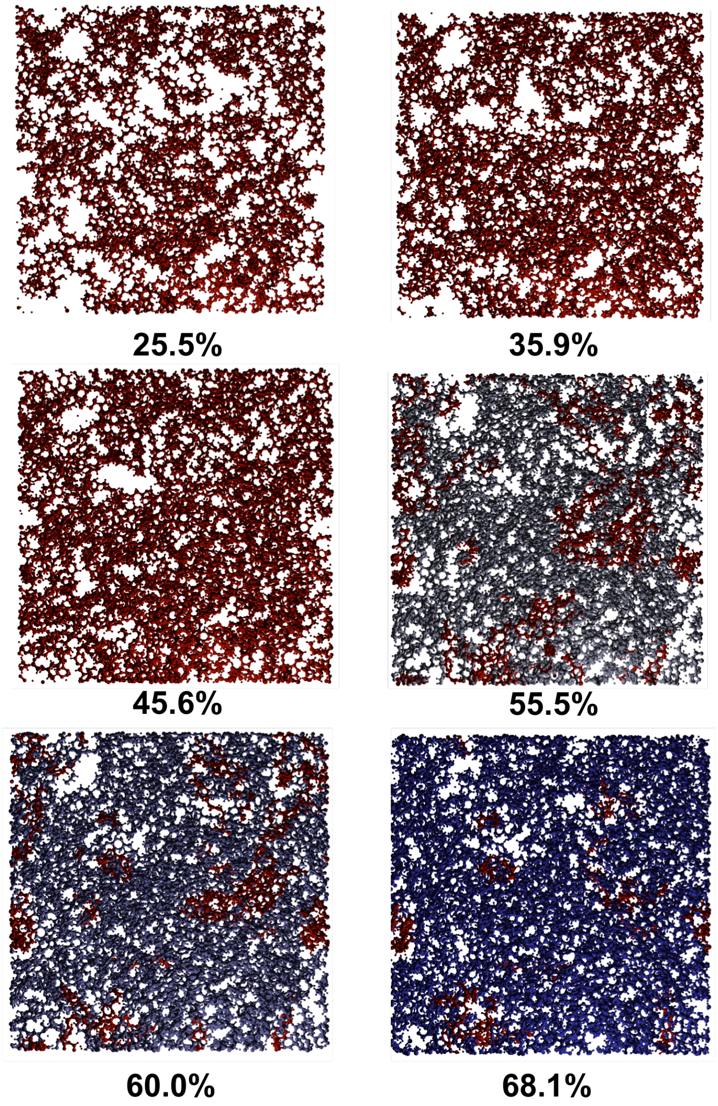

25.5% 35.9%

45.6% 55.5%

60.0% 68.1%

Figure 3.13. Network growth during cure for a 1200 monomer system. Atoms are colored according to the size of the molecule with red for small and blue for large.

The qualitative picture shows that as molecules join together, there are some clusters apparently trapped in pockets, unable to join the network due to steric hindrance. If we reverse the selection criteria, and instead render only the unreacted monomers remaining in the structure, we can see pockets of DGEBF (red) and a few isolated DETA monomers (blue) in Figure 3.14.

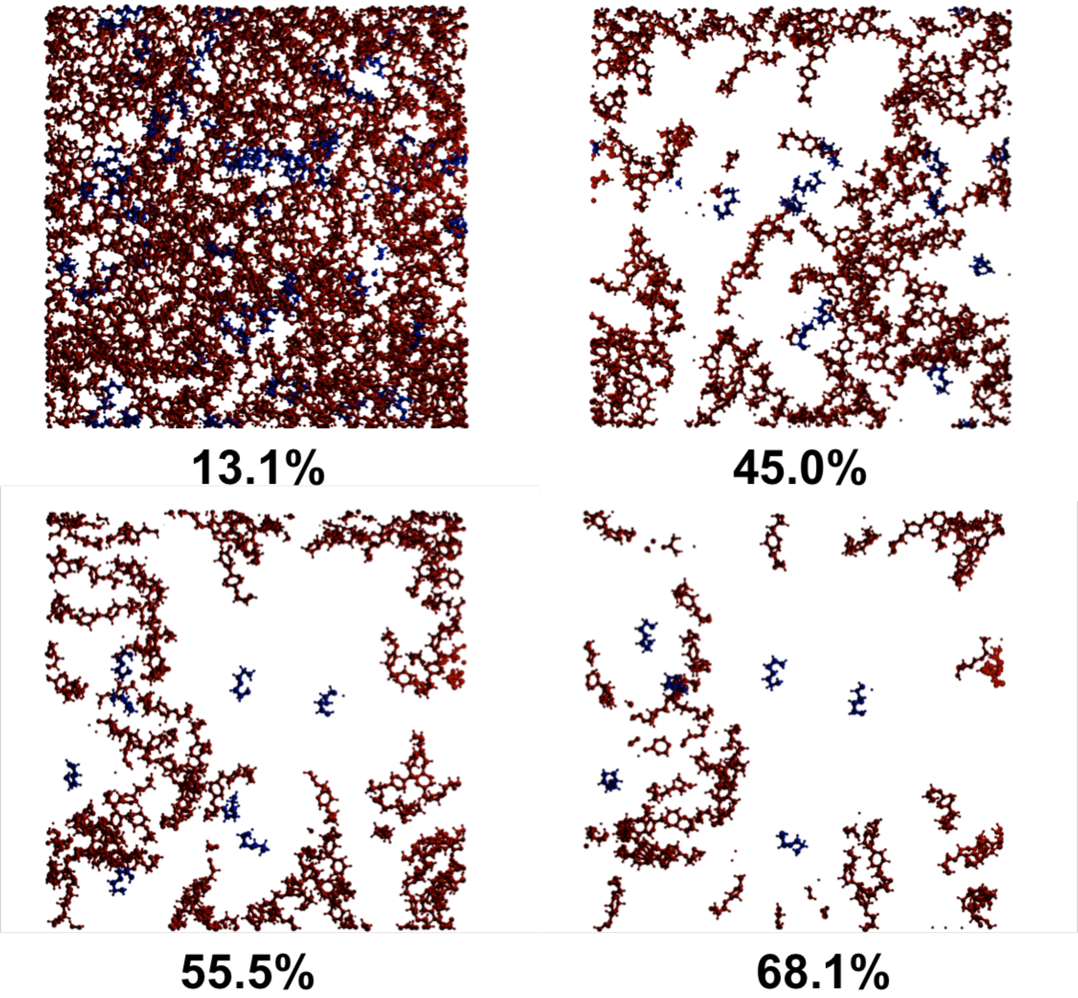

13.1%

45.0%

55.5%

68.1%

Figure 3.14. Unreacted monomers remaining in a 1200 monomer DETA system at various degrees of cure, with DGEBF and DETA colored as red and blue, respectively.

When viewing only the completely unreacted monomers, the role of mixing and steric hindrance becomes more early evident. The majority of the unreacted DGEBF monomer is in small clusters, rather than spread through out the system, while the remaining free amine monomers are clearly surround by reacted polymer. This mixing and depletion of the epoxy and amine monomers can also be seen by looking at the different resin-to-hardener ratios, shown in Figure 3.15.

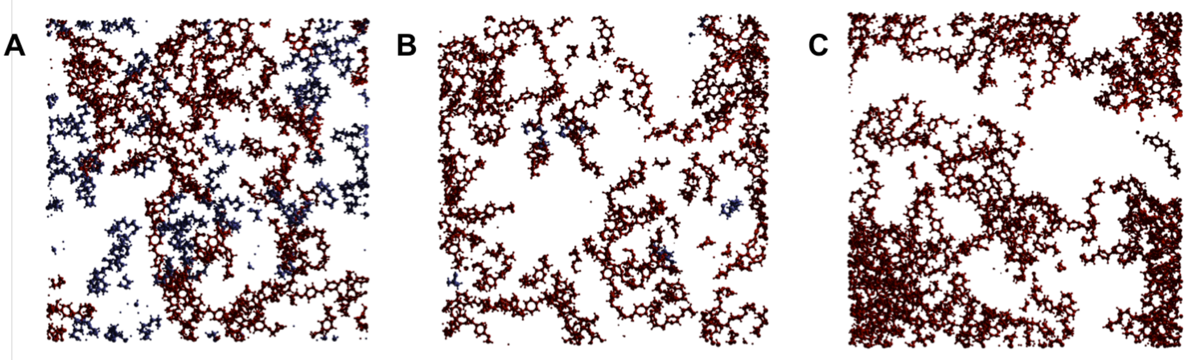

Figure 3.15. The unreacted monomers remaining in the system at 45% cure for (a) amine-rich (b) stoichiometrically balanced and (c) amine-poor epoxy systems.

In the amine-rich case, seen in Figure 3.15(a), both DGEBF and TETA monomers are still present, but are typically segregated. In the other two cases, the amine has largely been depleted, but it is clear that the unreacted DGEBF monomer is not distributed evenly across the system.

Another concern during network formation is the generation of local stresses. In the interest of simulation time it is necessary to create bonds longer than the equilibrium distance. This has the potential to result in large residual stresses in the system, beyond what might be expect from experiment.[2] The per-atom virial stress was calculated in LAMMPS, according to Equation 3.4. This results in units of MPa*V, as the volume of a single atom is not particularly physically meaningful.

$$S_{ab} = -\left[\begin{array}{l} \frac{1}{2}\sum_{n=1}^{N_{pairs}}\left(r_{1a}F_{1b} + r_{2a}F_{2b}\right) + \frac{1}{2}\sum_{n=1}^{N_{bonds}}\left(r_{1a}F_{1b} + r_{2a}F_{2b}\right)\ldots \\ \ldots + \frac{1}{3}\sum_{n=1}^{N_{angles}}\left(r_{1a}F_{1b} + r_{2a}F_{2b} + r_{3a}F_{3b}\right) + \frac{1}{4}\sum_{n=1}^{N_{dihed}}\left(r_{1a}F_{1b} + r_{2a}F_{2b} + r_{3a}F_{3b} + r_{4a}F_{4b}\right)\ldots \\ \ldots + Kspace\left(r_{i_a}, F_{i_b}\right) \\ \end{array}\right]$$

Eq. 3.4 Per-atom virial stress

where *a* and *b* are the respective *x*, *y* or *z* directions to generate the six components of the tensor, *r* is the position of the atom, and *F* are the respective forces as defined by the coefficients and functions of the particular forcefield. As indicated by the leading coefficients, the contribution of the energy is equally divided among all atoms involved, e.g., three atoms per angle, etc. In the case of the OPLS force field, pair forces are defined according to the Lennard-Jones 12-6 potential, bonds and angles are based on a harmonic spring model, and an alternating cosine series function for of the dihedral angle. The equations for each of these terms are given in Eq. 3.5.

$$F_{pair} = 4\varepsilon\left[\left(\frac{\sigma}{r}\right)^{12} - \left(\frac{\sigma}{r}\right)^{6}\right]$$

$$F_{bond} = K\left(r - r_0\right)^2$$

$$F_{angle} = K\left(\theta - \theta_0\right)^2$$

$$F_{dihed} = \frac{1}{2}K_1\left[1 + \cos(\phi)\right] + \frac{1}{2}K_2\left[1 - \cos(2\phi)\right] + \frac{1}{2}K_3\left[1 + \cos(3\phi)\right] + \frac{1}{2}K_4\left[1 - \cos(4\phi)\right]$$

Eq. 3.5 Force field equations for the pair, bond, angle and dihedral components

The distribution of per-atom stresses are presented as a function of cure in Figure 3.16(a), and then deconvoluted according to atom type in Figure 3.16(b). The sign convention is such that positive stress are compressive, and negative stresses are tensile.

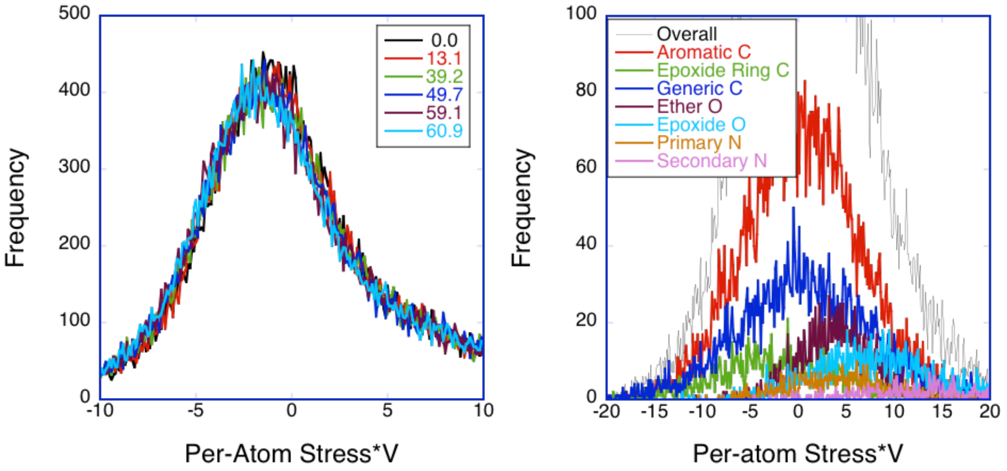

Figure 3.16. (a) Distribution of per-atom stresses as a function of cure in a 1200 monomer system and (b) the distribution of stress by atomic species at 60.9% cure

All systems show a nearly identical Gaussian-like distribution. However, there is a shift in the overall system stress towards a net tension as an infinite periodic network is formed. To verify that a single species was not under unusually high forces, the per-atom stress for the all species, except for hydrogen, in the uncured sample is shown in 16(b). As expected, aromatic and aliphatic carbon atoms in the structure have a stress distribution centered at zero, while more polar atoms, such as oxygen and nitrogen, or geometrically constrained atoms, such as the oxirane carbon, are shifted from a neutral average. This also partially explains why the overall shift of the net stress is not as dramatic as might be expected due to shrinkage during network formation: these stresses are in part being countered by the stress reduction from the opening of the oxirane rings.

The formation of an epoxide network has been structurally characterized, looking at system size, amine functionality, and stoichiometry. The expected volumetric shrinkage of ~1% was observed in all cases, in agreement with experiment, and no anomalous behavior was seen in the pair correlation function. Tensile stresses were generated as a function of cure, but were not excessive.

The mass-average molecular weight, dispersity and cumulative distribution of molecular weights demonstrated an initial constant growth of small clusters, before molecules join to form an infinite network. While systems with a surplus of amine hardener reach higher degrees of epoxide conversion, the formation of an infinite network is delayed.

From examination of the renderings of first the network by molecule size, and then the unreacted monomers, it is clear that steric hindrance prevents complete conversion. While 60-70% of the epoxide functional sites had reacted with the amine, the majority of the unreacted monomers were DGEBF unless there was a substantial surplus of amine. The connectivity of the amine as a function of cure again showed that while the conversion of epoxide is higher in the amine-rich case, the formation of potential crosslink is delayed compared to stoichiometrically balanced or amine-poor systems.

Mechanical Characteristics

Having characterized the as-cured epoxy structures, the mechanical properties of the system are explored by a simple uniaxial tension test with a constant deformation rate, under the constant pressure ensemble. This allows the system to shrink in the directions normal to the tensile strain being applied. The stress is determined according to the virial stress definition, as given in Eq.4.

By definition, the value derived by the virial stress for each atom is in units of stress*V. The uniaxial stress of the system is determined by summing the per-atom stress in the direction of tension, and normalizing with respect to the volume of the system. The sign convention is now to have tensile stresses positive, as all simulations are preformed in tension. An average value is then taken every 100 times steps to generate the stress-strain curves, though elastic properties will be determined from all available data points. An example series of stress-strain curves for the 1200 monomer DETA system at various points in cure are presented in Figure 3.17.

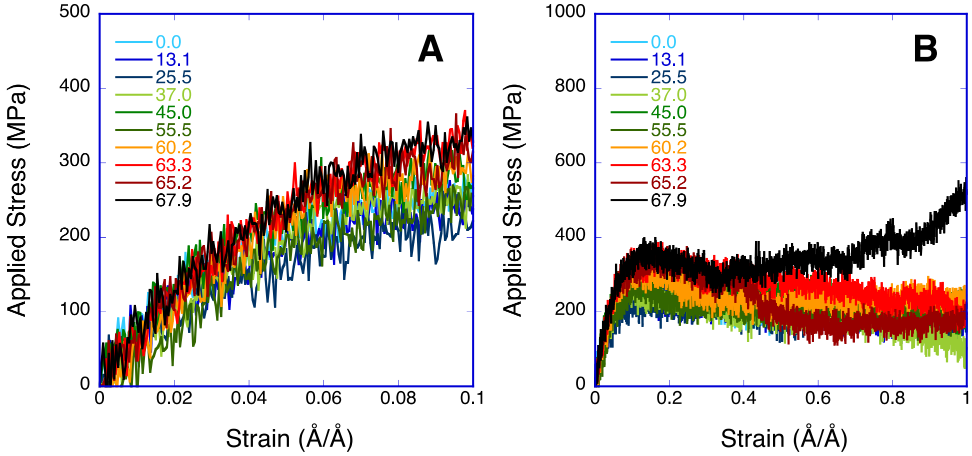

Figure 3.17. Stress-strain curves for a uniaxial tension test at a constant strain rate for a 1200 monomer DETA system during cure looking at (a) the elastic regime and (b) up to 100% elongation

Looking only at the low strain regime in Figure 3.17(a), it is clear that the elastic behavior of these systems is nonlinear. In the overall stress-strain curve, in Figure 3.17(b), there is a clear maximum marking the onset of necking, where void nucleation is expected, as well as a second inflection around 30% strain indicating the onset of the drawing phase. The tensile limit seems to increase slightly as a function of cure, which will be explored in more detail later. The effect of system size on the stress strain curve can be seen in Figure 3.18.

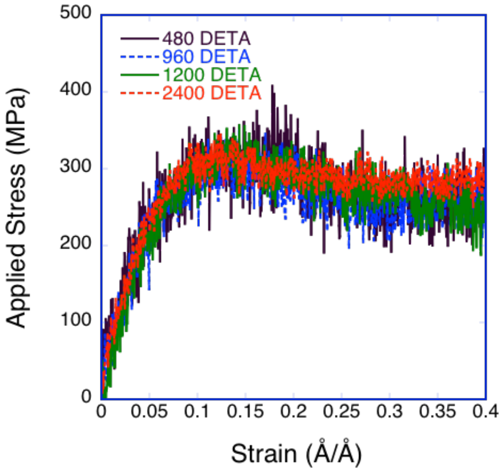

Figure 3.18. Uniaxial tension stress-strain curves for systems of 480, 960, 1200 and 2400 monomers at ~60% cure.

The systems compared in Figure 3.18 are all of the same functionality and as close to the same degree of cure as was available. Most obvious is the difference in the magnitude of the fluctuations in the stress as a function of strain. The largest system, 2400 monomers, results in a much cleaner stress-strain curve, which is important for confidence in the accuracy of any subsequent analysis of the mechanical properties of the system.

As noted above, the elastic regime of these simulations is distinctly nonlinear. Accordingly, the Young's modulus is determined by taking the tangent at zero strain, evaluated based on a parabolic fit of the complete stress-strain data from 0 to 5% strain. These moduli as a function of cure for various systems are presented in Figure 3.19.

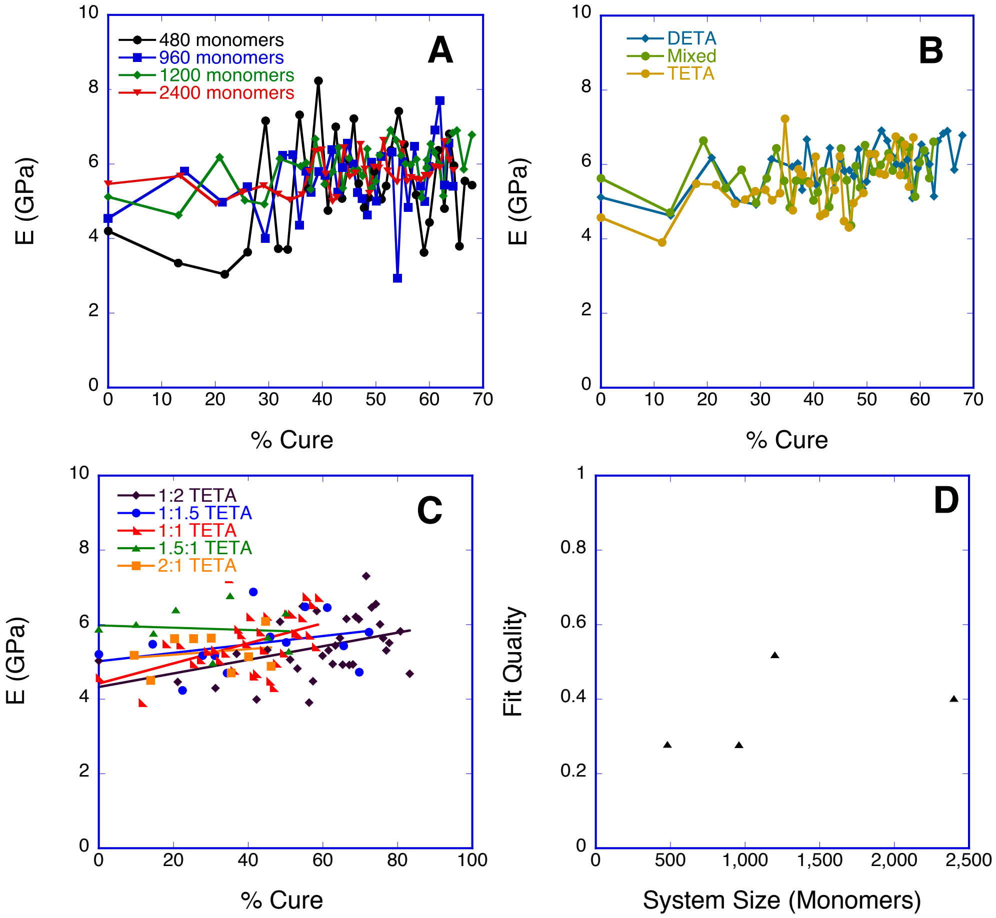

Figure 3.19. Young's modulus at 0% strain for (a) four different system sizes (b) different functionalities and (c) different stoichiometric mixing, indicating the resin-to-hardener ratios (d) comparison of linear fit quality of modulus versus curefor the system sizes presented

In all cases, there is a slight increase with modulus as a function of cure. The effect of functionality, seen in Figure 3.19(b), continues to be negligible. Unexpectedly, there is also no obvious trend based on the stoichiometry of the system in Figure 3.19(c). While differences are expected, the amount of variance in the calculation is larger than the variance between systems studied. System size does not affect the modulus specifically, but clearly impacts the reliability of the results, shown in Figure 3.19(d). Larger systems have smaller variance, as determined from the R-value of a linear regression. It is important to note that even the smallest simulation presented here is larger than many published in the literature.

To understand these relatively small shifts in Young's modulus observed with increasing network connectivity, we first examine the distribution of local stresses, focusing on the atom types associated with bonds added to the system during cure. Three atom types in particular were identified: the carbon from the epoxide ring that bonds to the nitrogen, the partially reacted terminal nitrogen, and any fully reacted nitrogen atom.

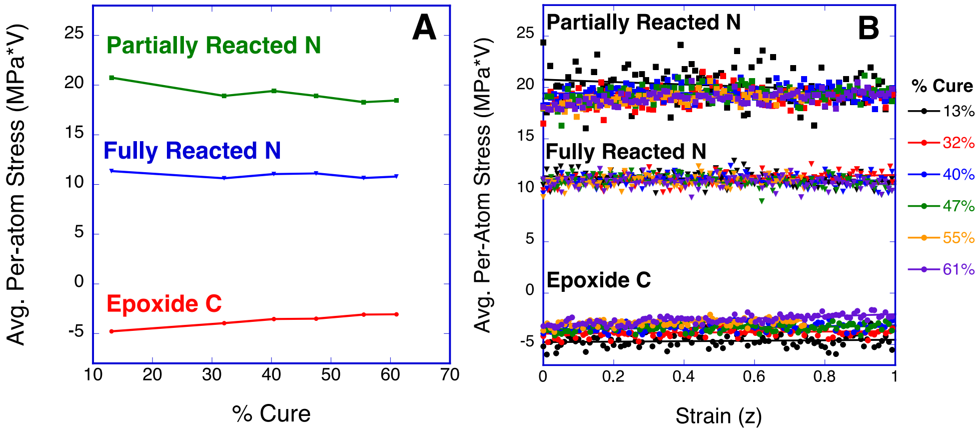

Figure 3.20. The average per-atom stress for atom types associated with the formation of new network bonds (a) as a function of cure at 0% strain and (b) as a function of strain for various cures

These stresses exhibit a similar distribution as shown earlier. We therefore give an average value for the stress of each atom type. As the reaction-relaxation process progresses, the average stress on atoms in network-forming bonds tends towards zero. During the uniaxial tensile test, there is a shift in the average per-atom stress, particularly evident for the carbon in the epoxide resin that has been bonded to the amine. This indicates that some fraction of the load is being transported through the network. However, within the elastic regime, there is no visible trend in the per-atom stress as a function of strain. To further clarify the mechanism of deformation, the length of the resin and hardener repeat units are tracked as a function of strain. In the case of the aliphatic amine, the terminal N groups are used to determine the length, while the epoxide monomer is measured from the carbons at the point of the original oxirane rings. The distribution of monomer lengths as a function of strain is presented in Figure 3.21.

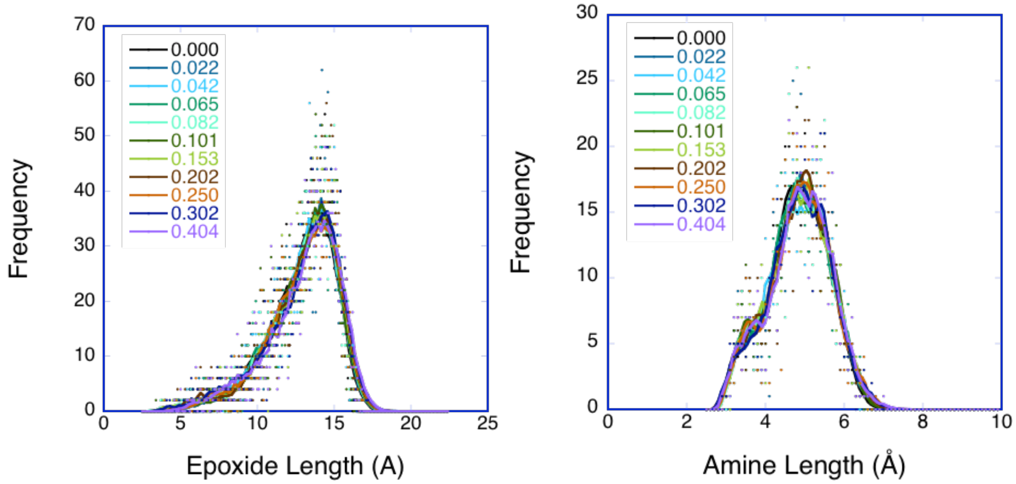

Figure 3.21. The distribution of monomer lengths at various values of strain for (a) DGEBF and (b) DETA in the 1200 monomer DETA system at 61% cure.

Neither species shows a significant shift in repeat unit length as strain is applied to the system, as the curves for up to 40% strain are directly on top of one another, with no shifting towards higher lengths. This implies that even for systems at 60% cure, entanglement is the dominant deformation mechanism. Looking beyond the initial elastic region, where only minimal differences were observed, the stress-strain curves for the uniaxial tension simulations show a cusp around 12% strain associated with the onset of necking, and a minimum at a strain between 25% to 50%, indicating the start of the drawing phase. The tensile stress at the onset of necking was determined by finding the maximum stress below 20% strain, and taking the average stress for a 1% strain window around this point. While necking is unclear at the nanoscale due to periodic boundary conditions, a better term for this phase of highly localized deformation has not been found. The maximum of 20% strain was chosen to avoid the high stresses in the extreme strain regime seen in some systems, while the stress averaging was done to avoid false deviations due to natural system fluctuations. Results as a function of cure are presented in Figure 3.22.

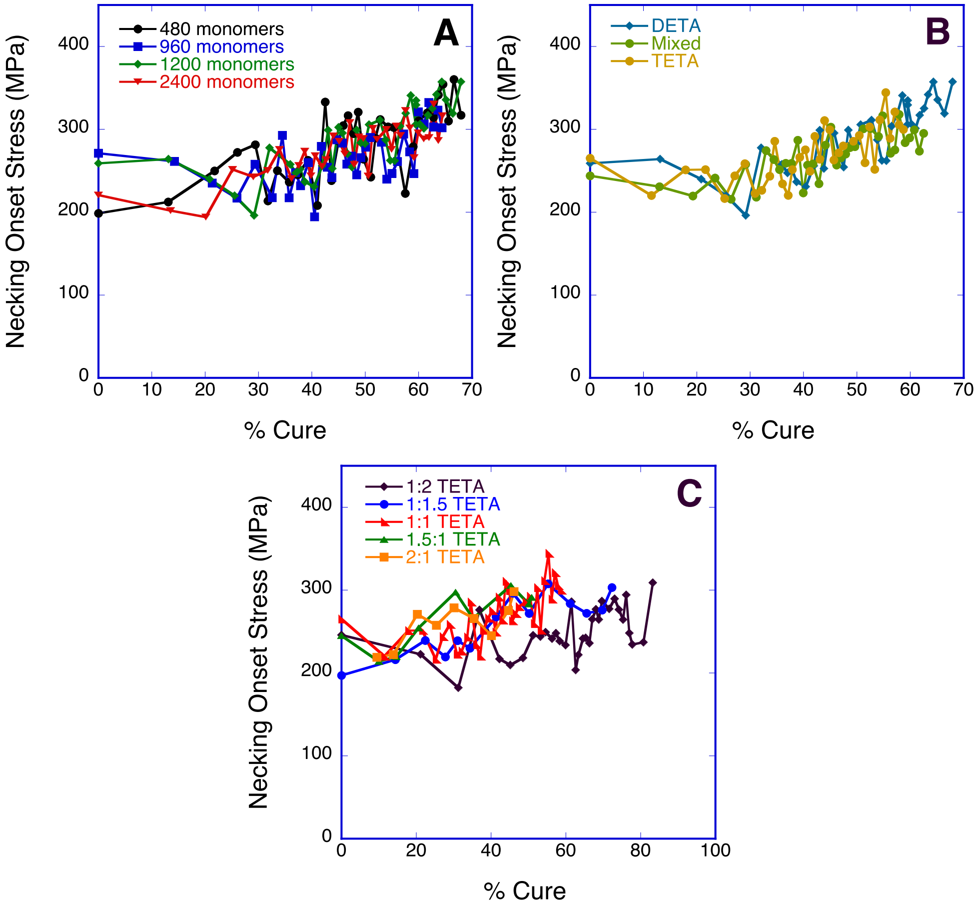

Figure 3.22. Tensile stress at the onset of necking as a function of cure for system of (a) varying size, (b) varying functionality and (c) stoichiometry

As the network develops, initially there is no significant change in the stress at the onset of necking, but after ~30% cure, there is a clear increase in the tensile strength of the network. As seen in previous metrics, a larger system size does not result in a change in properties, but instead improves the clarity of the results in Figure 3.22(a). The two different amines in Figure 3.22(b) continue to have very similar behavior. While there are only small differences between the different stoichiometries in Figure 3.22(c), the amine rich system seems to develop strength more slowly than the amine-poor system, in agreement with previous connectivity results.

The deformed structures at 20% and 100% strain for two different degrees of conversion in the 1200 monomer DETA system, are rendered in Figure 3.23.

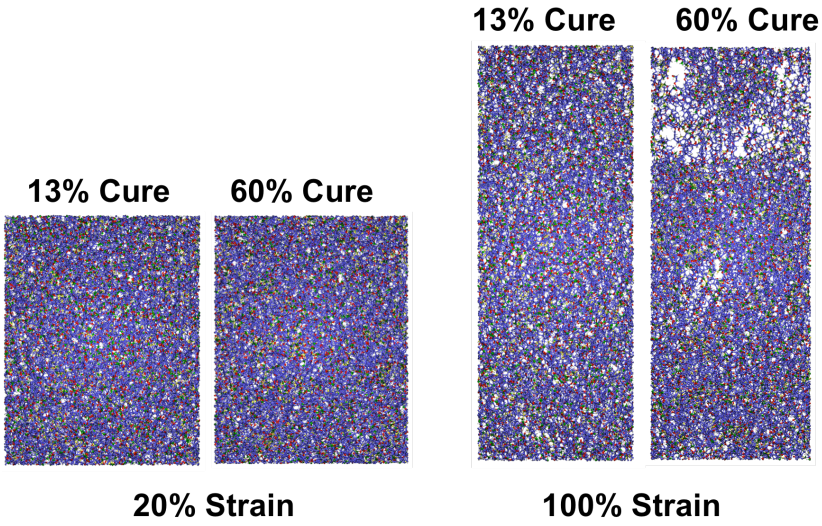

Figure 3.23. POVray rendering of the epoxy structure under ~20% strain and 100% strain for 13%cure and 60% cure and 50% strain

The minimally cured and 60% cured systems show no major differences at 20% strain. However, there is evidence of bond rupturing and void formation at 100% strain in the highly cured system, while the 13% cure system continues to deform in a fashion that preserves a relatively uniform density distribution. While at the nanoscale, we can see molecules bridging these interior voids, after fracture, they will rapidly reconfigure to join the fracture surface, resulting in the expected continuum level failure.

During plastic deformation, the nucleation and growth of voids is important to the prediction of fracture mechanics. To quantify the formation and growth of voids, the local mass density is calculated as a function of strain. To avoid errors due to hard cutoffs, a mass-conserving triquartic extrapolation is used for smoothing between cells.[97] Unlike a traditional Gaussian smoothing, the polynomial extrapolation is defined such that is goes to zero at the edge of the range of cells considered. The density is computed over five cells, assigning a fraction of each mass to the appropriate cell. Using a mass-density cutoff of 0.25 g/cm³ and a cell size of 2Å, the volume of voids in the system was then calculated, and presented as a function of strain in Figure 3.24.

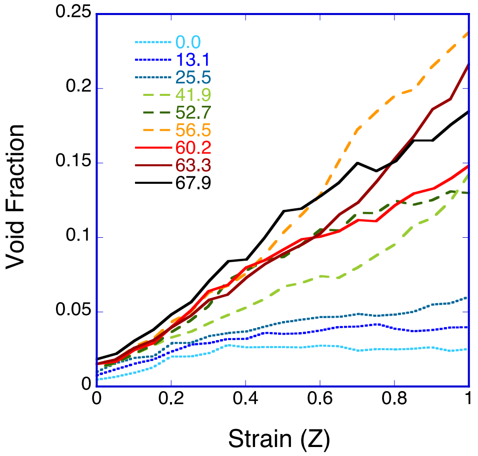

Figure 3.24. The total volume of voids in the system as a function of strain in the direction of the uniaxial tension. The legend indicates the degree of conversion.

The current cutoff and cell size shows 1-2% voids in the unstrained system. Use of smaller cells or cutoffs results in finding a high volume of voids in the fully dense system due to the point-mass definitions used in the calculation. In systems at relatively low degrees of cure, voids are fairly limited as the system behaves like a liquid. Above 40% cure, voids form more clearly, and grow consistently with strain. The liquid-like and gelled systems begin to diverge at 15-20% strain, which is where we see a maximum in the stress strain curve.

To verify that the mechanical properties are not significantly influenced by the further relaxation of the system, the stress-strain curves are compared between two systems at the same degree of conversion after 50ps and 200ps of relaxation, in Figure 3.25.

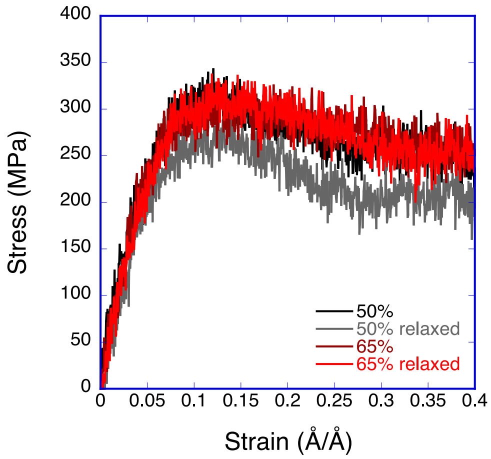

Figure 3.25. The stress-strain curve for systems at 50% and 65% cure, after 50ps and 500ps of relaxation

There are some differences in the stress-strain curves for systems that have undergone structural relaxation for 50 ps vs. 500 ps, particularly beyond 30% strain. However, the elastic regime seem largely unaffected. The Young's moduli of the two systems of 50% and 65% cure were shifted by -0.5 and 0.6 GPA, respectively. The system with a lower degree of cure is more susceptible to changes in the tensile strength at necking, which is somewhat expected as more substantial geometric changes are possible.

While the elastic properties of the system are only minimally changed by the growth of the network within the degrees of conversion achieved, the tensile strength of the epoxy is increased as a function of cure. The lack of any significant change in the repeat unit lengths as a function of strain indicates that below 60% cure, entanglement may remain the dominant deformation mechanism in a stoichiometrically balanced epoxy. Further relaxation of the structure within the reasonable confines of molecular dynamics simulations does not consistently affect mechanical properties. A clear transition between liquid-like and gelled network behavior could be seen by monitoring void formation.

The two functionalities of amine have nearly identical performance across all mechanical metrics. As expected from the structural results, while the amine-rich systems achieve a higher degree of cure, the development of stiffness and strength is somewhat delayed relative to other epoxide systems. While system size does not change the average elasticity or tensile strength as a function of cure, larger systems show smaller pressure fluctuations, which is critical to being able to confidentially interpret results.

3.4. Summary and Conclusions

We have examined the effect of system size, amine functionality, and stoichiometry on the structural and mechanical properties of a dynamically reacted bulk epoxy network. We are able to demonstrate a method for polymerization of a highly crosslinked network that allows us to monitor properties as a function of continuous cure of a network.

As expected, a volumetric shrinkage of ~1% is seen for all systems, accompanied by minor net tensile stresses. Network growth is tracked by calculating the mass-average molecular weight, dispersity, and cumulative distribution of molecular weights. A number of small molecules are formed and then grow, before joining to form an infinite network. While systems with a surplus of amine hardener reach higher degrees of epoxide conversion, the formation of an infinite network is delayed. Examination of the renderings shows that steric hindrance prevents complete conversion. The DGEBF monomers are more likely to fail to react with the network unless there is a substantial surplus of hardener. However, while the conversion of epoxide is higher in the amine-rich case, the formation of an infinite network and potential cross links is delayed compared to stoichiometrically balanced or amine-poor systems. System size and functionality has limited effects on any of the structural metrics considered.

Both elastic and plastic mechanical properties are studied during network growth. The elastic properties are only minimally changed by the growth of the network within the degrees of conversion achieved; however, the tensile strength of the epoxy was increased as a function of cure. The lack of local stresses or monomer deformation indicates that entanglement between molecules dominated the mechanics at the achieved degrees of cure. Further relaxation of the structure within the reasonable confines of molecular dynamics simulations did not consistently affect mechanical properties.

Amine functionality also has no clear effect on the mechanical properties, as anticipated from the structural results. Also, as expected from the characterization of network growth, amine-rich systems exhibit a delay in the development of strength. Increasing the system size does not alter the average mechanical properties as a function of cure, but showed more consistency, which is critical to being able to confidentially interpret results.

Clearly, continued iterations to push to higher degrees of conversion are needed, possibly including exploring higher cutoff values. Moreover, to better understand the effect of functionality, it is clear that DETA and TETA are too similar. The effects of initial mixing on network growth were not explicitly explored in this study, but would be off interest for future work.

3.5. References

1. Heinrich C, Aldridge M, Wineman A, Kieffer J, Waas AM (2011) Integrated computational materials science and engineering of textile polymer composites. Proceedings of the 52nd AIAA/ASME/ASCE/AHS/ASC structures, structural dynamics, and materials conference. Denver, Colorado, USA:

2. Heinrich C, Aldridge M, Wineman AS, Kieffer J, Waas AM et al. (2012) Generation of heat and stress during the cure of polymers used in fiber composites. International Journal of Engineering Science 53: 85-111.

3. Heinrich C, Aldridge M, Wineman AS, Kieffer J, Waas AM et al. (2012) The influence of the representative volume element (RVE) size on the homogenized response of cured fiber composites. Modelling and Simulation in Materials Science and Engineering 20: 075007.

4. Heinrich C, Aldridge M, Wineman AS, Kieffer J, Waas AM et al. (2013) The role of curing stresses in subsequent response, damage and failure of textile polymer composites. Journal of the Mechanics and Physics of Solids 61: 1241-1264.

5. Aldridge M, Shankar C, Zhen C, Sui L, Kieffer J et al. (2010) Combined experimental and simulation study of the cure kinetics of DCPD. Journal of composite materials 44: 2605-2618.

6. Aldridge MF, Waas AM, Kieffer J (2013) Elastic inhomogeneities in fiber towss of a textile polymer composite viainelastic light scattering. Materials Science and Technology

7. Aldridge M, Wineman A, Waas A, Kieffer J (2014) In Situ Analysis of the Relationship between Cure Kinetics and the Mechanical Modulus of an Epoxy Resin. Macromolecules

8. Aldridge MF (2014) In Situ Light Scattering Analysis of the Curing Behavior and the Mechanical Properties of Thermoset Polymers. deepbluelibumichedu

9. Aldridge M, Sebeck K, Waas A, Kieffer J (2014) Micro-Scale Polymer Matrix Elastic Properties in Composites using Inelastic Light Scattering Measurements and Molecular Dynamics Simulations. Bulletin of the American Physical …

10. Fan HB, Wong CKY, Yuen MMF (2008) A Multiscale Interfacial Delamination Model of Cu-SAM-Epoxy Systems. International Conference on Electronic Packaging Technology & High Density Packaging 2008:

11. Fan HB, Yuen MF (2007) Material properties of the cross-linked epoxy resin compound predicted by molecular dynamics simulation. Polymer 48: 2174-2178.

12. Ionita M (2012) Multiscale molecular modeling of SWCNTs/epoxy resin composites mechanical behaviour. Composites Part B: Engineering

13. Komarov PV, Yu-Tsung C, Shih-Ming C, Khalatur PG, Reineker P (2007) Highly cross-linked epoxy resins: an atomistic molecular dynamics simulation combined with a mapping/reverse mapping procedure. Macromolecules 40: 8104-8113.

14. Mijovic J, Zhang H (2004) Molecular Dynamics Simulation Study of Motions and Interactions of Water in a Polymer Network. J Phys Chem B 108: 2557-2563.

15. Salahshoor H, Rahbar N (2012) Nano-scale fracture toughness and behavior of graphene/epoxy interface. J Appl Phys 112(2): 023510.

16. Wu C, Xu W (2007) Atomistic molecular simulations of structure and dynamics of crosslinked epoxy resin. Polymer 48: 5802-5812.

17. Wu C, Xu W (2006) Atomistic molecular modelling of crosslinked epoxy resin. Polymer 47: 6004-6009.

18. Yarkovsky I, Evans E (2002) Computer simulation of structure and properties of crosslinked polymers: application to epoxy resin. Polymer 43: 963-969.

19. Yu S, Yang S, Cho M (2009) Multi-scale modeling of cross-linked epoxy nanocomposites. Polymer 50: 945-952.

20. Ziff RM, Hendriks EM, Ernst MH (1982) Critical properties for gelation: A kinetic approach. Physical Review Letters 49: 593.

21. Ziff RM, Finch SR, Adamchik VS (1997) Universality of finite-size corrections to the number of critical percolation clusters. Physical review letters 79: 3447.

22. Stockmayer WH (1943) Theory of Molecular Size Distribution and Gel Formation in Branched-Chain Polymers. J Chem Phys 11(2): 45.

23. Doi M (1995) Introduction to Polymer Physics. Oxford: Claredon Press.

24. Rodriguez F, Cohen C, Ober C, Archer LA (2003) Principles of Polymer Systems. Taylor & Francis.

25. Sindu BS, Sasmal S (2015) Evaluation of mechanical characteristics of nano modified epoxy based polymers using molecular dynamics. Computational Materials Science 96: 146-158.

26. Sirk TW, Karim M, Khare KS, Lenhart JL, Andzelm JW (2015) Bi-modal polymer networks: Composition-dependent trends in thermal, volumetric and structural properties from molecular dynamics simulation. Polymer 58: 199-208.

27. Zhang YY, Pei QX, He XQ, Mai Y-W (2015) A molecular dynamics simulation study on thermal conductivity of functionalized bilayer graphene sheet. Chemical Physics Letters 622: 104-108.

28. Khabaz F, Khare KS, Khare R (2014) Temperature dependence of creep compliance of highly cross-linked epoxy: A molecular simulation study. AIP Conference Proceedings 262-265.

29. Kumar A, Sundararaghavan V, Browning AR (2014) Study of temperature dependence of thermal conductivity in cross-linked epoxies using molecular dynamics simulations with long range interactions. Modelling Simul Mater Sci Eng 22: 025013.

30. Shokrieh MM, Esmkhani M, Shokrieh Z, Zhao Z (2014) Stiffness prediction of graphene nanoplatelet/epoxy nanocomposites by a combined molecular dynamics–micromechanics method. Computational Materials Science 92: 444-450.

31. Zhang Y-M, Li J-L, Wang J-P, Yang X-S, Shao W et al. (2014) Research on epoxy resin decomposition under microwave heating by using ReaxFF molecular dynamics simulations. RSC Adv 4: 17083-17090.

32. Sawa F, Imai T (2014) Molecular Dynamics Simulation for Epoxy-based Nanocomposites. ISEIM 327-329.

33. Li C, Coons E, Strachan A (2014) Material property prediction of thermoset polymers by molecular dynamics simulations. Acta Mech 225: 1187-1196.

34. Kim D-H, Kim H-S (2014) Investigation of hygroscopic and mechanical properties of nanoclay/epoxy system: Molecular dynamics simulations and experiments. Composites Science and Technology 101: 110-120.

35. Yang S, Qu J (2014) An invesitgation of the tensile deformation and failure of an epoxy/Cu interface using coarse-grained molecular dynamics simulations. Modelling and simulation in materials science and engineering 22: 065011.

36. Tam L-, Lau D (2014) A molecular dynamics investigation on the cross-linking and physical properties of epoxy-based materials. RSC Adv 4: 33074.

37. Hölck O, Bauer J, Braun T, Walter H, Wittler O et al. (2013) Transport of moisture at epoxy–SiO2 interfaces investigated by molecular modeling. Microelectronics Reliability 53: 1111-1116.

38. Shokuhfar A, Arab B (2013) The effect of cross linking density on the mechanical properties and structure of the epoxy polymers: molecular dynamics simulation. J Mol Model 19: 3719-3731.

39. Rahman R, Haque A (2013) Molecular modeling of crosslinked graphene–epoxy nanocomposites for characterization of elastic constants and interfacial properties. Composites Part B: Engineering 54: 353-364.

40. Li C, Jaramillo E, Strachan A (2013) Molecular dynamics simulations on cyclic deformation of an epoxy thermoset. Polymer 54: 881-890.

41. Sundararaghavan V, Kumar A (2013) Molecular dynamics simulations of compressive yielding in cross-linked epoxies in the context of Argon theory. International Journal of Plasticity 47: 111-125.

42. Sirk TW, Khare KS, Karim M, Lenhart JL, Andzelm JW et al. (2013) High strain rate mechanical properties of a cross-linked epoxy across the glass transition. Polymer 54: 7048-7057.

43. Okabe T, Takehara T, Inose K, Hirano N, Nishikawa M et al. (2013) Curing reaction of epoxy resin composed of mixed base resin and curing agent: Experiments and molecular simulation. Polymer 54: 4660-4668.

44. Mortazavi B, Benzerara O, Meyer H, Bardon J, Ahzi S (2013) Combined molecular dynamics-finite element multiscale modeling of thermal conduction in graphene epoxy nanocomposites. Carbon 60: 356-365.

45. Yang S, Gao F, Qu J (2013) A molecular dynamics study of tensile strength between a highly-crosslinked epoxy molding compound and a copper substrate. Polymer 54: 5064-5074.

46. Lin YC, Chen X (2005) Investigation of moisture diffusion in epoxy system: Experiments and molecular dynamics simulations. Chemical Physics Letters 412: 322-326.

47. Zhang FH, He XD, Dong LH, Yin YS (2009) Molecular Simulation of the Interfacial Properties of an Epoxy Composite Reinforced Using a Carbon Nanotube/Carbon Fiber Hybrid. Advanced Materials Research 79: 1289-1292.

48. Alperstein D, Dodiuk H, Kenig S (1998) Computer simulation of curing and toughening of epoxy systems. acta polymerica 49: 594-599.

49. Knaup JM, Kohler C, Frauenheim T, Blumenau AT, Amkreutz M et al. (2006) Computational studies on polymer adhesion at the surface of gamma-Al2O3. I. The adsorption of adhesive component molecules from the gas phase. J Phys Chem B 110: 20460-20468.

50. Lin PH, Kohale SC, Khare R (2011) Effect of nanoconfinement on kinetics of cross-linking reactions: a molecular simulation study. J Phys Chem B 115(43): 12348-12355.

51. Lin P-H, Khare R (2009) Molecular Simulation of Cross-Linked Epoxy and Epoxy-POSS Nanocomposite. Macromolecules 42: 4319-4327.

52. Knox CK, Andzelm JW, Lenhart JL, Browning AR, Christensen S (2009) High strain rate mechanical behavior of epoxy networks from molecular dynamics simulations. Army Science Conference Proceeding

53. Soni NJ, Lin P-H, Khare R (2012) Effect of cross-linker length on the thermal and volumetric properties of cross-linked epoxy networks: A molecular simulation study. Polymer 53: 1015-1019.

54. Frankland SJV, Gates TS (2007) Local Elastic Constants for Epoxy-nanotube Composites from Molecular Dynamics Simulation. Materials Research Society Fall Meeting

55. Li C, Browning AR, Christensen S, Strachan A (2012) Atomistic simulations on multilayer graphene reinforced epoxy composites. Composites Part A: Applied Science and Manufacturing 43(8): 1293-1300.

56. Li C, Medvedev GA, Lee E-W, Kim J, Caruthers JM et al. (2012) Molecular dynamics simulations and experimental studies of the thermomechanical response of an epoxy thermoset polymer. Polymer

57. Frankland SJV, Clancy TC (2008) Molecular Dynamics Simulation of Adhesion at Epoxy Interfaces. American Society fro Composites Proceedings

58. Nouri N, Ziaei-Rad S (2011) A Molecular Dynamics Investigation on Mechanical Properties of Cross-Linked Polymer Networks. Macromolecules 44: 5481-5489.

59. Liang Z, Gou JJ, Zhang C, Wang B, Kramer L (2004) Investigation of molecular interactions between (10, 10) single-walled nanotube and Epon 862 resin/DETDA curing agent molecules. Materials Science and Engineering A 365: 228-234.

60. Varshney V, Patnaik SS, Roy AK, Farmer BL (2008) A molecular dynamics study of epoxy-based networks: Cross-linking procedure and prediction of molecular and material properties. Macromolecules 41: 6837-6842.

61. Bandyopadhyay A, Valavala PK, Clancy TC (2011) Molecular Modeling of Crosslinked Epoxy Polymers: The Effect of Crosslink Density on Thermomechanical Properties.

62. Bandyopadhyay A, Odegard GM (2012) Molecular modeling of crosslink distribution in epoxy polymers. Modelling Simul Mater Sci Eng 20(4): 045018.

63. Bandyopadhyay A, Valavala PK, Odegard GM (2009) Atomistic Modelling of Crosslinked Epoxy Polymer. 17th International Conference on Composite Materials

64. Bandyopadhyay A, Odegard GM (2012) Molecular modeling of physical aging in epoxy polymers. J Appl Polym Sci n/a-n/a.

65. Gou J, Minaie B, Wang B, Liang Z, Zhang C (2004) Computational and experimental study of interfacial bonding of single-walled nanotube reinforced composites. Computational Materials Science 31: 225-236.

66. Li C, Strachan A (2010) Molecular Simulations of Cross-linking Process of Thermosetting Polymers.

67. Siva Prasad AVS, Gorver T, Basu S (2010) Coarse-grained molecular dynamics simulation of cross-linking of DGEBA epoxy resin and estimation of adhesive strength. International Journal of Engineering, Science and Technology 2: 17-30.

68. Stevens MJ (2001) Interfacial fracture between highly cross-linked polymer networks and a solid surface: effect of interfacial bond density. Macromolecules 34: 2710-2718.

69. Tan VBC, Deng M, Tay TE (2005) Coarse-Grained Molecular Modeling of Composite Interfaces. MSF 502: 39-44.

70. Zhu R, Pan E, Roy AK (2007) Molecular dynamics study of the stress-strain behavior of carbon-nanotube reinforced Epon 862 composites. Materials Science and Engineering: A 447: 51-57.

71. Wong CKY, Leung SYY, Poelma RH, Jansen KMB, Yuan CCA et al. (2012) Establishment of the coarse grained parameters for epoxy-copper interfacial separation. J Appl Phys 111(9): 094906.

72. Wong CKY, Leung SYY, Poelma RH, Jansen KMB, Yuan CCA et al. (2011) Molecular Dynamics study of the traction-displacement relations of epoxy-copper interfaces. Thermal, Mechanical and Multi-Physics Simulation and Experiments in Microelectronics and Microsystems (EuroSimE), 2011 12th International Conference on 1/5-5/5.

73. Cui H-, Li D-, Fan Q (2012) Adhesion of a novel flexible epoxy molding compound and its molecular dynamics simulation. International Journal of Adhesion and Adhesives 35: 50-54.

74. Yang S, Gao F, Qu J (2011) Modeling Separation Behavior of Epoxy/Cu Interface using Molecular Dynamics Simulation. Electronic Components and Technology Conference 1110-1114.

75. Jang C, Lacy TE, Gwaltney SR, Toghiani H, Pittman CU (2012) Relative Reactivity Volume Criterion for Cross-Linking: Application to Vinyl Ester Resin Molecular Dynamics Simulations. Macromolecules 45: 4876-4885.

76. Matthews FL, Rawlings RD (1999) Compositre materials: Engineering and science. Cambridge: Woodhead Publishing Limited.

77. MacKerell AD, Bashford D, Bellott MLDR, Dunbrack RL, Evanseck JD et al. (1998) All-atom empirical potential for molecular modeling and dynamics studies of proteins. The Journal of Physical Chemistry B 102: 3586-3616.

78. Sun H (1998) COMPASS: An ab initio force-field optimized for condensed-phase applications overview with details on alkane and benzene compounds. The Journal of Physical Chemistry B 102: 7338-7364.

79. Sun H, Ren P, Fried JR (1998) The COMPASS force field: parameterization and validation for phosphazenes. Computational and Theoretical Polymer Science 8: 229-246.

80. Yang J, Ren Y, Tian A, Sun H (2000) COMPASS force field for 14 inorganic molecules, He, Ne, Ar, Kr, Xe, H2, O2, N2, NO, CO, CO2, NO2, CS2, and SO2, in liquid phases. The Journal of Physical Chemistry B 104: 4951-4957.

81. Van Duin ACT, Dasgupta S, Lorant F, Goddard III WA (2001) ReaxFF: a reactive force field for hydrocarbons. The Journal of Physical Chemistry A 105: 9396-9409.

82. Jorgensen WL, Tirado-Rives J (1988) The OPLS potential functions for proteins. Energy minimizations for crystals of cyclic peptides and crambin. Journal of the American Chemical Society 110: 1657-1666.

83. Jorgensen WL, Maxwell DS, Tirado-Rives J (1996) Development and testing of the OPLS all-atom force field on conformational energetics and properties of organic liquids. Journal of the American Chemical Society 118: 11225-11236.

84. Jorgensen WL, McDonald NA (1998) Development of an all-atom force field for heterocycles. Properties of liquid pyridine and diazenes. Journal of Molecular Structure: THEOCHEM 424: 145-155.

85. Kahn K, Bruice TC (2002) Parameterization of OPLS-AA force field for the conformational analysis of macrocyclic polyketides. J Comput Chem 23: 977-996.

86. Kaminski G, Jorgensen WL (1996) Performance of the AMBER94, MMFF94, and OPLS-AA force fields for modeling organic liquids. The Journal of Physical Chemistry 100: 18010-18013.

87. Mayo SL, Olafson BD, Goddard WA (1990) DREIDING: A generic force field for molecular simulations. Journal of Physical Chemistry 94: 8897-8909.

88. McDonald NA, Jorgensen WL (1998) Development of an all-atom force field for heterocycles. Properties of liquid pyrrole, furan, diazoles, and oxazoles. The Journal of Physical Chemistry B 102: 8049-8059.

89. Rappé AK, Casewit CJ, Colwell KS, Goddard Iii WA, Skiff WM (1992) UFF, a full periodic table force field for molecular mechanics and molecular dynamics simulations. Journal of the American Chemical Society 114: 10024-10035.

90. Rizzo RC, Jorgensen WL (1999) OPLS all-atom model for amines: resolution of the amine hydration problem. Journal of the American Chemical Society 121: 4827-4836.

91. Bolton E, Wang Y, Thiessen PA, Brynat S (2008) PubChem: Integrated Platform of Small Molecules and Biological Activities. Annual Reports in Computational Chemistry 4: Ch. 12.

92. Frisch MJ, Trucks GW, Schlegel HB, Scuseria GE, Robb MA et al. (2009) Gaussian 09.

93. Plimpton S (1995) Fast parallel algorithms for short-range molecular dynamics. Journal of Computational Physics 117: 1-19.

94. Rohr DF, Klein MT (1990) Modeling Diffusion and Reaction in Cross-Linking Epoxy-Amine Cure Kinetics: A Dynamic Percolation Approach. Ind Eng Chm Res 29: 1210-1218.

95. Theodorou DN, Suter UW (1986) Atomistic modeling of mechanical properties of polymeric glasses. Macromolecules 19: 139-154.

96. Zimmerman JA, Webb III EB, Hoyt JJ, Jones RE, Klein PA et al. (2004) Calculation of stress in atomistic simulation. Modelling and simulation in materials science and engineering 12: S319.

97. Deserno M, Holm C (1998) How to mesh up Ewald sums. I. A theoretical and numerical comparison of various particle mesh routines. J Chem Phys 109: 7678.

Chapter 4. Interfaces between entangled polymers and ordered substrates

4.0. Synopsis

Planar interfaces between linear alkanes and FCC metal surfaces were constructed as a model system for studying interfaces between dissimilar materials. Several competing interactions at the interface are expected to contribute to the structural changes observed within the alkane region. To deconvolute these different interactions, a series of molecular dynamics simulations were performed with unconfined alkane on a metal substrate, varying the length of the alkane chain, the metal of the substrate, and for one combination, the interaction strength between the substrate and the polymer. Mechanical properties were determined as a function of film thickness for nano-confined alkanes with a constant chain length on a copper substrate.

Although this is intended as a simple model system, we were able to observe a clear nanoscale interphase, with several interesting results. First, a power-law relationship is seen between the interaction strength between the alkane and the substrate, and the density maximum, as well as the distance between the substrate surface and the density maximum. Secondly, the radial distribution function of layers within the alkane show a shortening of the C-C pair distance near the interface, returning to the expected equilibrium value with increasing distance from the interface. Lastly, within the nanoscale interfacial region the Young's modulus and the density are strongly correlated, with localized deformation occurring in the low-density regions.

4.1. Introduction

Composite materials are becoming increasingly important to meeting evolving performance requirements in a variety of industries, including automotive, aerospace and defense. Polymer matrix composites in particular have a high strength:weight ratio, as well as good toughness, which make them a strong alternative for metal components in many situations. However, designing composite components is more challenging than traditional metal parts, due to the more complex processing options, and the directional nature of mechanical properties. These inhomogeneties occur on several length scales, which further complicates predictions of failure. These length scales of interest extend from structural components to the micron scale fibers, down to the interfacial variations at the nanoscale. Finite element analysis is typically used to model the bahvior at continuum length scales, but the atomistic structures at the nanoscale have more discrete behavior. First principles calculations, such as density functional theory, typically can only model fewer than a thousand atoms, making it typically subnanoscale. However, molecular dynamics simulations are particularly well-suited to examination of structures at this smallest length scale, typically studying systems in the tens of nanometers.

While common polymer matrix composites are based on cross-linked materials, we want to examine a simpler model system. Linear alkane chains are among the simplest polymers, with only single bonds between carbon and hydrogen. There is some prior work on similar simple systems, though simulations of simple hydrocarbon-metal interfaces have primarily focused on single chemisorbed molecules or monolayers, with an emphasis on thiols.[1-8] However, single molecule or monolayer conformations do not reflect the more complex structure of the interfacial region, or the extent of the effect of the substrate.

Thicker layers and coatings have been studied for primarily chemisorbed species, where reactions occur between the polymer and the substrate.[9,10] Prior studies of alkanes physiosorbed on a crystalline substrate have shown interesting density variations perpendicular to the substrate, but have used fixed or flat walls.[11-13] Most studies have been done with either significant coarse-graining, small-molecule systems or perfectly smooth walls. Substrate-induced structural features, such as molecular layering near the interface have also been reported in other polymer phases.[14-16] Scheidler and co-authors treated such layering effects near a smooth wall as a problem, and added a term to energetically favor a constant density profile.

Experimental efforts to characterize the interphase in thin polymer films are based on several techniques. As in the simulation literature, monolayers are frequently studied as a first approximation and there is an extensive body of work studying monolayer films, particularly in the context of self-assembly.[17] However, prior work has shown that the interphase can extend well beyond this first deposition layer, though there is significant debate over the actual extent.[18-31] In the study of thin films, grazing incidence small angle x-ray scattering (GISAXS) can be a powerful tool, but the complexity of the analytical solutions have somewhat limited the application of this technique.[32-34] More commonly, changes in the glass transition as a function of film thickness or probe depth have been used as a proxy structural measurement.[35-42] The dependence of T_g on the film thickness was first demonstrated in polystyrene, but has since been observed in a variety of other polymer systems.

Mechanical models of the interphase have primarily been developed using macro- to microscale experimental data.[11,18-22,24-31,43,44] This was proposed as a mechanism to explain the deviations in elastic behavior in the transverse direction from the predictions of the rule of mixtures, more formally called the Reuss and Voight bounds.[21-23,26] Experimental characterization of these local mechanical properties is as challenging or more so than the structural characterization of the same regions.[45,46] A number of models to describe the continuum level mechanics have been developed over recent decades, typically focusing on fracture behavior, but also considering the elastic properties.[18-21,23,25-31] The interphase region is typically considered inhomogenous, with mechanical properties varying as a function of the thickness, assuming constant isotropic behavior in the bulk matrix and reinforcement materials. At the nanoscale, the interphase is a more discrete phenomenon. Models have largely been driven by surface interactions and chain immobilization, particularly in entanglement-dominated mechanics[22].

We first examine the structural variations associated with metal substrate, alkane chain length, and interfacial interaction strength for an unconfined film. The mechanical properties were explored as function of layer thickness, focusing on a single chain length and substrate for a nano-confined laminate system.

4.2. Computational Methods

All simulations were performed with the LAMMPS molecular dynamics code.[47] Initial alkane chain geometries were generated with the Polymer Modeler tool from nanohub.org.[48] Force field parameters for the alkane chains are based on the OPLS-AA force field.[49] Metal-metal interactions are modeled with the Embedded Atom Method (EAM) potentials incorporated in the LAMMPS distribution.[50,51] Alkane-metal interaction parameters are determined by geometric mixing rules defined in Equation 4.1, using LJ 12-6 parameters specifically optimized for FCC metal surfaces. [52]

Table 4.1 Lennard Jones 12-6 Parameters for All Species

Species	**ε (kcal/mol)**	**σ (Å)**	**Lattice Parameter (Å)**
Ni	5.65	2.532	3.52
Cu	4.72	2.616	3.61
Ag	4.56	2.955	4.08
Pb	2.93	3.565	4.95
C_{alkane}	0.065975	3.50	--
H_{alkane}	0.030007	2.50	--

$$\varepsilon_{ij} = \sqrt{\varepsilon_i \varepsilon_j}$$
$$\sigma_{ij} = \sqrt{\sigma_i \sigma_j}$$

Eq. 4.1. Geometric mixing rules for Lennard-Jones potentials

Unconfined alkane-metal interfaces were generated with 800 linear alkane chains with lengths of n=10, 20 and 40 with each of the four metals listed in Table 3.1. A target thickness of 60Å was assigned for n=10 and a thickness of 80Å for n=20 and 40. Periodic boundary conditions were removed from the z direction of the polymer structures and energetically minimized. The x and y parameters are slowly deformed to match a multiple of the substrate lattice parameter. The metal slab was then inserted in the xy plane, with a minimum thickness of 6 unit cells.

External opposing forces of $2x10^{-5}$ eV/Å were applied in the z direction to force the layers in to contact over 10ps. After effective physisorbtion, this force was removed and structures were further equilibrated for 15ps under constant volume-temperature conditions at 600K. The structure was then cooled to 300K over 25ps, equilibrated under NVT conditions for a further 25ps and finally relaxed under NVE conditions for 25ps.

In addition to the previous 15 configurations, 4 additional systems were constructed, varying the interaction strength between a silver surface and n-alkane with n=20 throughout the simulation. Values of σ were held constant, while ε values of 1/8, ¼, ½ and 2 times the geometric mixing value were sampled. Attempts at 4 times the geometric mixing strength did not run to completion.

Nano-confined structures were generated by randomly orienting linear alkane chains at very low density. The number of alkane chains in the system was varied, with a constant chain length of n=20. A copper substrate was chosen. All simulations used similar interfacial areas of 86.6Å by 86.6Å (7504Å^2). This fully periodic structure is compressed perpendicular to the metal surface, at elevated temperatures for 60ps under NPT. The free vacuum generated by the initial condensation was then eliminated by re-fitting the simulation box to the actual atomic positions. The box was then deformed under constant pressure to the final target thickness over 10 ps, and equilibrated under NVE conditions for 20 ps. The thicknesses of each are shown in Table 4.2. The structure was further relaxed with 10 MPa of pressure applied in the z direction for 500 ps. This final structure was then used for tensile analysis. For comparison, bulk systems of 800 chains with fully periodic boundary conditions were also prepared, using hydrostatic pressure instead of directional compressions.

Table 4.2. Thickness of the nanoconfined alkane layers based on the number of chains

Number of Chains	*Alkane Thickness*
400	24.2
600	36.4
800	49.3
1000	62.0

A number of methods have been considered for quantifying the structural variations observed with the introduction of an interface. Most obviously, the density profile perpendicular to the substrate is examined. Further quantities examined include the bulk pair correlation function, the 2-D pair correlational function taken in slices parallel to the substrate, end-to-end chain vectors, and intermolecular spacing. Some traditional metrics, such as radius of gyration, are also included for comparison.

4.3. Results and Discussion

The presence of an interface has an immediate and obvious influence on the structure of the alkane layer. This can be seen in Figure 4.1, where distinct can be identified based on the oscillations in the density profiles. Peak densities decrease with increasing distance from the alkane-metal interface and eventually reach bulk levels. For comparison, the density profile of a bulk alkane system is shown in Fig. 4.1b.

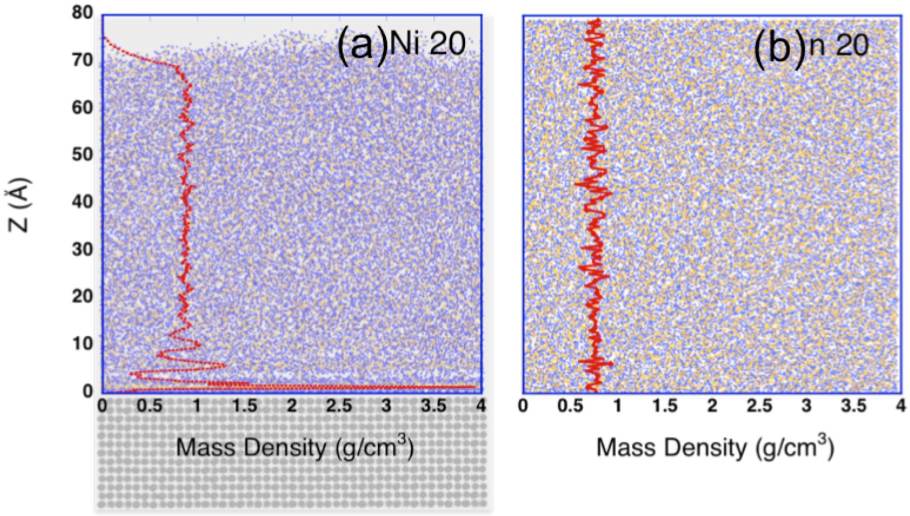

Figure 4.1. Density profiles within the alkane are superimposed on VMD rendered structures for a chain length *n=20*, for (a) an unconfined alkane layer on a Ni substrate and (b) a bulk alkane system.

The alkane layer immediately adjacent to the nickel substrate has a density nearly 5 times the bulk density of the alkane layer. In both cases, local variations can be seen, but in the presence of a metal substrate, distinct layers appear, continuing to over 1 nm from the substrate surface before the local density approaches the average of the bulk system. Qualitatively, the low-density regions can be seen in the rendering of the structure. A detailed examination of the density profile is presented in Figure 4.2, comparing the different substrates, chains lengths, and metal-alkane adhesive interaction strengths.

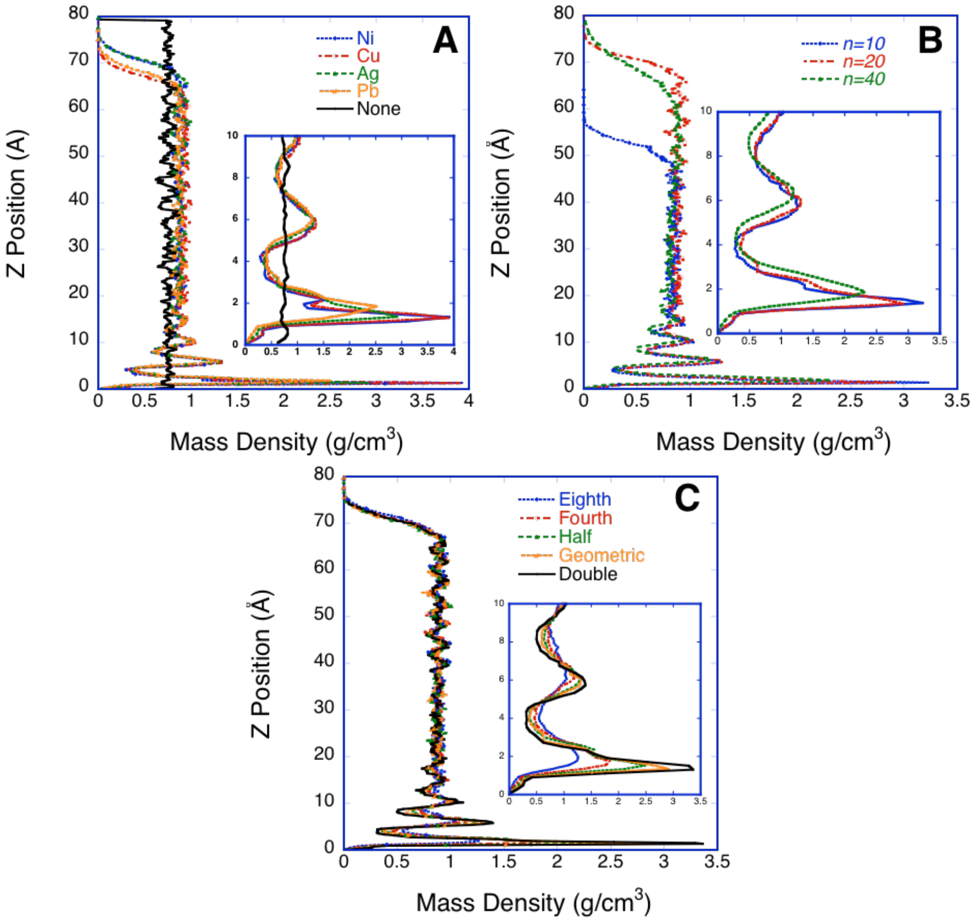

Figure 4.2. Mass density profiles for (a) the four metal substrates and chain length *n*=20, (b) three chains lengths on the Ag substrate and (c) variable interaction strength between *n*=20 chains and Ag. Insets provide a magnified view of the first 10Å

Figure 4.2(a) shows the density profiles for each of the four FCC metal substrates, as well as a periodic *n*=20 system included as a reference. The four metal substrates show comparable overall behavior, but a closer examination of the first two dense layers belies the differences. The lattice parameters of Ni and Cu are very similar (3.52Å and 3.61Å, respectively), but the Ni substrate has a larger value for interaction strength, and hence a stronger interaction between the alkane and the substrate. Conversely, Cu and Ag have different lattice parameters (3.61Å and 4.08Å), but similar interaction strengths. The distance between the substrate and the first density peak is nearly identical for Ni and Cu, indicating a dependence on lattice parameter over small differences in interaction strength. Lead, which has the largest lattice parameter and weakest interaction strength, has the lowest maximum density, as well as the greatest distance between the substrate and the maximum density. The shoulder visible for the other substrates is also not seen in the broader lead peak.

In Figure 4.2(b), the three alkane chain lengths are shown. There is little difference in the profile of the two shortest chain lengths, *n*=10 and *n*=20. However, the longest chain length examined, *n*=40, begins to show a decrease in the maximum density, and an increase of the distances of the density maxima from the interface. It is expected that this would continue at higher chain lengths. Figure 2(c) shows more extreme variations in the adhesive interaction strength, altering the alkane-metal adhesive interaction strength by a factor of two between systems. The maximum density shows a dramatic decrease with decreasing interaction strength, as well as an increasing distance from the substrate. The shoulder also gradually disappears with decreasing interaction strength, indicating that is an adhesion affect, rather than originating with substrate geometry.

In the nanoconfined simulation, the same layering behavior is seen at both interfaces. The extent of the structural interphase is similar in all cases, seen in Figure 4.3.

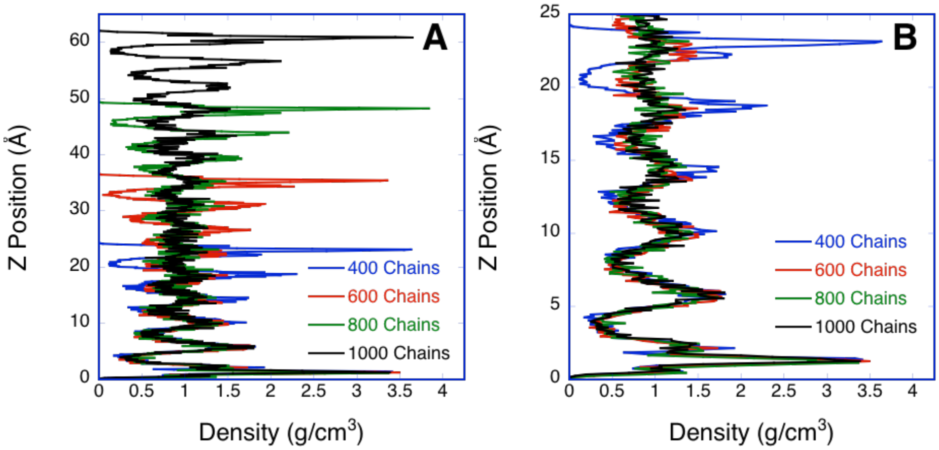

Figure 4.3. Density profiles for various thickness of alkane showing (a) the complete density profiles and (b) the first 25Å

All of the nanoconfined structures show the expected symmetry in Figure 4.3(a), but more importantly, show very similar density behavior in the first 8Å in Figure 4.3(b), which corresponds to approximately two layers. The central region of the thickest system, with 1000 alkane chains exhibits density fluctuations on the order of those observed for the bulk alkane system. However, in the case of the thinnest slabs, the density profile fails to approach bulk behavior in the symmetrically confined systems. This is most obvious when looking at the 400 chain case, shown in blue, where we see six distinct density layers through the alkane thickness. The next larger system is ~8Å thicker, and also still shows oscillations in the density profile throughout its thickness. The remaining systems all seem to reach bulk density behavior at least briefly in the center of the layer.

The maximum density is quantified for the various substrate and interaction strength configurations, and summarized in Figure 4.4.

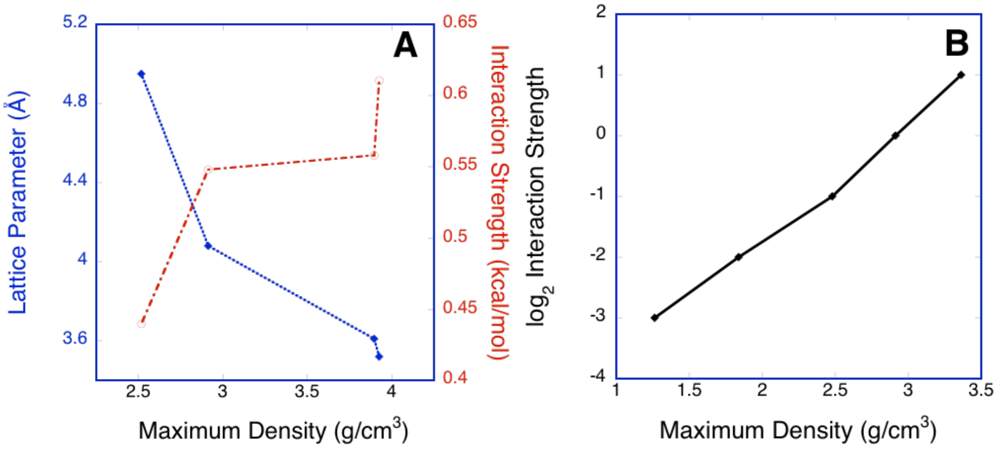

Figure 4.4. The dependence of the maximum slice density on (a) lattice parameter (blue) and interaction strength (red) for *n*=20 on the four FCC metals and (b) log$_2$ interaction strength scaling.

The lattice parameter, shown in Figure 4.4(a), demonstrates a strong inverse trend with maximum density, while no clear trend is observed based on the differences in the adhesive interaction strength using geometric mixing rules. Over a larger range of adhesive interaction strength, covered in a parametric study, a power law behavior is observed, as seen in Figure 4.4(b). However, even doubling the interaction strength between silver and the alkane did not result in as high of a maximum density as seen for the nickel substrate. This indicates a geometric origin, as the interaction strength between Ni and C from geometric mixing is 0.19kcal/mol, and the interaction strength between Ag and C is 0.18 kcal/mol.

To look more closely at the nature of these alkane structures, we first examine the pair correlation function for those atoms in center of the alkane layer, such that the cutoff of the distribution remains within the polymer phase. This is done to avoid normalization errors due to finite edge effects. Only carbon-carbon pairs are included, allowing us to compare only the structure of the alkane layers without interference from the innate ordering of the metal. The pair correlation functions, presented in Figure 4.5, shows a distinct difference between the free surface systems and a bulk alkane system.

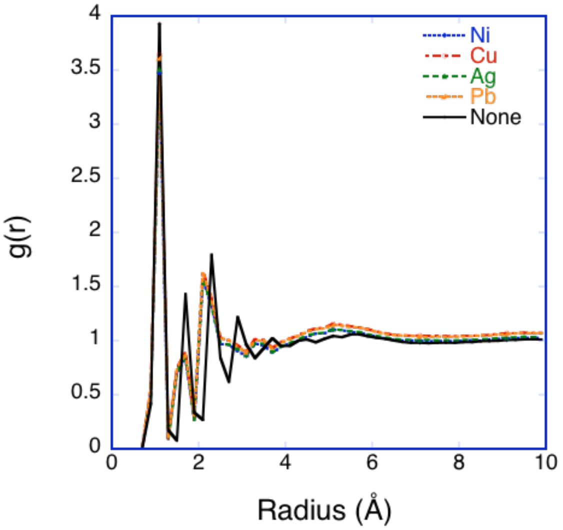

Figure 4.5. Pair correlation function for alkane elements in the center of the layer on the four substrates compared to the same method applied to a bulk sample (black).

The pair correlation function for bulk alkane is shown in black, whereas those for the various metal substrates represented using different colors. However, there is no clear differentiation between the different substrates. Relative to the bulk alkane system, peaks associated with the second- and, even more so, the third-nearest neighbor C-C pair distance in the layered structures are shifted, indicating a definite change in the chain conformations. There is also some broadening of this peak, which hints at broader distribution of local structures. This likely relates to the higher density of the alkanes in the presence of a substrate.

The layers were examined more closely by taking essentially a two-dimensional pair correlation function of finite slices at different distances from the interface. This by projecting The positions of the atoms within a slice are projected onto a plane parallel to the interface, and the pair correlation function is calculated using the distances between the projected positions in two dimensions. The locations of these slices relative to the interface and their respective distribution functions are shown in Figure 4.6 for an unconfined alkane layer with a chain length of n =20 on a silver substrate.

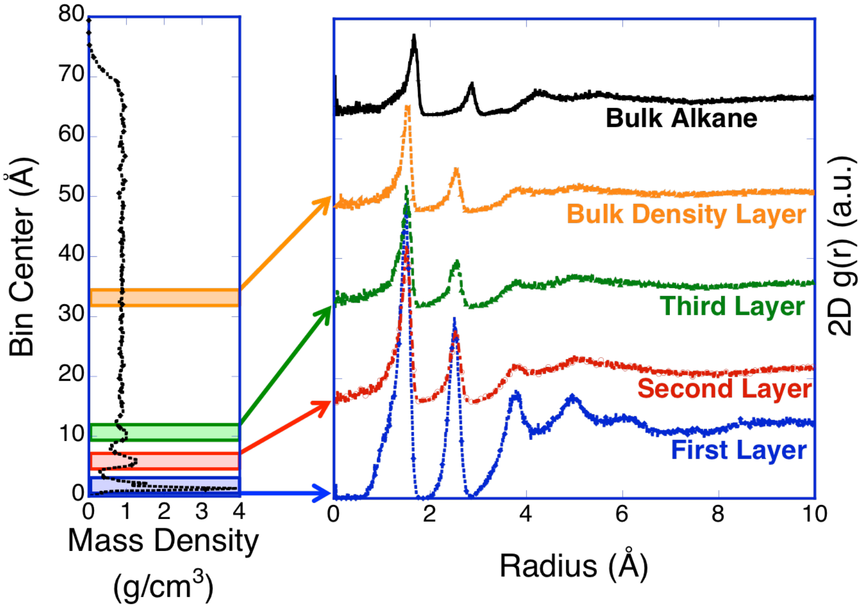

Figure 4.6. Slices of 2Å are taken parallel to the substrate surface and projected onto a plane. The 2D pair correlation function of the C-C pairs are shown for the first three layers of n=20 on a silver substrate, an equivalently sized slice in the "bulk" region and periodic n=20 as compared to the respective density profiles.

Compared to the three-dimensional pair correlation function focused on the center of the film (Figure 4.5), in two dimensions near the interface, the C-C pair distance appears to be shortened relative to the bulk. This, however, is likely only an artifact due to the projection scheme, which eliminates some of the distance between atoms if they are located at different vertical positions. This slant is also manifest in asymmetric tail of the peaks towards short distances. For the second and third carbon neighbor shells describing alkane near the substrate the shift is more pronounced, and the fact that is physically meaningful is corroborated by the three-dimensional pair correlation functions. In addition, the structure of the interfacial layers shows a higher degree of order. In the first layer adjacent to the substrate, peaks are clearly discernable as far out as 5.5A, compared to 3Å in bulk alkane. As distance from the substrate increases, the pair-correlation gradually approaches to the bulk alkane behavior.

In an effort to better understand the nature of these dense layers, we visually examine the polymer layer nearest the interface. Figure 4.7 shows the profile views, indicating where the cross-sections are taken, (a and c) and renderings of the cross-sections for a n=20 chain on silver(b), and a bulk n=20 system (d).

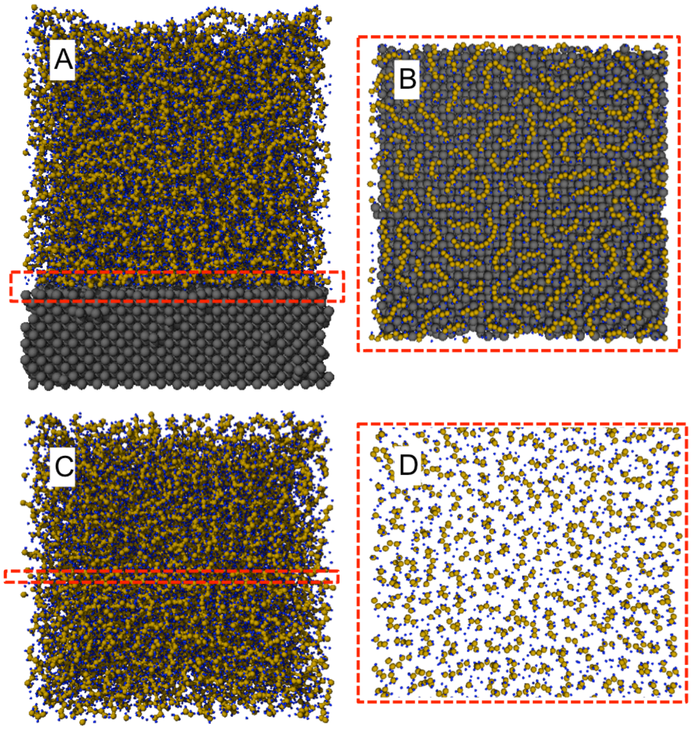

Figure 4.7. Rendering of the layering behavior showing (a) profile view of an *n*=20 chain length alkane on silver, (b) cross section view rendering only the atoms indicated in the profile, (c) profile view of a bulk periodic *n*=20 alkane and (d) corresponding cross-sectional view for bulk periodic alkane.

The alkane repeat units in contact with the surface, as seen in Figure 4.7(b), tend to be fairly closely packed, which in turn instills a higher degree of order than an entirely random would exhibit, and which is in agreement with the additional peaks seen in the pair correlation function at the surface. Also a significant portion of each chain is contained within the layer, indicating the chain tends to lie on the surface, a consequence of the attractive forces and the loss of orientational degrees of freedom due to the one-sided confinement. In contrast, a slice of the same thickness taken from a bulk alkane system, seen in Figure 4.7(d), contains randomly oriented small segments with no obvious domain formation.

To characterize the spacing between chains physisorbed onto the surface observed in Figure 4.7(b), the median value of the nearest neighbor carbon-carbon distance is determined, considering only for those pairs that belong to different chains. These results are presented in Figure 4.8.

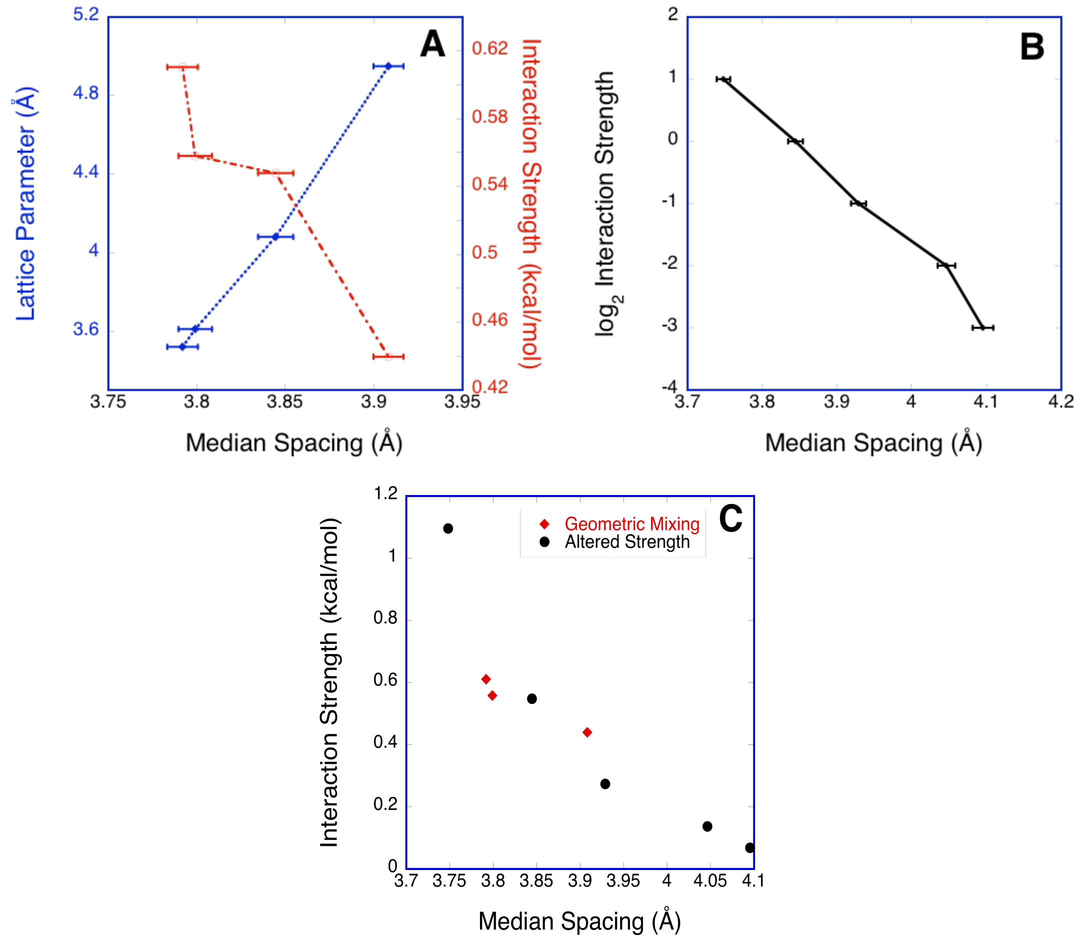

Figure 4.8. Median spacing between chain backbones for (a) various substrates and (b) varying interaction strength with (c) superimposing the substrate and interaction strength results.

As shown Figure 4.8(a) in blue, the median chain spacing has a close to linear dependence on the lattice parameter, but is not particularly sensitive to small changes in interaction strength, shown in red. This is particularly evident comparing the Ag and Cu substrate, which have similar interaction strengths, but different lattice parameters, resulting in the jump seen in the interaction strength trend. This is inverse from the trends previously seen for the maximum density, which is intuitively logical. The error bars indicate one standard deviation from the average value.

In Figure 4.8(b), the spacing between carbon chains follows an inverse power law dependence with the interaction strength, again, reciprocal to the previously observed trend in the maximum density. While the smallest chain spacing is associated with the nickel substrate (lattice parameter of 3.52Å), changing the interaction strength between silver and the alkane results in a much wider range of spacings, a range of 0.4Å instead of 0.11Å. This shows that the interaction strength for an arbitrarily chosen substrate lattice spacing can supersede the order created due to the lattice spacing at realistically chosen interaction strengths. This can be further seen in Figure 4.8(c), where both sets of data are presented as a function of the interaction strength.

Again examining the renderings of the first layer in Figure 4.7(b), it is clear that a significant portion of the alkane chain is in contact with the substrate, but not always the entire chain. To quantify this, the number of backbone carbon atoms within the first layer (as determined by the density profile) are counted for each partially physisorbed chain. For comparison, in bulk alkane, slices of a thickness equivalent to that of the directly absorbed alkane layer are taken and the number of repeat units contained in that layer are counted and averaged. Results for the number of alkane chains with the number of units given by the abscissa in contact for variable substrates, polymer chain lengths and interaction strength are presented in Figure 4.9.

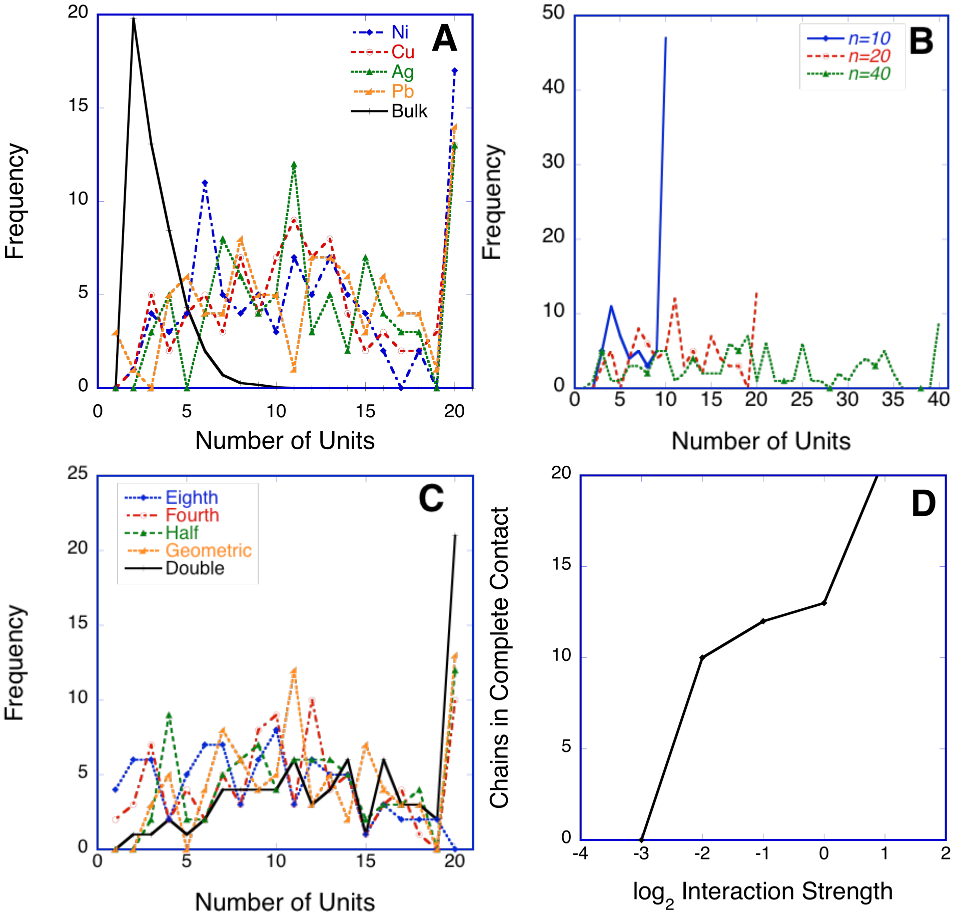

Figure 4.9. Number of polymer units in contact with the substrate for (a) various lattices and chain length *n=20*, (b) various chain lengths on Ag substrate, (c) variable interaction strength for chain length *n=20* and Ag substrate, and (d) summary of interaction strength dependency on the number of congruent chains

Comparing first the bulk system and the four metal substrates in the Figure 4.9(a), while there is a difference between systems with and without a substrate, differences between substrate types are at best within the range of the statistical variance. In bulk alkane, the histogram of polymer units belonging to a given chain within a slice of contact layer thickness shows a skewed distribution, with only a few backbone atoms lying within a slice. The *n=20* systems deposited on a metal substrate show a distinctly bimodal trend: chains either are fully adsorbed, or follow a distribution with a maximum around 10 mer units. For any substrate type, the number of chains that are completely in contact with the surface constitute the largest population. However, the population of chains with 19 units in contact is almost nonexistent, indicating that once chains have a significant fraction in contact with the surface, chains are drawn to the surface to be in complete contact. This behavior is more pronounced for shorter chain lengths, as shown in Figure 4.9(b). Shorter chains are the most likely to be fully adsorbed, with the distribution flattening out as chain length increases. In all the chain lengths studied, it is most likely that the chain will be fully in contact, rather than only partially within the contact layer. However, it is expected that this trend would not be the case much beyond n=40, as full chains in contact are only slightly more probable in the n=40 chain length case. Looking at the number of polymer units in contact as a function of interaction strength, plotted in Figure 4.9(c), we see the same bimodal distribution as observed for the different substrates. Examining the trend between interaction strength and number of chains in complete contact in Figure 4.9(d), we observe a linear-$\log_2$ trend, as seen previously in the maximum density behavior. No obvious trend in distribution or maximum number of chains in contact is observed as a function of lattice parameter.

The vector from one end of the carbon backbone to the other is determined to quantify the orientation of individual alkane chains. The angle between the surface plane and this vector for each chain is calculated, and compared. As the chains have no particular head or tail, the absolute value of this angle was used, resulting in a range of angles from 0 and 90 degrees. For the random vectors and bulk alkane systems, the angle to the *xy* plane normal is taken, though there is no substrate. The results of these calculations are presented in Figure 4.10.

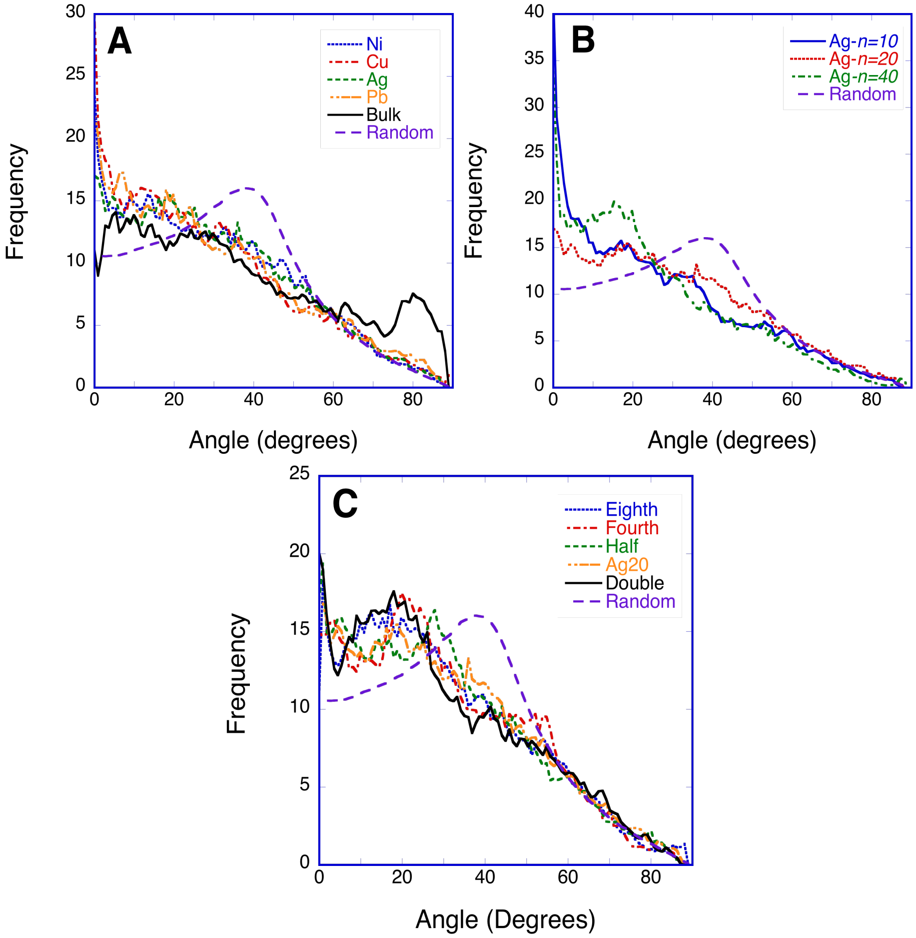

Figure 4.10. The distribution of angles between the end-to-end vector and the substrate compared to a system of 800 random vectors for (a) different substrate lattices, (b) different chain lengths for periodic and silver substrate systems and (c)variable interaction strengths of *n*=20 on a silver substrate.

Figure 4.10(a) shows that most probable chain orientation is altered by the presence of a substrate. Compared to the random vectors, there is an increased number of chains between 0-20° to the surface, but the frequency is not strongly affected by lattice type. These low-angle orientations are largely accounted for by the chains in the near-surface layers. Interestingly, the bulk alkanes are also non-randomly oriented relative to the *xy* plane, showing significant deviation from the randomly generated vector set. Notably, chains are more likely to be parallel or perpendicular to one another, with fewer chains at angles between 20-60°, which would be the expected most probable angle from the random vectors.

Figure 4.10(b) shows the effect of chain length for both the bulk systems and the silver substrate systems. Shorter chain lengths are the most likely to lie parallel to the surface. Longer chain lengths show a secondary peak at 15-20°, which correlates with chains bridging multiple layers. This can be qualitatively seen in Figure 4.11. The effect of changes in substrate-alkane interaction strength are shown in Figure 4.10(c), where increasing the strength primarily affects the number of parallel chains, which again, are largely accounted for in the contact layer.

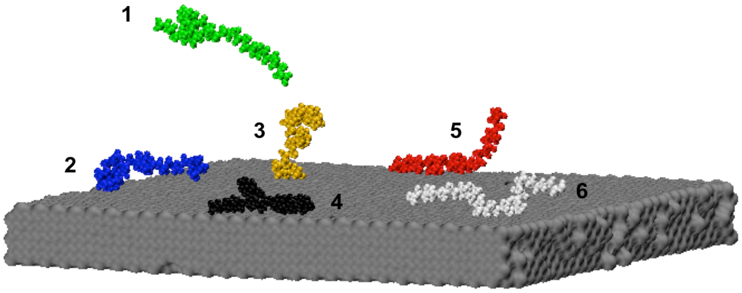

Figure 4.11. A variety of chain conformations seen in *n*=40 alkane on a silver substrate showing different layer-bridging behaviors and bulk chain conformations.

In Figure 4.11, chain 1 is typical of the region of the alkane with bulk density. Accounting for most of the barely physisorbed and high-angle chains, one which is mostly perpendicular to the substrate is shown as chain 3. Chains 2, 4, and 6 are all examples of different conformations with end-to-end vectors parallel or near parallel to the surface, with different fractions of the backbone in contact with the substrate surface. Chain 5 exhibits a hybrid behavior, half physisorbed and half perpendicular to the substrate.

Some models of the mechanics of the nanoscale interphase have attributed its stiffening to immobility and a difference in the radius of gyration at the interface.[22] The radius of gyration is determined for all alkane chains in the nanoconfined systems, and averages are taken for slices in the *xy*-plane. These averages are superimposed on the raw data for the first 30Å above the substrate, presented in Figure 4.12.

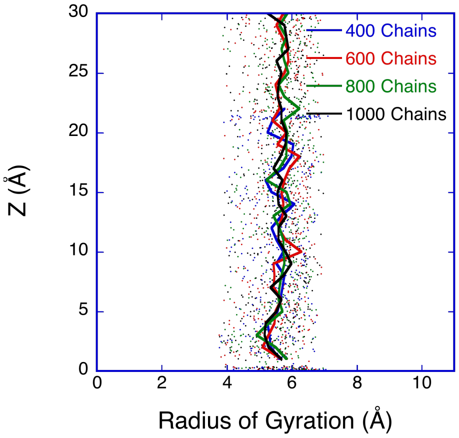

Figure 4.12. The average radius of gyration of alkane chains as a function of distance from the substrate surface. All values are shown as points, with binned averages presented as lines.

There are no obvious changes in radius of gyration as a function of position. At best, the chains closest to the surface might have a minutely smaller average R_g, but the magnitude of the difference is on par with the fluctuations throughout the system. It has also been argued that the interphase region thickness is roughly equivalent to R_g, but as shown previously, we see a clear layering behavior out to at least 2 R_g.

Mechanical properties were only determined for the nano-confined laminate systems with variable thickness, in order to identify the elastic response of the polymer near the interface. Uniaxial tension was applied at a constant strain rate perpendicular to the substrate surface, while maintaining the two perpendicular dimensions of the system constant. The stress-strain curves for each alkane thickness and a system of periodic alkane chains are presented in Figure 4.13.

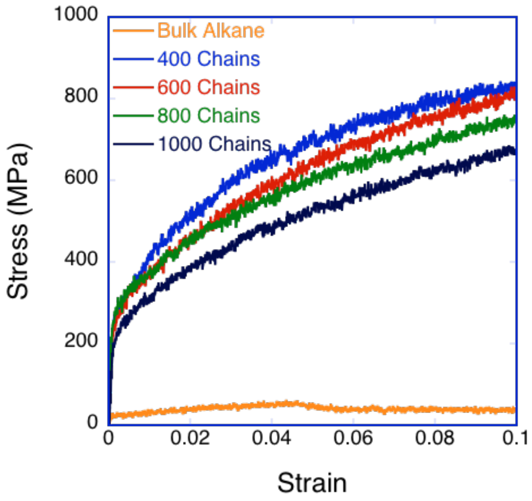

Figure 4.13. Stress strain curves for 4 different thickness of alkane on a Cu substrate and a periodic alkane system As expected, the modulus increases

In general, the thinnest layers show the greatest stiffness. This is expected, as the absolute thickness of the substrate was held constant, rather than the ratio between the two layers. The elastic moduli as a function of layer thickness are determined as the slope of the stress vs. strain curves at zero stress, using a parabolic fit to the region of the curve between 0.0 and 0.05 strain. To predict the composite strength, a simple linear spring series model for the rule of mixtures is used, given by Equation 4.2.

$$E_{mix} = \left(\frac{E_{alkane}}{t_{alkane}} + \frac{E_{Cu}}{t_{Cu}} \right)^{-1} t_{net}$$

Eq. 4.2. Linear spring series rule of mixtures

Where *E* is the Young's modulus and *t* is the thickness of the respective layers. Results are presented in Figure 4.14, compared to the expected modulus values according to Equation 4.2.

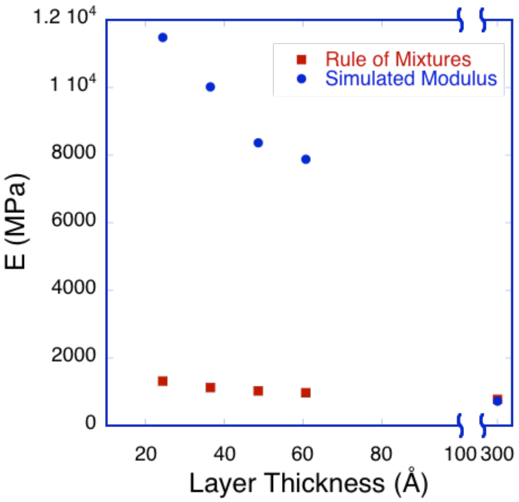

Figure 4.14. Elastic moduli for different layer thicknesses from simulation compared to the modulus expected from a simple rule of mixtures. The bulk alkane is placed at 300Å for comparison.

The net elastic modulus is highest in the thinnest layer, and decreases with increasing alkane thickness. However, the increased elastic modulus is well in excess of what would be predicted by of the relative thickness and modulus of the copper layer, and the modulus determined from the bulk alkane. As the layer thickness increases, the measured and predicted value seem to converge.

As discussed in the introduction, a number of models have been proposed for the interphase region. [11,19-22,24-31,43,44] One common description of the elastic modulus is to use a exponential scaling factor that varies with thickness, given in Equation 4.3.

$$E_{\text{int}} = E_0 e^{\beta x}$$

Eq. 4.3 Exponential scaling factor modulus

where E_o and β are constants empirically determined from the geometry and stiffness of a series of samples and x is the distance from the interface. At the nanoscale, the local properties such as density do not vary monotonously, but instead oscillate due to a markedly layered structure. It is expected that density strongly affects mechanical behavior, particularly given the system's stiffness depends on entanglements and intermolecular interactions. If we recall the 2-D pair correlation functions at different positions along the layer thickness in Figure 6, the interchain separation increases with distance from the substrate, scaling inversely with the density.

Molecular dynamics simulations allow us to consider the stress and strain behavior in the two components of the composite system separately in a way that cannot be done in experiment. Stress-strain curves are calculated from the sum of the directional pressure on each atom. By only including the hydrogen and carbon atoms, we can determine a partial stress-strain curves for the same tensile tests. The curves showing only the alkane layer stresses and strain are presented in Figure 4.15 for the four layer thicknesses.

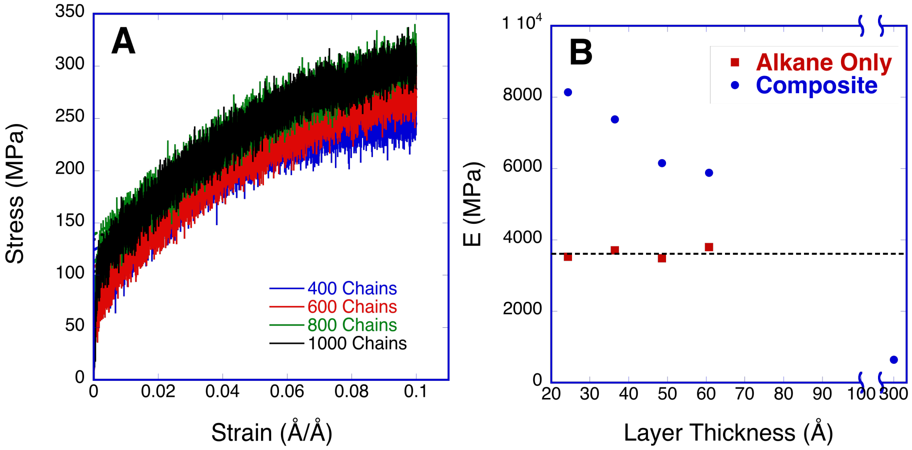

Figure 4.15. (a)Stress-strain curves derived from the alkane portion of the nanoconfined laminate and (b) updated modulus values

Unexpectedly, the curves are almost identical, with a Young's modulus of around 3.6 GPa for each of the four thicknesses. This is 5 times the modulus of the bulk alkane system. However, the density of these nanoconfined systems is higher than the bulk density (1.02g/cm3), and nearly the same for all four systems. Moreover, the alkane in the nanoconfined system is laterally confined by the stiffness of the copper, restricting the available deformation directions. To better understand the deformation behavior, the density profiles of the thickest and thinnest nanoconfined layers (62Å and 26Å, respectively) were monitored during strain. The complete profile is presented in Figure 4.16(a), with a closer examination of deformation near the substrate in Figure 4.16(b).

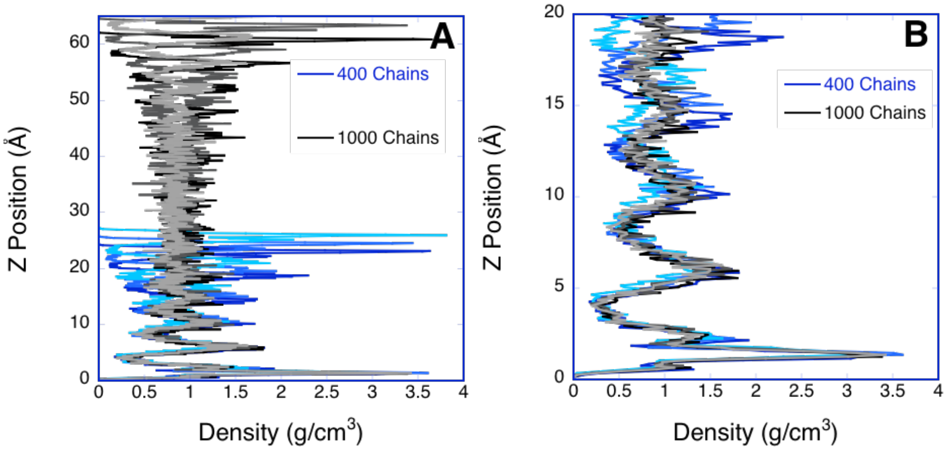

Figure 4.16. Comparing the density change for unstrained, and two different amounts of strain between the 400 chain and 1000 chain systems for (a) the complete region and (b) near the substrate. Line color is lightened as strain is increased.

The *z* axis in each system is set such that the bottom of the alkane layer defines zero, and both systems are shown for the undeformed state, and the 2Å and 4Å deformed states. The complete density profile shows that deformation is occurring fairly uniformly through the sample. Looking more closely at the first 20Å in Figure 16(b), the first two layers barely deformed, and are almost identical between the two systems. At approximately 10% strain, the 400 chain system starts to show some deformation near the surface, with a broadening of the gap between the first two layers. In general, the deformation seems to affect the lower density regions of the sample, i.e., the middle. In the thinner sample under constant strain, this results in a larger deformation of a smaller region, while the deformation in the thicker sample is more uniformly distributed across a wider region.

Based on these observations, while ordering continues beyond the initial density fluctuations, an interphase model for the nanoscale in entangled polymers should be based on the density of the system. In this case, because all alkane layers have the same net density, there is no difference in the modulus of the overall region. It is likely that sufficient thickness to leave the interphase region was not achieved in this study. Future work may explore the more localized modulus of each density layer within the alkane structure. However, it is evident even in this simple model system that the nanoscale interphase is a complex phenomenon.

4.4. Summary and conclusions

The introduction of an ordered substrate results in local heterogeneity within the amorphous polymer. The density profile was shown to be informative in describing the extent of the interphase region, while more traditional metrics, such as radius of gyration, were less informative. A method for examining the local pair correlations of layers was presented, showing a gradual shift in the ordering behavior of the system as a function of distance from the substrate

A closer examination of the structure of the alkane near the surface was performed. The lattice parameter of the substrate was shown to inversely correlate to the maximum alkane density, while being almost linearly correlated to interchain spacing in the surface layer. Increasing the interaction strength beyond the rules of geometric mixing, resulted in $\log_2$ correlation between the interaction strength and maximum density, with the inverse trend seen for interchain spacing. While some expected differences were observed between chain lengths, their trends in densification and ordering were similar across all alkanes studied.

The effect of alkane layer thickness was tested for four systems, using a common chain length and substrate. The elastic moduli were well above the expected values predicted from the bulk Cu and alkane moduli. Moreover, the stress-strain curves for only the alkane atoms of the system showed little difference as a function of thickness, but a universally higher modulus and density than that of the bulk periodic alkane system.

This simple model system has helped to identify metrics of interest for studying the interphase and interphase mechanics, as well as eludicated the role of the substrate on the structural characteristics of adjacent disordered materials. It is clear that studying thicker alkane layers could help clarify the nanoscale interphase, as true bulk behavior is not reached in samples under 60Å thick.

4.5. References

1. Ghorai PK, Glotzer SC (2007) Molecular Dynamics Simulation Study of Self-Assembled Monolayers of Alkanethiol Surfactants on Spherical Gold Nanoparticles. Journal of Physical Chemistry C 111: 15857.

2. Giro R, Caldas MJ (2007) Calcium deposition on poly (para-phenylene vinylene): Molecular dynamics simulations. Physical Review B 76: 161303.

3. Guymon CG, Harb JN, Rowley RL, Wheeler DR (2008) MPSA effects on copper electrodeposition investigated by molecular dynamics simulations. J Chem Phys 128: 044717.

4. Fan HB, Wong CKY, M.F.Yuen M (2008) A Multiscale Interfacial Delamination Model of Cu-SAM-Epoxy Systems. International Conference on Electronic Packaging Technology & High Density Packaging 2008:

5. Heinz H, Castelijns HJ, Suter UW (2003) Structure and phase transitions of alkyl chains on mica. J Am Chem Soc 125: 9500-9510.

6. J.S. Raut DSS, K.A. Fichthorn (1997) Molecular-dyanmics simulation of structures and dynamics of n-butane adlayers on Pt(111). Surface Science 389: 88-102.

7. Kisin S, Vukic; JB, Varst. PGT (2007) Estimating the Polymer-Metal Work of Adhesion from Molecular Dynamics Simulations.

8. Kawamata M, Yamamoto T (1997) Molecular dynamics simulation of surface ordering in liquid n-alkanes. Journal of the Physical Society of Japan 66: 2350-2354.

9. Guymon CG, Harb JN, Rowley RL, Wheeler DR (2008) MPSA effects on copper electrodeposition investigated by molecular dynamics simulations. J Chem Phys 128: 044717.

10. Stevens MJ (2001) Interfacial fracture between highly cross-linked polymer networks and a solid surface: effect of interfacial bond density. Macromolecules 34: 2710-2718.

11. Farah K, Leroy F, Muller-Plathe F, Bohm MC (2011) Interphase Formation during Curing: Reactive Coarse Grained Molecular Dynamics Simulations. J Phys Chem C 115(33): 16451-16460.

12. Kanzow J, Horn P, Kirschmann M, ZAPOROJTCHENKO V, DOLGNER K et al. (2005) Formation of a metal/epoxy resin interface. Applied Surface Science 239: 227-236.

13. Kulmi U, Basu S (2006) A molecular dynamics study of the failure modes of a glassy polymer confined between rigid walls. Modeling Simul Mater Sci Eng 14: 1071-1093.

14. Lin PH, Kohale SC, Khare R (2011) Effect of nanoconfinement on kinetics of cross-linking reactions: a molecular simulation study. J Phys Chem B 115: 12348-12355.

15. Malvaldi M, Bruzzone S, Raos G, Allegra G (2007) Equilibrium dynamics of an associating polymer melt in narrow slits by computer simulation. J Phys Chem B 111: 4141-4149.

16. Scheidler P, Kob W, Binder K (2002) Cooperative motion and growing length scales in supercooled confined liquids. Europhys Lett 59: 701-707.

17. Israelachvili JN (2011) Intermolecular and Surface Forces. Elsevier.

18. Ayatollahi MR, Shadlou S, Shokrieh MM (2010) Multi-scale modeling of nonlinear mechanical behavior of polymer/SWNT nanocomposites: Investigation of interphase. Enabling Science and Nanotechnology (ESciNano), 2010 International Conference on: 1-2.

19. Chaboche JL, Girard R, Schaff A (1997) Numerical analysis of composite systems by using interphase/interface models. Computational Mechanics 20: 3-11.

20. Chang YS, Lesko JJ, Case SW, Dillard DA, Reifsnider KL (1994) The Effect of Fiber-Matrix Interphase Properties on the Quasi-Static Performance of Thermoplastic Composites. Journal of Thermoplastic Composite Materials 7: 311-324.

21. Fisher FT, Brinson LC (2001) Viscoelastic interphases in polymer–matrix composites: theoretical models and finite-element analysis. Composites Science and technology 61: 731-748.

22. Jancar J (2008) Review of the role of the interphase in the control of composite performance on micro- and nano-length scales. J Mater Sci 43: 6747-6757.

23. Kaw AK, Selvarathinam AS, Besterfield GH (1992) Comparison of interphase models for a crack in fiber reinforced composite. Theoretical and Applied Fracture Mechanics 17: 133-147.

24. Kim J-K, Sham M-L, Wu J (2001) Nanoscale characterisation of interphase in silane treated glass fibre composites. Composites Part A: applied science and manufacturing 32: 607-618.

25. Li JY (2000) Thermoelastic behavior of composites with functionally graded interphase: a multi-inclusion model. International journal of solids and structures 37: 5579-5597.

26. Papanicolaou GC, Paipetis SA, Theocaris PS (1978) The concept of boundary interphase in composite mechanics. Colloid and Polymer Science 256: 625-630.

27. Reifsnider K, Stinchcomb W, Dillard D, Swain R, Jayaraman K (1992) Role of Interfaces and Interphases in the Evolution Mechanics of Material Systems.

28. Reifsnider KL (1994) Modelling of the interphase in polymer-matrix composite material systems. Composites 25: 461-469.

29. Subramanian S, Lesko JJ, Reifsnider KL, Stinchcomb WW (1996) Characterization of the Fiber-Matrix Interphase and its Influence on Mechanical Properties of Unidirectional Composites. Journal of Composite Materials 30: 309-332.

30. Wang Q, Chiang F-P (1996) Experimental characterization of interphase mechanical properties of composites. Composites Part B: Engineering 27: 123-128.

31. Yi S, Pollock GD, Ahmad MF, Hilton HH (1995) Effective transverse Young's modulus of composites with viscoelastic interphase. AIAA journal 33: 1548-1550.

32. Lee B, Park I, Yoon J, Park S, Kim J et al. (2005) Structural Analysis of Block Copolymer Thin Films with Grazing Incidence Small-Angle X-ray Scattering. Macromolecules 38: 4311-4323.

33. Metzger TH, Kegel I, Paniago R, Lorke A, Peisl J et al. (1998) Shape, size, strain and correlations in quantum dot systems studied by grazing incidence X-ray scattering methods. Thin Solid Films 336: 1-8.

34. Zhang J, Posselt D, Smilgies DM, Perlich J, Kyriakos K et al. (2014) Lamellar Diblock Copolymer Thin Films during Solvent Vapor Annealing Studied by GISAXS: Different Behavior of Parallel and Perpendicular Lamellae. Macromolecules 47: 5711-5718.

35. Fischer H (2002) Thermal Probe Surface Treatment of a Bulk Polymer: Does a Surface Layer with a Lower Glass Transition Than the Bulk Exist? Macromolecules 35: 3592-3595.

36. Fragiadakis D, Pissis P, Bokobza L (2005) Glass transition and molecular dynamics in poly (dimethylsiloxane)/silica nanocomposites. Polymer 46: 6001-6008.

37. Kim JH, Jang J, Zin W-C (2000) Estimation of the Thickness Dependence of the Glass Transition Temperature in Various Thin Polymer Films. Langmuir 16: 4064-4067.

38. Kim JH, Jang J, Zin W-C (2001) Thickness Dependence of the Glass Transition Temperature in Thin Polymer Films. Langmuir 17: 2703-2710.

39. Onard S, Martin I, Chailan J-F, Crespy A, Carriere P (2011) Nanostructuration in Thin Epoxy–Amine Films Inducing Controlled Specific Phase Etherification: Effect on the Glass Transition Temperatures. Macromolecules 44: 3485-3493.

40. Sun Y, Zhang Z, Moon K-S, Wong CP (2004) Glass transition and relaxation behavior of epoxy nanocomposites. J Polym Sci B Polym Phys 42: 3849-3858.

41. Tress M, Erber M, Mapesa EU, Huth H, Müller J et al. (2010) Glassy Dynamics and Glass Transition in Nanometric Thin Layers of Polystyrene. Macromolecules 43: 9937-9944.

42. Yang Z, Clough A, Lam C-H, Tsui OKC (2011) Glass Transition Dynamics and Surface Mobility of Entangled Polystyrene Films at Equilibrium. Macromolecules 44: 8294-8300.

43. Kaw AK, Selvarathinam AS, Besterfield GH (1992) Comparison of interphase models for a crack in fiber reinforced composite. Theoretical and Applied Fracture mechanics 37: 133-147.

44. Possart W, Kruger JK, Wehlack C, Muller U, Petersen C et al. (2006) Formation and structure of epoxy network interphases at the contact to native metal surfaces. Comptes Rendus Chimie 9: 60-79.

45. Aldridge M, Waas A, Kieffer J (2014) Spatially Resolved In-Situ Elastic Modulus of Thermoset Polymer Amidst Carbin Fibers in a Polymer Matrix Composite. Composites Science and Tehcnology 98:

46. Llorca J, Gonzalez C, Molina-Aldareguia JM, Segurado J, Seltzer R et al. (2011) Multiscale modeling of composite materials: a roadmap towards virtual testing. Adv Mater 23(44): 5130-5147.

47. Plimpton S (1995) Fast Parallel Algorithms for Short-Range Molecular Dynamics. J Comp Phys 117: 1-19.

48. Nanotechnology NFC (2009) NanoHub. Available: https://nanohub.org/ via the Internet.

49. Jorgensen WL, Tirado-Rives J (1988) The OPLS potential functions for proteins. Energy minimizations for crystals of cyclic peptides and crambin. Journal of the American Chemical Society 110: 1657-1666.

50. Daw MS, Foiles SM, Baskes MI (1993) The embedded-atom method: a review of theory and applications. Materials Science Reports 9: 251-310.

51. Foiles SM, Baskes MI, Daw MS (1986) Embedded-atom-method functions for the fcc metals Cu, Ag, Au, Ni, Pd, Pt, and their alloys. Physical Review B 33: 7983.

52. Heinz H, Vaia RA, Farmer BL, Naik RR (2008) Accurate Simulation of Surfaces and Interfaces of Face-Centered Cubic Metals Using 12– 6 and 9– 6 Lennard-Jones Potentials. The Journal of Physical Chemistry C 112: 17281-17290.

Chapter 5. Interfaces between glassy polymers and ordered substrates

5.0. Synopsis

A planar interface within an epoxy and carbon composite was simulated using molecular dynamics simulations, varying the thickness of the epoxy layer and the hardener resin chemistry of the epoxy. A common epoxy resin, diglycidal ether of bisphenol F (DGEBF) and two simple amine hardeners, diethylenetriamine (DETA) and triethylenetetramine (TETA) were used as precursors. Graphene layers were used to simulate the surface of an unsized PAN-based fiber. Epoxy networks were generated while confined between graphene layers using a dynamic reaction algorithm previously implemented for bulk epoxy systems.

A denser packing was seen in the epoxy adjacent to the graphene structure, which shows a tendency to form more ordered structures in this region of the epoxy. The overall shrinkage and network growth behavior as a function of cure was similar to the periodic bulk epoxy, with greater inconsistency in the density achieved during initial compression of the monomeric liquids. The percolation of an infinite cluster was somewhat delayed relative to a periodic bulk epoxy, but surprisingly unaffected by the thickness of the epoxy layer. The density of new network bonds does not track the local mass density, indicating that the interfacial structures hinder reactions at the substrate surface.

Mechanical properties were calculated from uniaxial tension tests perpendicular to the substrate. Only slight increases in the elastic moduli are seen with cure, though there are clear differences between the layers, as expected. The tensile strength shows a more obvious increase with cure, and also increases with decreasing layer thickness. Voids are identified by calculating the local mass densityon a mesh. Nucleation of voids appears to be fairly even throughout the epoxy layer thickness, starting at ~10% strain, with growth and coalescence of the voids occurring mostly in the middle of the epoxy layers, rather than as expected at the graphene surface. Overall void growth behavior is insensitive to degree of cure or thickness. Glass transition at various degrees of cure was calculated, but no clear trends emerged. However, structures that had been effectively annealed in the process of determining the glass transition temperature show a nearly uniform decrease in both stiffness and tensile strength.

5.1. Introduction

In the automotive and defense industries, there has been a clear push in recent years to reduce vehicle weight and improve fuel economy as a response to new NHSTA regulations and the needs of the battlefield.[1,2] Fiber reinforced polymer matrix composites (FPMCs), such as epoxy/carbon fiber, are a strong candidate for many of these applications, with a high strength-to-weight ratio and good toughness. However, our ability to model these materials is complicated by non-homogenous behavior at every length scale. Prior experimental work in the Kieffer group has shown that the longitudinal modulus of epoxy resin within 5 μm of the reinforcing fiber differs from the modulus of the bulk material by ~4.5%.[3-5] While this change may seem small, it is significant. For example, to induce such a stiffness change via strain hardening would require a strain three times larger than the failure strain. Identifying the underlying cause of this behavior is therefore critical to accurate prediction of failure of composite components.

There are two major precursors for carbon fibers, which result in different surface textures. Pitch-based fibers tend to be highly non-uniform with rough surfaces and no particular graphene sheet orientation. Fibers formed with polyacrylonitrile (PAN), have a more uniform surface made of graphene sheets wrapped around a more disordered core. [6] Myriad efforts to improve the strength of FPMCs have focused on modifying the fiber surface to improve adhesion between the fiber and the matrix [7-23] Strategies include oxidation of the carbon surface, modifying surface roughness, and use of sizing chemicals to bind with both the fiber and the polymer matrix. However, as the primary goal of this study is to investigate the effect of an ordered substrate on the matrix material; chemical reactions between the matrix and the fiber are beyond the current scope.

Simulations of the interface between epoxy and various reinforcement materials have been undertaken previously, with carbon nanotubes, graphene, alumina and copper being the most frequently chosen substrate or nanoparticle materials.[23-52] In many cases, the system size is quite small, under 100 monomers. It is unreported in a surprisingly large number of papers. Some prior work has explored the effect of sizing on the adhesion of monomers, or thin layers. [27,30,52,53] However, this was often only for the monomer, rather than looking at network formation. Fan *et. al.* did build corss-linked networks within Materials Studio, but used limited system sizes (to the extent these were even specified). The largest networks with an interface were published by Yang *et. al.*, studying a Novolac/bisphenol A network on a Cu substrate with no sizing.[42,48] The simulation of large-scale network formation on a sized substrate has not been published to date, to the best of our knowledge.

The majority of published epoxy simulations, as discussed in Chapter 3, involve aromatic amine hardeners, such as 4,4’-diaminodiphenyl sulfone (DDS), including the studies of interfacial behavior.[7-9,11,13,15-17,20,21,54-60] As previously studied in the bulk system, we use two different resin-hardener systems, namely, the single-chain aliphatic amines triethylenetetramine (TETA) and diethylenetriamine (DETA). These amines have a lower degree of shrinkage upon cure, making them desirable in many manufacturing scenarios sensitive to dimensional tolerance and residual strains. As in the bulk epoxy study discussed in Chapter Three, we are interested in the effects of system size and functionality. For the laminate structures, system size equates to thickness of the composite layers, keeping the cross-sectional area constant across all systems. Functionality effects were investigated for a single system size.

5.2.Computational Methods

As in the previous bulk studies of epoxy network formation, one epoxide monomer, diglycidal ether of bisphenol F (DGEBF), and two aliphatic amines, diethylenetriamine (DETA) and triethylenetetramine (TETA) were chosen as the resin and hardeners. These monomer structures are shown in Figure 5.1.

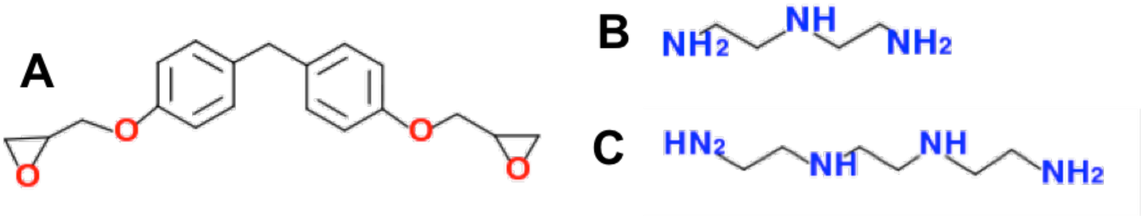

Figure 5.1. Monomers used are (a) diglycidal ether of bisphenol F (DGEBF), (b) diethylenetriamine (DETA) and (c) triethylenetetramine (TETA)

To study the interface between an epoxy matrix and a carbon fiber surface, a simple periodic laminate system was generated. Seven graphene layers were used to approximate the near-surface region of a PAN-type fiber, providing sufficient thickness to prevent false periodic interactions between the epoxy layers. The same cross section of 25 nm^2 was used for all simulations, and the amount of graphene kept constant, resulting in varying matrix to reinforcement ratios. Increasing the amount of epoxy in the system therefore increased the thickness of the matrix layer. The amount of graphene was chosen to avoid periodic self-interaction of the epoxy, as well as to avoid significant warping of the graphene sheets. To create the system, a large simulation box was created containing the graphene slab. Epoxide and amine monomers were randomly inserted in the vacuum layer above the substrate at an artificially low density.

Simulations were prepared for three system sizes: 595 monomers, ~1200 monomers, and 1785 monomers, which correspond to epoxy layer thicknesses of 70Å, 165Å and 240Å, respectively. The effect of amine functionality is explored to the intermediate size only. The OPLS-AA potential is used to describe all interactions, with all parameters listed in Appendix A. As graphene is an aromatic sp^2 carbon, no additional terms are required to describe the interactions between the substrate and the polymer matrix, given that aromatic carbon is already included as part of the DGEBF molecule. Sizing agents and chemical reactions between the matrix and fiber are beyond the current scope.

A somewhat complex procedure is required in order to condense the system enough to achieve experimental densities without creating residual stresses. This structure was energetically minimized using to the steepest descent algorithm. At a temperature of 1000 K, the box was rescaled in the free dimension (perpendicular to the interfaces) over 50 ps to 60-75% of the initial dimension, depending on the system size. A compressive pressure of 100 atm was then applied to the same dimension for a further 50 ps. The system was cooled under pressure over 250 ps, and the pressure gradually reduced to atmospheric pressure at room temperature over an additional 250 ps. Finally, the whole system was allowed to relax under constant pressure conditions at room temperature and atmospheric pressure over 250 ps. The total densification procedure takes 850ps, but all steps are important to creating a void-free structure with no significant stresses at the target density. This is verified by monitoring the per-atom virial stress, neglecting the kinetic energy term, which is defined according to Eq. 5.1:

$$S_{ab} = -\begin{bmatrix} \frac{1}{2}\sum_{n=1}^{N_{pairs}}\left(r_{1a}F_{1b}+r_{2a}F_{2b}\right)+\frac{1}{2}\sum_{n=1}^{N_{bonds}}\left(r_{1a}F_{1b}+r_{2a}F_{2b}\right)\ldots \\ \ldots+\frac{1}{3}\sum_{n=1}^{N_{angles}}\left(r_{1a}F_{1b}+r_{2a}F_{2b}+r_{3a}F_{3b}\right)+\frac{1}{4}\sum_{n=1}^{N_{dihed}}\left(r_{1a}F_{1b}+r_{2a}F_{2b}+r_{3a}F_{3b}+r_{4a}F_{4b}\right)\ldots \\ \ldots+Kspace\left(r_{i_a},F_{i_b}\right) \\ \end{bmatrix}$$

Eq. 5.1 Per-atom virial stress

where *a* and *b* are the respective *x*, *y* or *z* directions to generate the six components of the tensor, *r* is the position of the atom, and *F* is the respective force as defined by the coefficients and functions of the particular force field.[61,62] A more detailed discussion of the force field has been presented previously during the discussion of the bulk epoxy system. All parameters are given in Appendix A, Tables 2-5. Units are in MPa*Å^3, as the definition of the volume of an atom is ambiguous at best. The per-atom stress distributions before densification, after compression, and after relaxation are presented in Figure 5.2.

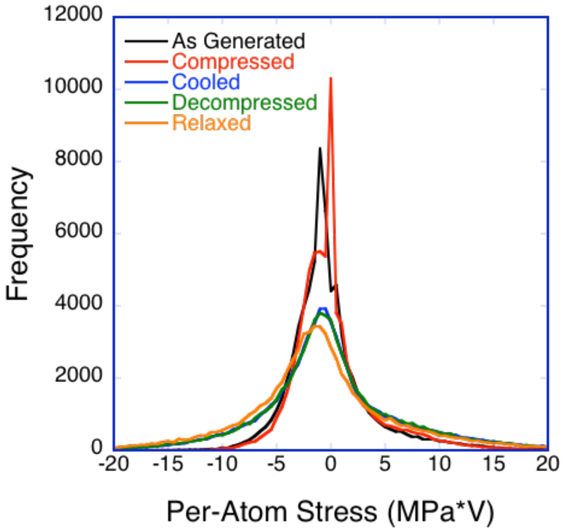

Figure 5.2. Per-atom stress distributions before densification, after compression, after cooling, after decompression and after relaxation

The low-density monomer structure, as generated, has a narrow stress distribution centered near zero. During densification, excess compressive stresses are generated, which are then mostly relieved during the cooling and decompression process. However, the final differences between the decompression and relaxation stage highlight the need for this final phase of the densification procedure.

The network growth of the epoxy matrix is simulated via a cut-off based algorithm, with an additional penalty term to account for the differing reactivities of the primary and secondary amine groups.[63,64] A detailed discussion of this algorithm is presented in Chapter 3. The requisite topology modifications for each new link are detailed in Appendix C. As part of these updates, the partial charges must also be updated, given the large polarity shift associated with the conversion of the oxygen in the epoxide ring to a hydroxyl group. Partial charges for all monomers, reacted dimers, and the second reaction of the terminal amine were calculated with Gaussian 09, using the HF/6-31G(d) exchange correlation functional. Reacted structures were first relaxed using MD simulations to reduce convergence time. Results showed that the changes in partial charge are restricted to atoms within 4 neighboring sites of the newly formed bond, so that only those atoms are modified. Comparison between the magnitude of change in the DETA and TETA partial charges upon reaction showed little difference, allowing us to use the same charge transfer rules for either hardener. The complete information for partial charges and changes thereof is described in Appendix B.

Mechanical properties were determined by a simple uniaxial tension test, with deformation perpendicular to the graphene substrate under constant pressure and a strain rate of 10^{-5}/fs. Stresses are determined according to the virial stress definition given in Eq. 1, summed over all atoms and normalized with respect to the system volume. While experiments often measure the interlaminar shear stress, we are primarily interested in the response of a possible interphase, rather than adhesion between the substrate and matrix. The uniaxial tension test more directly probes this change in the matrix. From the stress-strain curves generated by these tests, we examine both elastic and plastic behaviors.

5.3. Results and Discussion

The structure and mechanical properties of carbon-epoxy laminates were calculated during the cure process for three epoxy layer thicknesses, comparing two amine hardeners. Network growth, local stresses and structural heterogeneity are monitored and compared to previous results for a periodic bulk system. To study the elastic and plastic deformation behavior, uniaxial strain is applied in the direction normal to the interfaces.

Structure During Network Growth

The presence of an ordered substrate has been shown to affect the structure of amorphous materials. As described in the previous chapter, an ordered metallic substrate causes *n*-alkane chains to pack with a pronounced density layering in the vicinity of the surface. A similar effect is observed at the carbon-epoxy interface, shown in Figure 5.3.

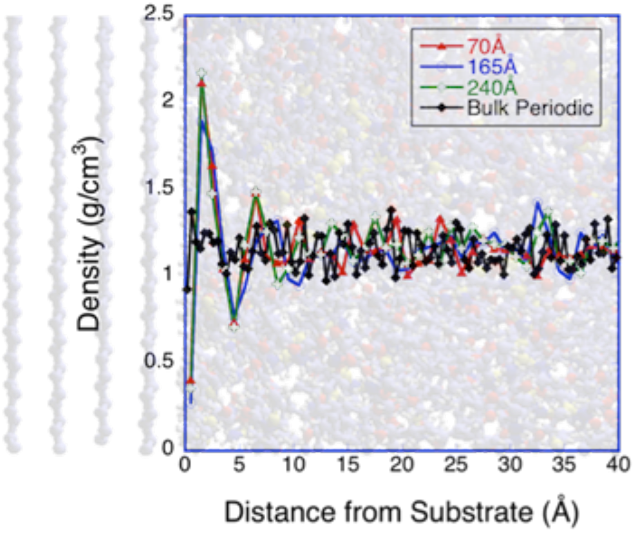

Figure 5.3. Mass density profiles for three laminate thicknesses and bulk epoxy superimposed on a rendered epoxy laminate structure to demonstrate the layering behavior

While the effect is less pronounced in epoxy than in the simple hydrocarbon case, there is still a clear layering effect in the mass density, with the maximum density nearly double that of the bulk regime. Based on this density profile, there are two clear peaks, within the first ~10Å of the interfacial region before density oscillations dissipate into a constant bulk density level. Fluctuations in density thereafter are of a similar magnitude as those observed in a bulk polymer grown with periodic boundary conditions in all three dimensions.

The atoms within the first, maximum-density layer adjacent to the substrate are rendered in Figure 5.4, and compared to a rendering of the atoms in a slice of the same thickness, taken from the middle of the epoxy phase, where it has returned to the bulk density behavior. Bonds between atoms contained within the slice are also rendered for clarity.

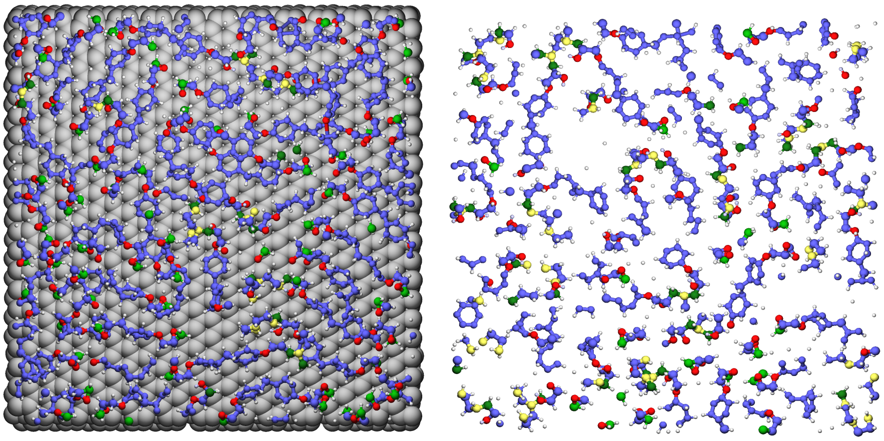

Figure 5.4. (a) The graphene surface and atoms within the first density layer and (b) an equivalently thick slice of a bulk periodic epoxy are rendered using POVray. Colors are assigned as follows: graphite (light gray), N (yellow), C (light blue), O (red), unreacted oxirane C (light green), reacted oxirane C (dark green), H (white).

The surface layer shows monomers lying predominately in the plane parallel to the graphite surface, while the orientation in the middle of the layer is expectedly more random. There is also some apparent clustering that could be indicative of a tendency for domain formation, but the available cross-sections are insufficient for statistically justifiable analysis. Due to the rigid nature of the DGEBF monomer and the fact that the two phenyl rings are not parallel to each other, the conformation with the substrate is limited. There are no visible differences in the structure of the first layer as a function of epoxy layer thickness or functionality.

Some changes in the local structure are expected in addition to the changes in density near the interface. The pair correlation function is used to describe the interatomic spacings, normalized to the average number density of the system. However, in the case of a free surface, or lamellar structure, this normalization factor is ill defined when the integration sphere surpasses the system boundaries. Instead, to analyze the behavior of the full epoxy layer, we calculate the bulk pair correlation function using only those atoms in the middle of the layer as centers, but use all atoms as potential neighbors.

In addition to analyzing the entire epoxy region, individual density layers are analyzed with a projected slice 2Å thick, taken parallel to the substrate surface, and normalized according to the density only of that slice. By projecting the atoms from a three-dimensional slice onto a two-dimensional plane, some smearing, particularly of short distance pairs, is expected. The pair correlation functions taken of the highest density layers, as well as an arbitrary section in the middle of the epoxy layer are compared to the overall pair correlation function of the epoxy layer in Figure 5.5.

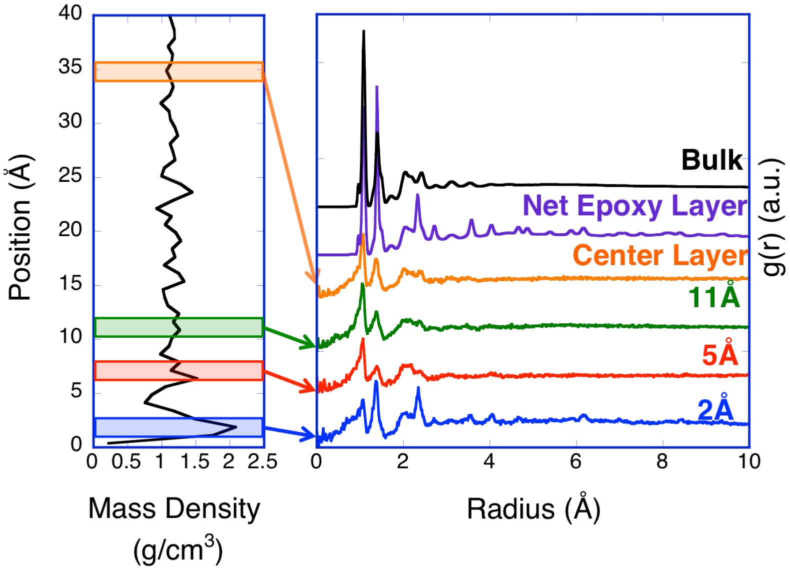

Figure 5.5. Projected [air correlation taken for 2.5Å thick slices at various points in the epoxy layer as indicated on the density profile and compared to the net epoxy layer, and a periodic bulk epoxy system

Looking at the pcf for the layer nearest the graphene surface, there is a significant increase in the magnitude of the peak at 1.4Å compared to those for the layers at 5Å or 11Å from the substrate. This layer also shows much sharper peaks for the second-neighbor distances between 2-2.5Å. Some small peaks propagate throughout. Due to the projection method, the peaks associated with hydrogen, such as 0.9Å (C-H), tend to be smeared. Other than this effect, the peaks begin to approach the behavior of bulk epoxy (determined for a system without substrate and subject to periodic boundary conditions in three dimensions) as the distance from the substrate increases. Interestingly, the pair correlation function for the full epoxy layer in the composite structure is strongly influenced by the ordering behavior near the substrate though it is a small fraction of the total volume.

Matrix shrinkage during cure is a major concern in process design of composite materials. Density was tracked throughout the curing of the epoxy matrix for each system, and is presented in Figure 5.6.

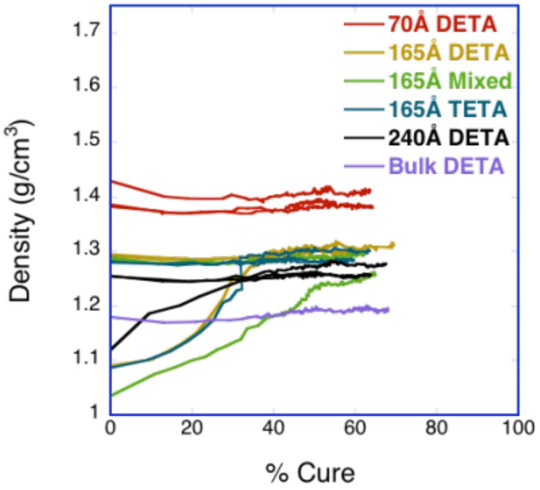

Figure 5.6. Density during cure of the laminate systems for all layer thickness and functionalities, compared to the density in a bulk periodic epoxy.

Several systems show a substantial increase in density compared to that of their initial configuration: these are not indicative of a fundamental shrinkage behavior, but the initial configuration densification was incomplete at the start of the reaction. The data is shown here to demonstrate that, despite the incomplete equilibration at the start, the polymerization procedure we employ yields unique results. For two thirds of all systems investigated, the initial configurations have the expected densities. As a function of the degree of cure, their densities exhibit a shallow minimum around 20% cure, and then compact to slightly above their initial density. These density evolutions are on par with the ones seen in the bulk periodic epoxy case, indicating no change in overall shrinkage due to the introduction of an interface. The different densities of the three system sizes are attributed to the differing relative amounts of epoxy located close to the interface with graphite: the thinner the layer, the more epoxy is affected by the interface, and the denser is the polymer structure.

In addition to shrinkage, we are concerned with the development of stresses as a function of the cure process. Using the per-atom stress definition previously discussed, the distribution of stresses as a function of conversion is presented in Figure 5.7.

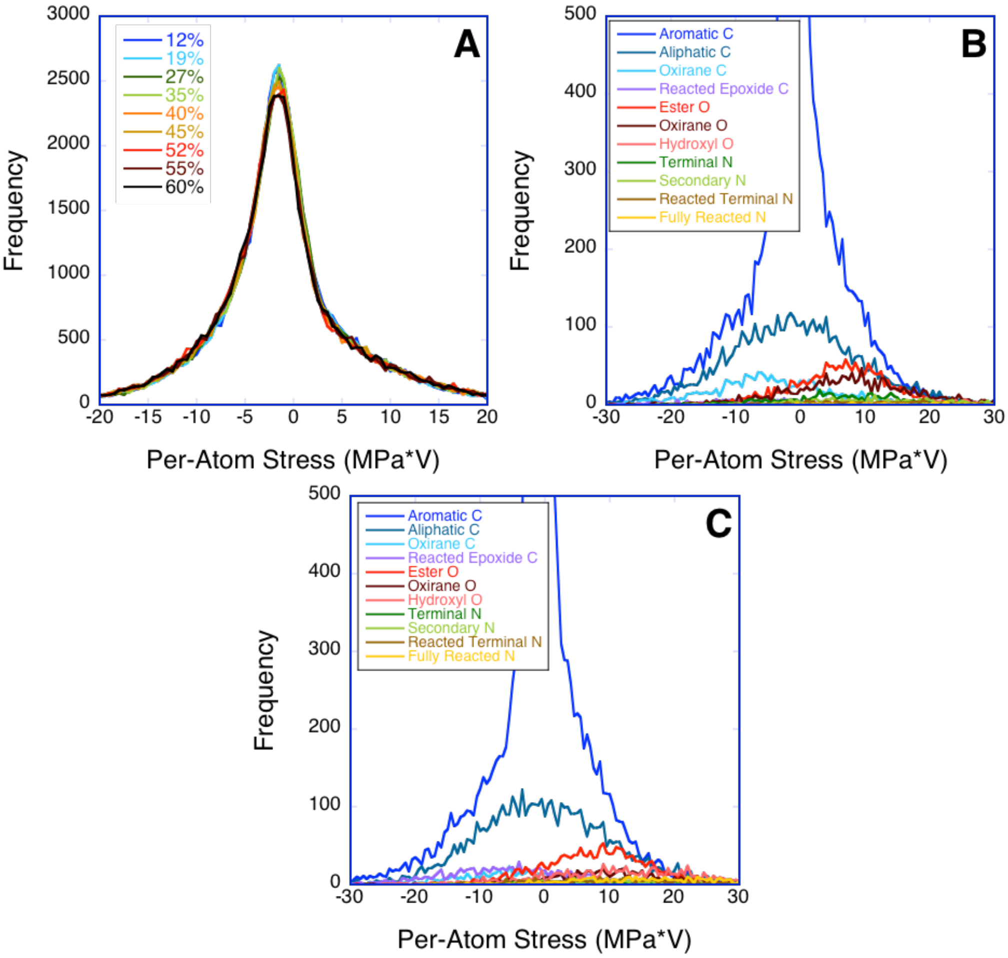

Figure 5.7. Distribution of per-atom stresses (a)at various degrees of cure in a 165Å thick epoxy layer and (b) by species at 12% cure and (c) by species at 60% cure

For the bulk system, as seen previously, the peak per-atom stress value shifts towards a net tensile stress with increasing degree of cure. In comparison, there is no change in the overall peak position for the epoxy sandwiched between two graphite surfaces, as seen in Figure 5.7(a). However, the overall distribution seems to broaden slightly. Note that this per-atom stress distribution includes the ones acting within the graphene sheets. Since the majority of aromatic carbon is located in the graphene slabs, which do not undergo any reactions, the stress experienced by this type of carbon, peaking at zero) remains unaffected by the degree of conversion. This is inferred from the species breakdown at 12% and 60% cure, shown in Figure 5.7(b) and 5.7(c), respectively. While the overall distributions do not show the same shifts seen in the bulk epoxy, the stresses for the backbone species are consistent with cure, as well as the prior results for the periodic bulk epoxy, indicating the difference in the overall per-atom stress behavior is largely due to the influence of the graphene carbon.

One of the common metrics for monitoring the growth of polymer networks is average molecular weight, particularly the mass-average molecular weight. To monitor the variation of molecular weight, the dispersity, which is the ratio between the mass-average and number-average molecular weights, was also calculated. Results for both are presented as a function of cure in Figure 5.8.

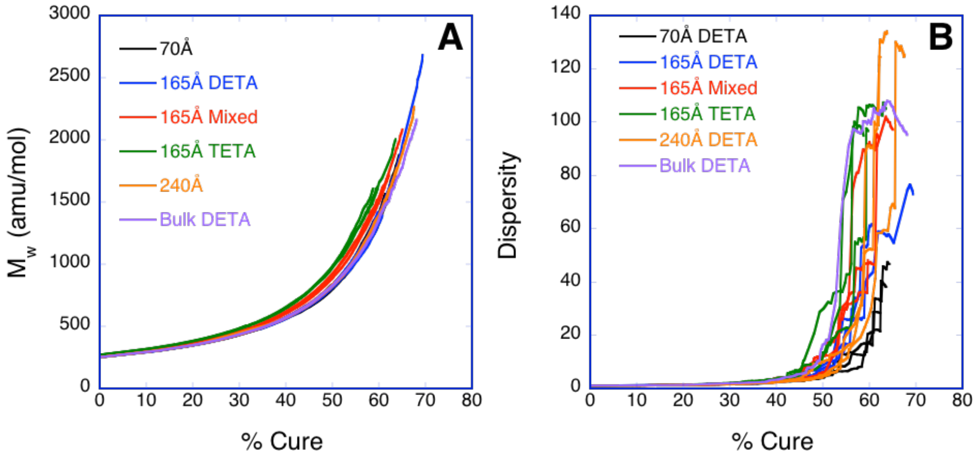

Figure 5.8. (a) Mass-average molecular weight and (b) dispersity as a function of cure for the difference thickness and functionality combinations of carbon-epoxy laminates

The mass-average molecular weight for the epoxy component as a function of cure was calculated for each system and is presented in Figure 5.8(a). As previously observed for the bulk epoxy systems, there are minor differences related to amine functionality, as is expected from the different masses of the two amine species used. The thickness of the system has no obvious influence on the network growth, and the network grows almost identically to a bulk system of the same chemistry. There is significantly more variation in the dispersity behavior, shown in 8(b). It is important to note that our dispersity values are unphysically high, due to errors associated with the statistics of small samples. Accordingly, the different system sizes have understandable differences in the maximum dispersity, as the fraction and size of the small clusters remains similar, but the maximum cluster size increases. The thinnest epoxy layer is the last to form an inifite cluster, indicated by the sudden uptick in the dispersity. The onset of percolation of the infinite cluster is similar to that in bulk epoxy, or very slightly delayed, as is expected by the effectively reduced dimensionality of the system.

To better understand the changes in molecular weight qualitatively, network development can be visualized by showing only reacted monomers, seen for a 165Å DETA system in Figure 5.9(a-c). The inverse can also be done, showing only the unreacted monomers in the system in Figure 5.9(d-f).

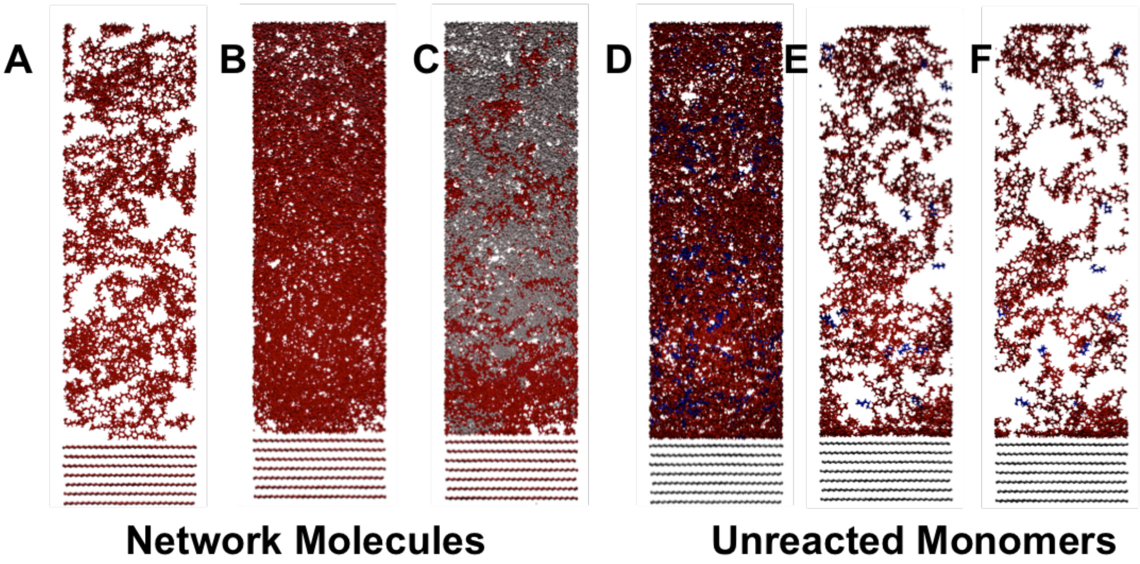

Figure 5.9. Rendering of the 160Å DETA epoxy system, showing (a-c) only the molecules which have joined the network, colored by molecule size (red: small, blue:large) and (d-f) the unreacted monomers (red: DGEBF, blue: DETA) at (a,d) 12% cure, (b,e) 55.5% cure and (c,f) 60.7% cure.

At the earliest stages of cure, a number of smaller clusters are formed, but as seen in Figure 5.9(a), the molecules at the surface are frequently not incorporated in the network. This is still evident in the rendering of the network at higher degrees of conversion, where gaps are visible, and by the number of unreacted monomers present at the surface even at higher degrees of cure. By 60% cure, in Figure 5.9(c), a continuous molecule spans the entire thickness of the slab, although several larger clusters remain unincorporated. Looking instead at the unreacted monomers, the resin and hardener seem evenly mixed in early phases, i.e., Figure 5.9(d). As cure progresses, there is a clear cluster of the DGEBF monomers on the graphite surface. Generally we observe that polyfunctional DETA monomers incorporate more rapidly into the network than the bifunctional epoxy resin, in agreement with previous quantitative analysis of the bulk epoxy.

The location of new network bonds through the epoxy thickness was also quantitatively monitored. Both the average density and fraction of epoxy rings in a given slice that have reacted are presented in Figure 5.10.

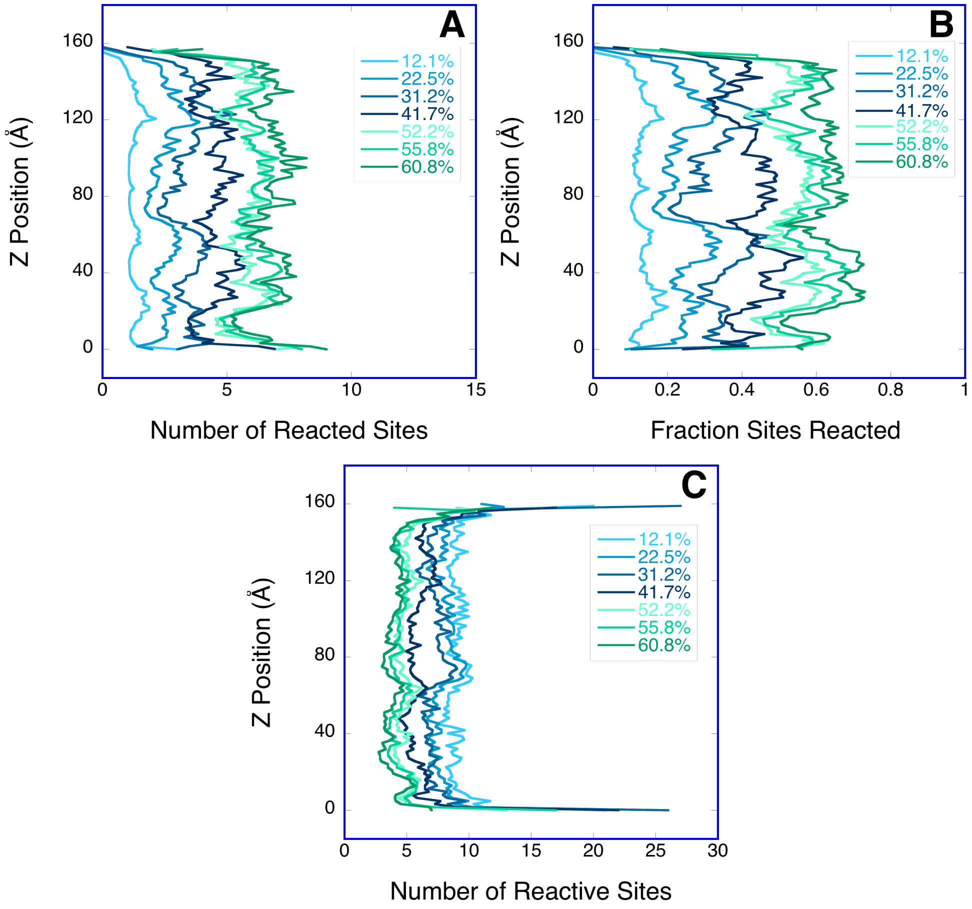

Figure 5.10. (a) the number of reacted sites through the thickness of the epoxy layer (b) normalized by the density of all epoxide sites in the layer and (c) number of reactive sites

While the number of reacted sites is fairly evenly distributed through the epoxy layer, the fraction of sites in a given layer that have reacted shows evidence of steric hindrance for functional groups near the interface as they react with a lower probability than throughout the remainder of the layer. New network bonds are formed throughout the layer, rather than nucleating at a particular point, as is expected with our polymerization procedure. It is possible that the addition of an autocatalytic term would change this behavior, which could dramatically affect the network growth behavior and mimic the effects of exothermic behavior seen experimentally. In addition to potential steric hindrance due to the presence of a substrate, demixing of the reaction partners may be an issue, as qualitatively observed in Figure 5.9(d-f).

Layering at the interface between the epoxy matrix and the fiber is observed, and some degree of ordering of epoxy in these layers is evident from visual inspection and the pair correlation function. Network stresses developed during cure were not noticeable due to the stress contributions of graphene substrate. Network growth as monitored by mass-average molecular weight and dispersity was surprisingly unaffected by the thickness of the epoxy layer, though the percolation of the infinite cluster was delayed compared to the periodic bulk epoxy network. Most interestingly, bonds did not form proportionally to local density immediately adjacent to interfaces, indicating steric hindrance effects in the higher density interfacial regions.

Mechanical Properties

Laminate composite materials are used in a wide variety of high-performance applications, such as racecars and fighter planes. As such, understanding of the mechanical properties is critical to effective design. The interface between carbon and epoxy, as well as the interfacial region of the epoxy matrix have been studied at various length scales. In order to focus on the effects of these structures on the mechanical properties, the properties in uniaxial tension, rather than in shear are analyzed. A series of uniaxial tensile tests under constant pressure conditions at a strain rate of 10^7/s were performed for the different thicknesses and as a function of the degree of cure. Stress-strain curves are generated by taking the sum of the per-atom stresses in the direction of interest, and normalizing with respect to the volume of the simulation box. These curves at various degrees of conversion of the 165Å thick DETA epoxy layer are presented in Figure 5.11.

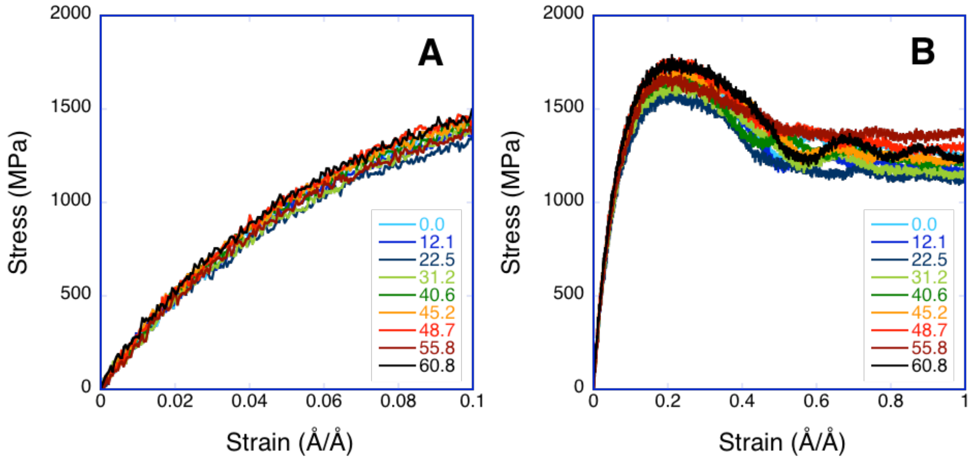

Figure 5.11. Stress-strain curves for various stages of cure in the 165Å thick DETA only system, showing (a) the elastic deformation region and (b) the extended strain region

From Figure 5.11(a), it is clear that within the range of conversion tested, elastic deformation is characterized by a fairly consistent non-linear stress-strain relationship. Note that the absolute amplitude of the stress fluctuations is comparable to those we observed for a bulk epoxy, the overall stress higher and therefore, the relative fluctuations are smaller. Beyond the elastic regime, as shown in Figure 5.12(b), the stress maximum occurs around 20% cure, which would be typically considered the onset of necking. An inflection at around 40% strain is associated with the drawing phase. As network growth progresses, the stress at the onset of necking, *i.e.,* the tensile strength, increases. The effect of system size on the stress-strain curve is shown in Figure 5.13.

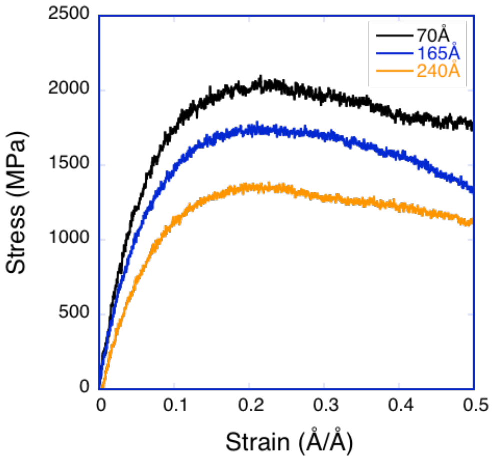

Figure 5.13. Stress-strain curves for each of the three thickness of epoxy layer at ~60% cure

As expected, the thinner the epoxy layer, the greater its tensile strength. A constant thickness of graphene was used, rather than a constant fraction, accounting for much of the difference between thicknesses. In all cases, the transition from elastic to plastic deformation seems consistent. In order to quantify the elastic behavior as a function of cure, the Young's moduli were calculated by taking the 0% strain slope of a parabolic fit of the 0-10% strain region. Results are presented in Figure 5.14.

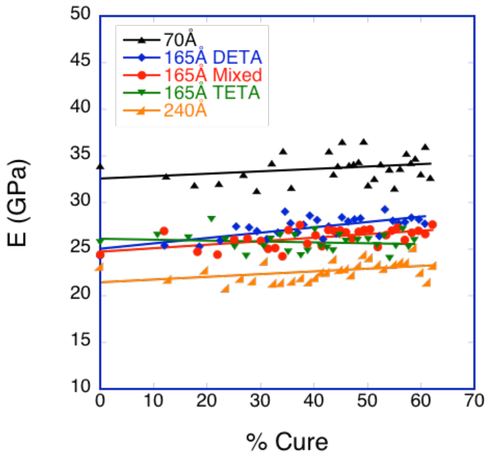

Figure 5.14. Elastic moduli as a function of cure determined from the 0% strain tangent of a parabolic fit of the stress-strain data.

As previously seen in bulk epoxy, there is only a trivial change in stiffness as a function of cure, of the same magnitude as the observed variations. The thinnest epoxy layer, with the highest graphene-to-epoxy ratio is the stiffest. However, the differences between the three system sizes are less than would be expected by a simple serial spring model for composite elasticity, given the high stiffness of graphene even in the transverse direction. There is no clear trend with regard to the amine functionality; all three systems behave very similarly.

The tensile strength was determined to describe the changes in deformation behavior due to network growth,. The maximum stress was found, and an average taken over a 0.1% strain region to minimize erroneous effects due to pressure fluctuations. These results are presented for the three thicknesses and different amine functionalities in Figure 5.15.

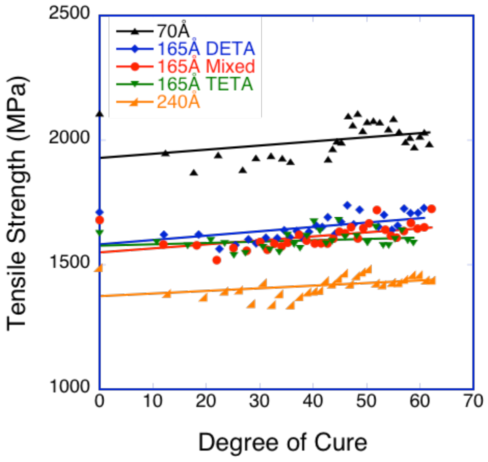

Figure 5.15. Tensile stress at the onset of necking as a function of cure.

The tensile strength is unexpectedly high in the uncured state in all systems. After an initial drop off, the tensile strength gradually increases with cure. Again, the thinnest system has the highest strength, but the amount of variability in the modulus values may be obscuring any differences between system sizes in the rate of strengthening with cure Differences between the three functionalities are within the range of noise, and require additional simulations to fully validate their significance or be disregarded.

During plastic deformation, the formation and growth of voids is expected, and indeed, critical to the prediction of fracture. The local mass density is calculated as a function of strain using a mass-conserving triquartic extrapolation for smoothing between cells, and avoid errors due to abrupt cutoffs, as described in Chapter 3. To qualitatively monitor void formation, the atomistic and bonded stucture is first rendered using the POVray graphics library. Voids are rendered using XCrysDen at an iso-density surface of 0.25 g/cm^3. Results for 10%, 20% and 50% strain of a 165 Å thick epoxy layer are presented in Figure 5.16.

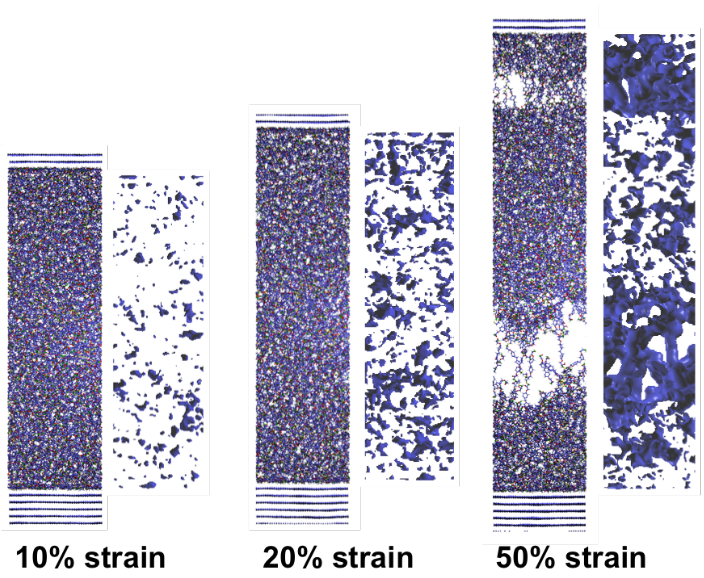

Figure 5.16. Renderings of network under tension and void formation at 10%, 20% and 50% strain

Voids begin to nucleate at low strains (10% or less). These voids are generally well dispersed throughout the system. Around 20% strain, voids begin to grow and coalesce. At high strains, large voids have formed, and rupture is now evident in the rendering of the atomistic structure. Interestingly, despite the density minimum beyond the compact first layer adhering to the substrate, shown in Figure 5.3, void growth does not occur substantially in the region. The overall void growth behavior is characterized as a function of cure and system size in Figure 5.17.

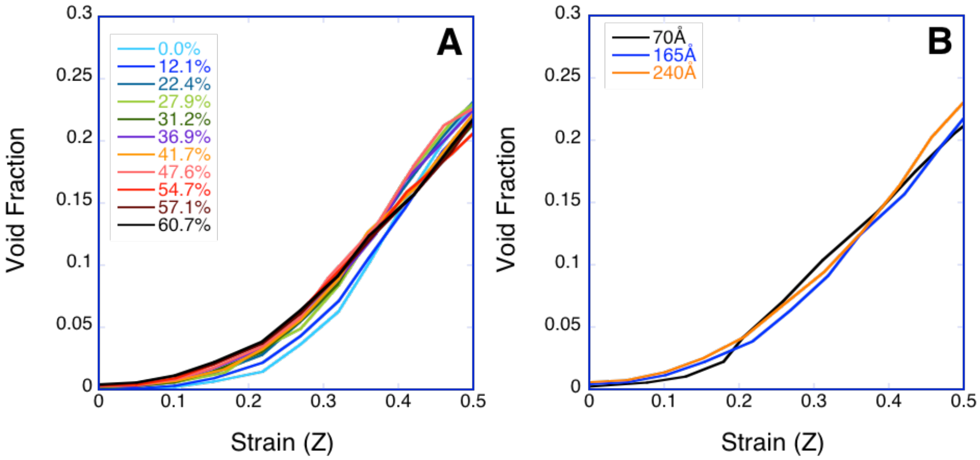

Figure 5.17. Net void volume fraction using 2Å cells and a density cutoff of 0.25g/cm^3 as a function of strain for (a) various cure stages of the 165Å epoxy layer and (b) 60% cure of the three layer thicknesses.

Unlike the bulk epoxy case, there is substantial void formation and growth even at low degrees of cure, due to cohesion of the epoxy layer. There are remarkably few differences between the different system sizes, as void nucleation typically begins near 10%, with a volumetric growth rate accelerating near 20% strain.

In addition to tensile properties, the glass transition temperature as a function of the degree of cure was determined. The glass transition temperature is akin to a second-order phase transition, identifiable by a change in the rate of change in the volume with respect to temperature. Samples are heated from 300K to 425K over 60ps to ensure they are above the glass transition temperature, held at 425K for 10ps, and then cooled from 425K to 200K over 100ps. The system is then returned to 300K over 10ps. The volume change of the system is monitored as a function of temperature, presented for various degrees of cure in Figure 5.18 (a) and (b).

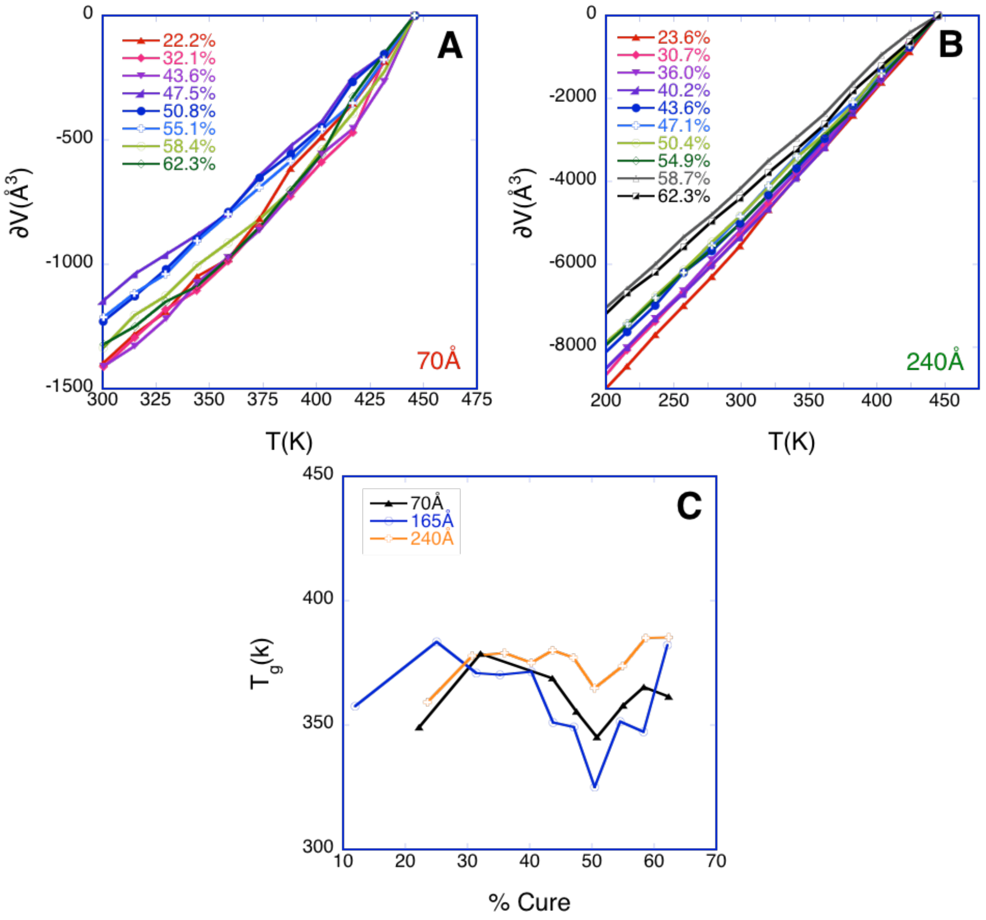

Figure 5.18. Volume change as a function of temperature for (a) 70Å thick and (b) 240Å thick epoxy, used to determine (c) glass transition temperature as a function of cure for three layer thicknesses.

According to our simulations, there is no particularly sharp transition apparent in in volume as a function of temperature. The volume rate of change is generally larger at lower degrees of cure, but this trend is not consistent, particularly for the thinner epoxy layer. In order to determine the glass transition temperature, linear fits were taken from 200K-250K, and 400K-425K, and the glass transition temperature is identified by the intersection of the two lines. The results, shown in Figure 5.18(c), exhibit no consistent trend with cure or system size. This is not unexpected, as the changes in volumetric contraction are too subtle.

The systems studied for glass transition also provide an opportunity for a preliminary analysis of annealing effects. The final structures of select systems that underwent the aforementioned thermal cycling were then used for the simulation of uniaxial tension testing. A comparison of the stress-strain curves with those for the as-cured samples is presented in Figure 5.19.

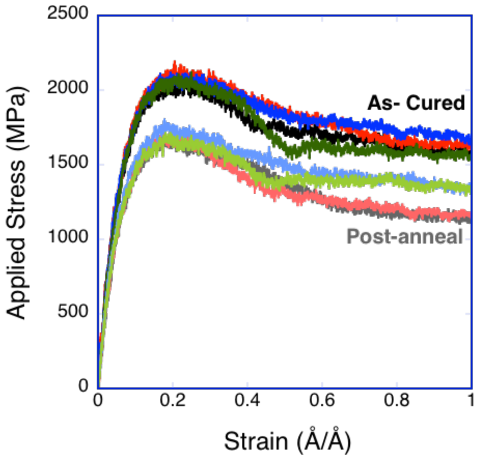

Figure 5.19. Stress-strain curves pre- and post- thermal cycling for several cure points of the 70Å thick epoxy system

The as-cured structures consistently reach higher applied stresses than the annealed ones for equivalent degrees of cure, though no significant density changes are noted. Above 40% strain, there is more change in the curves at higher degrees of cure, indicating some changes in the entanglement of the network. To quantify the shifts in mechanical properties pre- and post thermal cycling, the Young's moduli and tensile strength were determined. Results are presented in Figure 5.20.

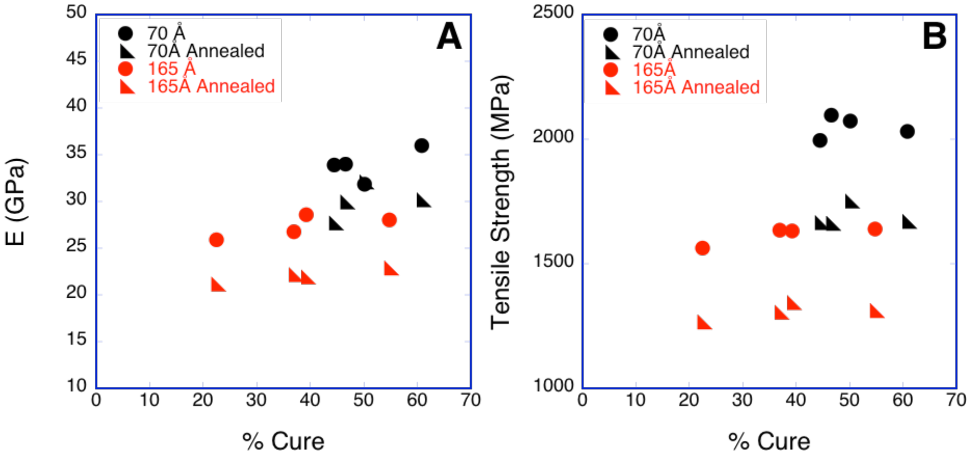

Figure 5.20. Comparing (a) Young's moduli and (b) tensile strength of structures as-cured and after thermal annealing for 70Å and 165Å thick epoxy at several degrees of conversion

Four different degrees of cure were tested for two different epoxy layer thicknesses. In nearly every case, the thermal cycle resulted in a notably reduced Young's modulus, with one configuration largely unchanged. The tensile strength universally decreases by ~300 MPa. Further work in needed to understand the internal structural changes leading to this shift, as density is largely unchanged, and no visible buckling of the graphene sheets has occurred.

While the stiffness was only slightly affected by cure, tensile strength increased noticeably with cure. As expected, layer thickness had a strong affect on the mechanical properties, as the ratio of epoxy and graphene in the system changes. Void nucleation and growth were monitored using a mass density meshing method. Renderings of the density isosurfaces show nucleation of voids throughout the system, but coalescence and growth occurs largely towards the middle of the layer. While the glass transition temperature analysis is largely inconclusive, the structures generated by the requisite thermal cycling show that annealing of the as-cured structures results in a definite decrease in stiffness and tensile strength. Further investigation into the differences between the as-cured and post-annealed structures could be highly informative.

5.4. Conclusions

Epoxy/carbon laminate structures were prepared to study the effects of amine functionality and epoxy thickness. The difference in amine functionality has minimal effect on the structure and mechanical properties of these systems. Exploration of longer aliphatic amines, or more complex aliphatic amines is suggested for future work.

Densification of the epoxy matrix adjacent to the graphene structure was observed, which showed a tendency to form more ordered structures. While there were greater inconsistencies in the initial compression of the monomer liquids, overall, shrinkage and network growth was fairly consistent with prior results for the periodic bulk epoxy. The percolation of an infinite cluster was somewhat delayed, but surprisingly unaffected by the thickness of the epoxy layer. New network bonds do not form proportionally to the local mass density, indicating that the more ordered structures near the substrate result in some steric hindrance.

Mechanical properties were calculated from constant strain rate uniaxial tension tests perpendicular to the substrate. Stiffness increased only slightly with network growth, though there are clear differences between different thicknesses of epoxy, as expected. Tensile strength shows a more obvious increase with cure, and also increases with decreasing layer thickness. A mass density mesh was calculated to locate and quantify void formation. Nucleation of voids appeared to be fairly uniform, starting at ~10% strain. At higher strain, the growth and coalescence of the voids occurs mostly in the middle of the epoxy layers, rather than at the surface. Glass transition as a function of cure was calculated, but no clear trends emerged. However, in the process, the generated structures that had been effectively annealed show a nearly uniform decrease in both stiffness and tensile strength. Further investigation of the structural details is needed to better understand this change.

Overall, the method previously demonstrated for generating bulk epoxy networks was effectively applied to a laminate composite structure. System sizes larger than the majority of the published literature were achieved. However, higher degrees of conversion need to be pursued. There also remain many other variables to explore, such as stoichiometry, sizing, surface roughness, and thermal cycling.

5.5. References

1. NHSTA Corporate Average Fuel Economy (CAFE) program. Available: http://www.nhtsa.gov/fuel-economy/ via the Internet.

2. TARDEC (2014) TARDEC: 30 Year Strategy.

3. Aldridge M, Sebeck K, Waas A, Kieffer J (2014) Micro-Scale Polymer Matrix Elastic Properties in Composites using Inelastic Light Scattering Measurements and Molecular Dynamics Simulations. Bulletin of the American Physical ...

4. Aldridge M, Waas A, Kieffer J (2014) Spatially Resolved In-Situ Elastic Modulus of Thermoset Polymer Amidst Carbin Fibers in a Polymer Matrix Composite. Composites Science and Tehcnology 98:

5. Aldridge MF, Waas AM, Kieffer J (2013) Elastic inhomogeneities in fiber towss of a textile polymer composite viainelastic light scattering. Materials Science and Technology

6. Matthews FL, Rawlings RD (1999) Compositre materials: Engineering and science. Cambridge: Woodhead Publishing Limited.

7. Fitzer E, Geigel KH, Huttner W, Weiss R (1980) Chemical Interactions Between the Carbon Fibre Surface and Epoxy Resins. Carbon 18: 389-393.

8. Johannesson T, Sjöblom P, Seldén R (1984) The detailed structure of delamination fracture surfaces in graphite/epoxy laminates. Journal of Materials Science 19: 1171-1177.

9. Takahagi T, Ishtani A (1988) XPS study on the surface structure of carbon fibers using chemical modification and C1s line shape analysis. Cabon 26: 389-396.

10. Drzal LT (1990) The Effect of Polymeric Matrix Mechanical Properties on the Fiber-Matrix Shear Strength. Materials Science and Engineering A 126: 289-293.

11. Donnet J-B, Park S-J (1991) Surface characteristics of pitch-based carbon fibers by inverse gas chromatography method. Carbon 29: 955-961.

12. Hughes JDH (1991) The Carbon Fibre/Epoxy Interface - A Review. Composites Science and Technology 41: 13-45.

13. Dong S, Gauvin R (1993) Application of Dynamic Mechanical Analysis for the Study of the Interfacial Region in Carbon Fiber/Epoxy Composite Materials. Polymer Composites 14: 414.

14. Huang Y, Young RJ (1994) Analysis of the fragmentation test for carbon-fibre/epoxy model composites by means of Raman spectroscopy. Composites Science and Technology 52: 505-517.

15. Hentschel MP, Harbich KW, Lange A (1994) Nondestructive evaluation of single fibre debonding in composites by X-ray refraction. NDT & E International 27: 275-280.

16. Wu GM, Schultz JM, Hodge DJ, Cogswell FN (1995) Effects of Treatment on the Surface Composition and Energy of Cabron Fibers. Polymer Composites 16: 284.

17. Sherwood PMA (1996) Surface analysis of carbon and carbon fibers for composites. Journal of Electron Spectroscopy and Related Phenomena 81: 319-342.

18. Tang L-G, Kardos JL (1997) A Review of Methods for Improving the Interfacial Adhesion Between Carbon Fiber and Polymer Matrix. Polymer Composites 18: 100.

19. Weitzsacker CL, Xie M, Drzal LT (1997) Using XPS to Investigate Fiber/Matrix Chemical Interactions in Carbon-fiber reinforced Composites. Surface and Interface Analysis 25: 53-63.

20. Ryu SK, Park BJ, Park SJ (1999) XPS Analysis of Carbon Fiber Surfaces--Anodized and Interfacial Effects in Fiber-Epoxy Composites. Journal of colloid and interface science 215: 167-169.

21. Sun YP, Fu K, Lin Y, Huang W (2002) Functionalized carbon nanotubes: properties and applications. Acc Chem Res 35: 1096-1104.

22. Rana S, Alagirusamy R, Joshi M (2009) A review on carbon epoxy nanocomposites. Journal of Reinforced Plastics and Composites 28: 461.

23. Liu A, Wang KW, Bakis CE (2011) Effect of functionalization of single-wall carbon nanotubes (SWNTs) on the damping characteristics of SWNT-based epoxy composites via multiscale analysis. Composites Part A: Applied Science and Manufacturing 42(11): 1748-1755.

24. Gou J, Minaie B, Wang B, Liang Z, Zhang C (2004) Computational and experimental study of interfacial bonding of single-walled nanotube reinforced composites. Computational Materials Science 31: 225-236.

25. Liang Z, Gou JJ, Zhang C, Wang B, Kramer L (2004) Investigation of molecular interactions between (10, 10) single-walled nanotube and Epon 862 resin/DETDA curing agent molecules. Materials Science and Engineering A 365: 228-234.

26. Wu C, Xu W (2006) Atomistic molecular modelling of crosslinked epoxy resin. Polymer 47: 6004-6009.

27. Knaup JM, Kohler C, Frauenheim T, Blumenau AT, Amkreutz M et al. (2006) Computational studies on polymer adhesion at the surface of gamma-Al2O3. I. The adsorption of adhesive component molecules from the gas phase. J Phys Chem B 110: 20460-20468.

28. Wu C, Xu W (2007) Atomistic molecular simulations of structure and dynamics of crosslinked epoxy resin. Polymer 48: 5802-5812.

29. Frankland SJV, Gates TS (2007) Local Elastic Constants for Epoxy-nanotube Composites from Molecular Dynamics Simulation. Materials Research Society Fall Meeting

30. Fan HB, Wong CKY, Yuen MMF (2008) A Multiscale Interfacial Delamination Model of Cu-SAM-Epoxy Systems. International Conference on Electronic Packaging Technology & High Density Packaging 2008:

31. Frankland SJV, Clancy TC (2008) Molecular Dynamics Simulation of Adhesion at Epoxy Interfaces. American Society fro Composites Proceedings

32. Lin P-H, Khare R (2009) Molecular Simulation of Cross-Linked Epoxy and Epoxy-POSS Nanocomposite. Macromolecules 42: 4319-4327.

33. Zhang FH, He XD, Dong LH, Yin YS (2009) Molecular Simulation of the Interfacial Properties of an Epoxy Composite Reinforced Using a Carbon Nanotube/Carbon Fiber Hybrid. Advanced Materials Research 79: 1289-1292.

34. Yu S, Yang S, Cho M (2009) Multi-scale modeling of cross-linked epoxy nanocomposites. Polymer 50: 945-952.

35. Yang S, Gao F, Qu J (2011) Modeling Separation Behavior of Epoxy/Cu Interface using Molecular Dynamics Simulation. Electronic Components and Technology Conference 1110-1114.

36. Choi J, Yu S, Yang S, Cho M (2011) The glass transition and thermoelastic behavior of epoxy-based nanocomposites: A molecular dynamics study. Polymer 52(22): 5197-5203.

37. Cui H-, Li D-, Fan Q (2012) Adhesion of a novel flexible epoxy molding compound and its molecular dynamics simulation. International Journal of Adhesion and Adhesives 35: 50-54.

38. Li C, Browning AR, Christensen S, Strachan A (2012) Atomistic simulations on multilayer graphene reinforced epoxy composites. Composites Part A: Applied Science and Manufacturing 43(8): 1293-1300.

39. Ionita M (2012) Multiscale molecular modeling of SWCNTs/epoxy resin composites mechanical behaviour. Composites Part B: Engineering

40. Salahshoor H, Rahbar N (2012) Nano-scale fracture toughness and behavior of graphene/epoxy interface. J Appl Phys 112(2): 023510.

41. Zhang X, Du L, Xu Z (2012) The effect of soft bake on adhesion property between SU-8 photoresist and Ni substrate by molecular dynamics simulation. J Appl Polym Sci n/a-n/a.

42. Yang S, Gao F, Qu J (2013) A molecular dynamics study of tensile strength between a highly-crosslinked epoxy molding compound and a copper substrate. Polymer 54: 5064-5074.

43. Mortazavi B, Benzerara O, Meyer H, Bardon J, Ahzi S (2013) Combined molecular dynamics-finite element multiscale modeling of thermal conduction in graphene epoxy nanocomposites. Carbon 60: 356-365.

44. Okabe T, Takehara T, Inose K, Hirano N, Nishikawa M et al. (2013) Curing reaction of epoxy resin composed of mixed base resin and curing agent: Experiments and molecular simulation. Polymer 54: 4660-4668.

45. Rahman R, Haque A (2013) Molecular modeling of crosslinked graphene–epoxy nanocomposites for characterization of elastic constants and interfacial properties. Composites Part B: Engineering 54: 353-364.

46. Shokuhfar A, Arab B (2013) The effect of cross linking density on the mechanical properties and structure of the epoxy polymers: molecular dynamics simulation. J Mol Model 19: 3719-3731.

47. Hölck O, Bauer J, Braun T, Walter H, Wittler O et al. (2013) Transport of moisture at epoxy–SiO2 interfaces investigated by molecular modeling. Microelectronics Reliability 53: 1111-1116.

48. Yang S, Qu J (2014) An invesitgation of the tensile deformation and failure of an epoxy/Cu interface using coarse-grained molecular dynamics simulations. Modelling and simulation in materials science and engineering 22: 065011.

49. Kim D-H, Kim H-S (2014) Investigation of hygroscopic and mechanical properties of nanoclay/epoxy system: Molecular dynamics simulations and experiments. Composites Science and Technology 101: 110-120.

50. Sawa F, Imai T (2014) Molecular Dynamics Simulation for Epoxy-based Nanocomposites. ISEIM 327-329.

51. Shokrieh MM, Esmkhani M, Shokrieh Z, Zhao Z (2014) Stiffness prediction of graphene nanoplatelet/epoxy nanocomposites by a combined molecular dynamics–micromechanics method. Computational Materials Science 92: 444-450.

52. Sindu BS, Sasmal S (2015) Evaluation of mechanical characteristics of nano modified epoxy based polymers using molecular dynamics. Computational Materials Science 96: 146-158.

53. Fan HB, Yuen MF (2007) Material properties of the cross-linked epoxy resin compound predicted by molecular dynamics simulation. Polymer 48: 2174-2178.

54. Brenner DW, Harrison JA, White CT, Colton RJ (1991) Molecular dynamics simulations of the nanometer-scale mechanical properties of compressed Buckminsterfullerene. Thin Solid Films 206: 220-223.

55. Weitzsacker CL, Xie M, Drzal LT (1997) Using XPS to Investigate Fiber/Matrix Chemical Interactions in Carbon-fiber reinforced Composites. Surface and Interface Analysis 25: 53-63.

56. Eitan A, Jiang K, Dukes D, Andrews R, Schadler LS (2003) Surface modification of multiwalled carbon nanotubes: toward the tailoring of the interface in polymer composites. Chem Mater 15: 3198-3201.

57. Zussman E, Chen X, Ding W, Calabri L, Dikin DA et al. (2005) Mechanical and structural characterization of electrospun PAN-derived carbon nanofibers. Carbon 43: 2175-2185.

58. Liu L, Wagner HD (2005) Rubbery and glassy epoxy resins reinforced with carbon nanotubes. Composites Science and Technology 65: 1861-1868.

59. Koyanagi J, Yoneyama S, Eri K, Shah PD (2010) Time dependency of carbon/epoxy interface strength. Composite Structures 92: 150-154.

60. Sun LH, Ounaies Z, Gao XL, Whalen. CA (2011) Preparation, Characterization, and Modeling of Carbon Nanofiber/Epoxy Nanocomposites.

61. Van Dommelen L (2003) Physical interpretation of the virial stress.

62. Zimmerman JA, Webb III EB, Hoyt JJ, Jones RE, Klein PA et al. (2004) Calculation of stress in atomistic simulation. Modelling and simulation in materials science and engineering 12: S319.

63. Rohr DF, Klein MT (1990) Modeling Diffusion and Reaction in Cross-Linking Epoxy-Amine Cure Kinetics: A Dynamic Percolation Approach. Ind Eng Chm Res 29: 1210-1218.

64. Varshney V, Patnaik SS, Roy AK, Farmer BL (2008) A molecular dynamics study of epoxy-based networks: Cross-linking procedure and prediction of molecular and material properties. Macromolecules 41: 6837-6842.

Chapter 6. Conclusions and Future Work

Throughout this thesis, we have investigated the importance of local heterogeneity and network structure in the structure-property relationship analysis of amorphous materials through atomistic simulations. Both inorganic and organic bulk amorphous systems are studied, as well as two different amorphous systems on ordered substrates.

In silicate glasses, the clustering of network cations and the second-shell neighborhood affect the vibrational modes and mechanical properties. Mean-field rigidity theory is shown to be unable to account for mixed modifier effect in soda lime silicate glasses. Some evidence of non-random cation mixing is observed, with an observed tendency to form unlike cation pairs. Trends in simulated mechanical properties are generally in agreement with available experimental data.

The IR spectra of these glasses are computed and analyzed. A Fourier Filtered Atomic Trajectory method to further understand the structural units responsible for specific vibrational behaviors is applied and presented. Results for peaks in the IR spectra of pure silica and sodium disilicate glasses agree well with prior experimental investigations. However, the shoulder observed at 960 cm^{-1}, which is typically attributed to non-bridging oxygen, is shown to relate to an asymmetric stretching of the Si-O-Si unit. Analysis of the speciation of the silica atoms is not directly conclusive, indicating a possible anharmonic behavior of the network leading to the development of this vibrational mode.

Further investigation of the mixed modifier effect is needed to better understand the role of the cation in rigidity. Additionally, analysis of the relationships between cations and ring buckling in soda lime silicates may offer insight into the bulk modulus behavior observed. The mixed network former effect, such as in sodium borosilicate glasses, is not discussed in this thesis, but preliminary work has been completed. This has been only minimally investigated in simulation, and no prior work in network theory of mixed oxides was found. The majority of commercial oxide glass compositions have complex chemistry, including multiple glass-forming elements.

The structural and mechanical properties are studied for a dynamically reacted bulk epoxy network, demonstrating a polymerization method allowing us to monitor properties as a function of continuous growth of a network, including volumetric shrinkage and internal stresses. Network growth itself is monitored by tracking the molecular weight and corresponding statistics. For all combinations of system size, functionality, and mixing ratios, a number of small molecules are formed and then grow, before joining to form an infinite network. Systems with a surplus of amine hardener reach higher degrees of epoxide conversion, but the formation of an infinite network is delayed. Steric hindrance prevents complete conversion, with some smaller clusters trapped within the larger network. System size and functionality have limited effects on any of the structural metrics considered.

The elastic properties are only minimally changed by the growth of the network within the degrees of conversion achieved. Tensile strength, however, increases as a function of cure. The lack of local stresses or monomer deformation indicates that entanglement between molecules dominates the mechanics at the achieved degrees of cure. Further relaxation of the structure within the reasonable confines of molecular dynamics simulations does not consistently affect mechanical properties. Amine functionality also has no clear effect on the mechanical properties, as anticipated from the structural results. Increasing the system size does not alter the average mechanical properties as a function of cure, but improves the quality of results.

One area of interest for future work would be to explore the effects of initial mixing on cure. It has been shown in the self-healing community that poor mixing of the resin and hardener agents leads to poor cure behavior. While no major differences were seen between DETA and TETA, a larger difference in amine functionalities may still be of interest. Additional system sizes, both smaller and larger than those studied here, should be simulated to see if there is a clear threshold behavior, or a more general convergence. Higher degrees of conversion should be pursued in all cases.

As a simple model system to understand interfaces between amorphous and ordered materials, a simple alkane film was placed on a metallic substrate. The introduction of an ordered substrate creates a layered structure within the first 10 Å of the surface, shown by the density behavior, as well as pair correlation functions and monomer orientation. The ordering of the lattice is also shown to influence the structure of the alkane film near the interface, with lattice parameter shown to change spacing between alkanes on the surface. Difference in interfacial interaction strength between metal substrates shows little effect in most cases. However, altering the interaction strength independently, a $\log_2$ power law behavior is seen for the maximum density, as well as location of the maximum density layer.

This structural change also affects the mechanical properties of the system. The elastic moduli of nanoconfined alkane systems are shown to be higher than the simple composite strength of the two material. However, computing the mechanics properties of the alkane layers separately, layer thickness has no major effect on the elastic modulus. While alkane/metal interfaces are chosen as a simple model system, further investigation into longer alkane chain lengths, and different surface orientations of metal would be valuable to answer some lingering questions. Investigations of polyethylene and non-monodisperse systems would be valuable. Based on experimental investigations of film thickness effects on the glass transition temperature, polystyrene would be interesting.

Lastly, a series of epoxy/carbon laminate systems were investigated, comparing different epoxy layer thicknesses and amine functionality, using the same resin and hardeners previously explored. As seen in the alkane/metal composites, a dense layer is seen in the amorphous epoxy layer adjacent to the graphene substrate. The overall cure and shrinkage behavior mimicks the bulk epoxy, though the percolation of an infinite cluster is delayed. However, network formation is largely unaffected by the thickness of the epoxy layer, though overall mechanical properties followed expected trends based on the epoxy to carbon ratio. During plastic deformation, nucleation of voids appeared to be well-distributed through the thickness, rather than localized at the substrate surface. Annealing of structures in the process of determining the glass transition temperature shows a nearly uniform decrease in both the elastic module and tensile strength, and should be explored further.

There is still significant work to be done in order to improve these models, and bring them closer to the commercial carbon fiber composite systems. First and foremost, fiber surface oxidation and sizing agents need to be investigated. Oxidation of graphene leads to the formation of oxirane structures, which could lead to more direct bonding between the substrate and the network. Based on the results from the bulk epoxy, the effect of stoichiometry in laminate systems should be investigated. There is also a significant range of chemistry to be investigated, for different amine compounds, as well as different epoxide agents. Additionally, the interactions between epoxy and other fiber surfaces, such as E-glass or oxides like ZnO should be studied. Surface roughness, as would be expected in the cheaper pitch-based carbon fibers, should also be investigated.

It is clear that the presented work has only begun to address the question of the nature of amorphous networks and the structural changes in amorphous materials near an interface. Local heterogeneity is important in predicting nanoscale mechanics for all systems investigated. System size was also shown to be important in convergences of mechanical properties derived from simulation of highly cross-linked network polymers.

Appendix A: Interaction parameters for all simulations

Table A-1: FLX potential parameters for sodium-calcium-silicate and sodium-borate-silicate glasses

Element	σ_i *(nm)*	n_i	z_i	$q_i^{\varnothing}$	μ
Na	0.1300	8	+1	+1	4.149
Ca	0.1560	8	+2	+2	4.149
Si	0.1010	8	+4	+4	4.149
O	0.1430	8	-2	-2	5.803

Pair	A_{ij} (10^{-19} J)	ρ_{ij} (nm^{-1})	λ_{ij} (nm)	η_{ij} (nm)	κ_{ij} (nm^{-1})
Na-Na	0.5327	35.00	0.0	0.0	35.00
Na-Ca	0.2450	35.00	0.0	0.0	35.00
Na-Si	0.1450	35.00	0.0	0.0	35.00
Na-O	0.1977	35.00	0.0	0.0	35.00
Ca-Ca	0.1900	20.44	0.0	0.0	20.44
Ca-Si	0.1450	20.47	0.0	0.0	20.47
Ca-O	0.4800	25.00	0.0	0.0	25.00
Si-Si	0.1600	34.50	0.0	0.0	34.50
Si-O	0.1400	38.70	2.6	3.2	38.70
O-O	0.2500	19.50	0.0	0.0	19.50

Charge Transfer	δ_{ij} (e)	a (nm)	b (nm^{-1})
	0.2170	0.24	80

Triplet	γ_{ijk} (rad^{-2})	θ (rad)
O-Si-O	0.1	1.91
Si-O-Si	0.2	2.48

Element	σ_i *(nm)*	n_i	z_i	$q_i^{\varnothing}$	μ
Na	0.1300	8	+1	+1	4.149
B					
Si	0.1010	8	+4	+4	4.149
O	0.1430	8	-2	-2	5.803

Pair	A_{ij} (10^{-19} J)	ρ_{ij} (nm^{-1})	λ_{ij} (nm)	η_{ij} (nm)	κ_{ij} (nm^{-1})
Na-Na	0.5327	35.00	0.0	0.0	35.00
Na-B					
Na-Si	0.1450	35.00	0.0	0.0	35.00

Na-O	0.1977	35.00	0.0	0.0	35.00
B-B					
B-Si					
B-O					
Si-Si	0.1600	34.50	0.0	0.0	34.50
Si-O	0.1400	38.70	2.6	3.2	38.70
O-O					

Charge Transfer	δ_{ij} (e)	a (nm)	b (nm^{-1})
	0.2170	0.24	80

Triplet	γ_{ijk} (rad^{-2})	θ (rad)
O-Si-O	0.1	1.91
Si-O-Si	0.2	2.48
O-B-O		
B-O-B		
B-O-Si		

Table A-2 Epoxy atom types and non-bonded interactions

Atom Type	*ε(kcal/mol)*	*σ(Å)*	*q*	*Reference*
C, aromatic (CAR)	0.070	3.550		[2]
CT, R_2CH_2	0.066	3.500		[2]
CT, R_3CH	0.066	3.500		[2]
H, aromatic (HAR)	0.030	2.420		[2]
HC, alkane	0.030	2.500		[2]
HC, CH_nOR	0.030	2.500		[2]
O, ester	0.170	3.000		[2]
O, oxirane	0.170	3.120		[2]

CT, 1^{ary} amine	0.066	3.500	[1]
CT, 2^{ary} amine	0.066	3.500	[1]
CT, 3^{ary} amine	0.066	3.500	[1]
HN, 1^{ary} amine	0.010	3.300	[1]
HN, 2^{ary} amine	0.010	3.300	[1]
HC, amine	0.015	2.500	[1]
N20	0.170	3.300	[1]
N1	0.170	3.300	[1]
N21	0.170	3.300	[1]
N0	0.170	3.300	[1]
CT, oxirane	0.066	3.500	[1]
CT, post-reaction	0.066	3.500	[2]
O, hydroxyl	0.170	3.120	[2]
H, hydroxyl	0.010	3.000	[2]

Table A-3 Harmonic bond parameters for epoxy interactions

Bond Type	*k_o(kcal/molÅ2)*	*r_o(Å)*	*Reference*	*Type Assignment*
Car-Car	469.000	1.400	[5]	1
Car-CT	634.000	1.510	[6]	2
Car-Har	367.000	1.080	[5]	3

Car-O	900.000	1.364	[6]	4
CT-CT	310.000	1.526	[2]	5
CT-HC	331.000	1.090	[2]	6
CT-O	214.000	1.327	[4]	7
CT-O$_{epoxy}$	640.000	1.410	[6]	8
CT-O$_{hydoxyl}$	640.000	1.410	[6]	9
CT-N20	382.000	1.448	[1]	10
CT-N21	382.000	1.448	[1]	11
CT-N1	382.000	1.448	[1]	12
CT-N0	382.000	1.448	[1]	13
HN-N20	434.000	1.010	[1]	14
HN-N21	434.000	1.010	[1]	15
HN-N1	434.000	1.010	[1]	16
HO-OH	1106.00	0.960	[6]	17
N*-CTreacted	382.000	1.448	[1]	18

Table A-4 Harmonic angle parameters for epoxy interactions

Angle Type:	*ko(kcal/mol·°)*	*θo (°)*	*Reference*	*Type Assignment*
Car-Car-Car	63.000	120.000	[5]	1
Car-Car-CT	140.00	120.000	[6]	2
Car-Car-Har	35.000	120.000	[5]	3
Car-Car-O	140.00	120.000	[6]	4

Car-CT-Car	80.000	109.500	[6]	5
Car-CT-CT	126.00	114.000	[6]	6
Car-Ct-HC	70.000	109.500	[6]	7
Car-O-CT	83.000	116.900	[4]	8
CT-CT-CT	40.000	109.500	[2]	9
CT-CT-HC	35.000	109.500	[2]	10
CT-CT-HC (amine)	37.500	110.700	[1]	11
CT-CT-O	100.00	109.500	[6]	12
CT-CT-Oepoxy	56.200	109.500	[6]	13
CT-CT-Ohydroxyl	120.00	109.500	[6]	14
CT-CT-N*	110.00	108.500	[1]	15
CT-Oepoxy-CT	35.000	109.500	[1]	16
CT-O-H	35.000	109.500	[1]	17
CT-N*-HN	64.000	109.500	[1]	18
CT-N*-CT	35.000	109.500	[6]	19
HC-CT-O	33.000	107.800	[6]	20
HC-CT-HC	43.600	106.400	[1]	21
HC-CT-HC (amine)	64.000	109.500	[1]	22
HN-N*-HN	63.000	120.000	[1]	23
N*-CT-HC	140.00	120.000	[1]	24

Table A-5 OPLS dihedral angle parameters for epoxy interactions

Dihedral Types	*V1 (kcal/mol)*	*V2*	*V3*	*V4*	*Reference*
C-C-N-C	2.392	-0.674	0.550	0.000	[2]
C-N-C-C	0.416	-0.128	0.695	0.000	[1]
N-C-C-N	4.684	-5.113	0.968	-0.540	[6]
C-O-C-H	0.000	0.000	0.198	0.000	[3]
C-C-C-OS	0.000	0.000	-0.553	0.000	[3]
C-C-O-C	-1.22	-0.126	0.422	0.000	[3]
X-CA-C-X	0.000	0.000	0.000	0.000	[6]
X-CA-CA-X	7.250	0.000	-7.250	0.000	[6]
CA-CA-o-C	3.000	0.000	-3.000	0.000	[6]
O-C-C-Oepoxy	2.159	-2.159	0.000	0.000	[6]
O-C-C-C	0.687	0.139	0.500	-1.326	[6]
H-C-C-O	0.234	0.702	0.000	-0.936	[6]
H-C-O-H	-0.106	0.916	0.174	-0.984	[6]
H-C-CA-CA	0.2310	0.693	0.000	-0.924	[6]
H-C-C-C	0.1500	0.450	0.000	-0.600	[6]
H-C-N-H	0.2000	0.600	0.000	-0.800	[6]
C-C-N-H	-0.303	0.722	0.417	-0.836	[6]
H-C-C-H	0.150	0.450	0.000	-0.600	[6]
H-C-N-C	0.280	0.840	0.000	-1.120	[6]
CA-O-C-H	0.380	1.140	0.000	-1.520	[6]
C-C-C-N	0.797	-0.371	0.674	-1.100	[6]
$\mathrm{O}_{\mathrm{hydroxyl}}$-C-C-N	4.000	-4.000	0.000	0.000	[6]

C-C-O-H	-0.106	0.916	0.174	-0.984	[6]
H-C-C-N	0.280	0.840	0.000	-1.120	[6]

Table A-6 References for parameters used for epoxy interactions

Reference	*Full Citation*
[1]	Rizzo and Jorgenson, J Am Chem Soc V121 N20, 1999
[2]	Supplemental Jorgeson J Amer Chem Soc 1990
[3]	Price, Ostrovsky and Jorgenson, JCC 2001
[4]	Charifson, Hiskey, Pedersen JCC 1990
[5]	Jorgenson and McDonald, Theochem1998 pg 145-55
[6]	Gromacs 4.5.5

Table A-7 Non bonded LJ 12-6 interactions for n-alkane and FCC metals

Species	*ε (kcal/mol)*	*σ (Å)*	*Lattice Parameter (Å)*
Ni	5.65	2.532	3.52
Cu	4.72	2.616	3.61
Ag	4.56	2.955	4.08
Pb	2.93	3.565	4.95
$\mathrm{C_{alkane}}$	0.065975	3.50	--
$\mathrm{H_{alkane}}$	0.030007	2.50	--

Table A-8 Further interactions for n-alkane

Interaction	*Style*	*A*	*B*	*C*	*D*
C-C bond	Harmonic	41.82	1.54		
C-H bond	Harmonic	42	1.09		
C-C-C angle	Harmonic	40	109.5		
C-C-H angle	Harmonic	35	109.5		
H-C-H angle	Harmonic	35	109.5		
C-C-C-C dihedral	OPLS	1.41104	-0.271016	3.14504	0

Table A-9 References for parameters used in alkane and FCC metal interactions

Interaction	*Citation*
Alkane	Jorgensen, W. L. & Tirado-Rives, J. The OPLS potential functions for proteins. Energy minimizations for crystals of cyclic peptides and crambin. Journal of the American Chemical Society 110, 1657-1666 (1988).
FCC Metal LJ	Heinz, H., Vaia, R. A., Farmer, B. L. & Naik, R. R. Accurate Simulation of Surfaces and Interfaces of Face-Centered Cubic Metals Using 12– 6 and 9– 6 Lennard-Jones Potentials. The Journal of Physical Chemistry C 112, 17281-17290 (2008).
Ag, Ni and Cu EAM	SM Foiles, Baskes, M. I. & Daw, M. S., 'Embedded-atom-method functions for the fcc metals Cu, Ag, Au, Ni, Pd, Pt and their alloys', Phys Rev B, 33, 7983 (1986)
Pb EAM	Becker, C. A. Atomistic simulations for engineering: Potentials and challenges. ASM Tools, Models, Databases and Simulation Tools Developed and Needed to Realize the Vision of ICME, (2011). Zhou, X. W., Johnson, R. A. & Wadley, H. N. G., 'Mistfit-energy-increasing dislocations in vapor-deposited CoFe/NiFe multilayers', Phys Rev B, 69, 144113 (2004)

Appendix B. Distribution and change of partial charges of monomers, dimers and trimers

Monomer Partial Charges

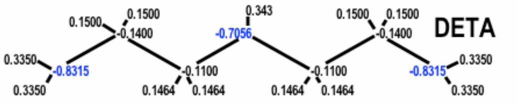

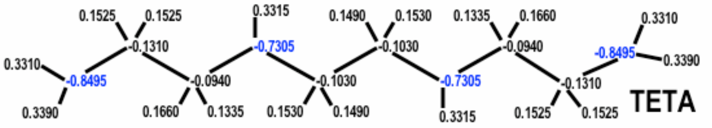

Dimer Charges – Primary amine initial reaction

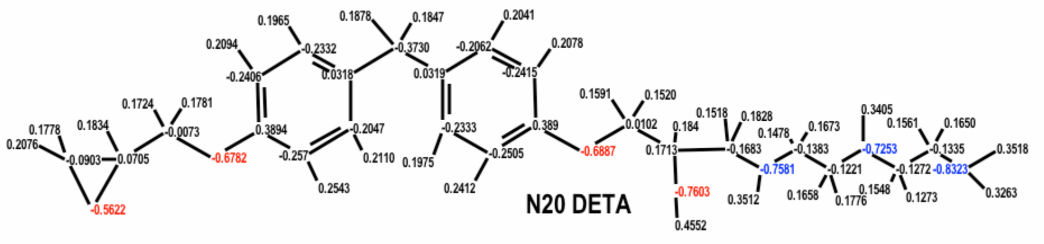

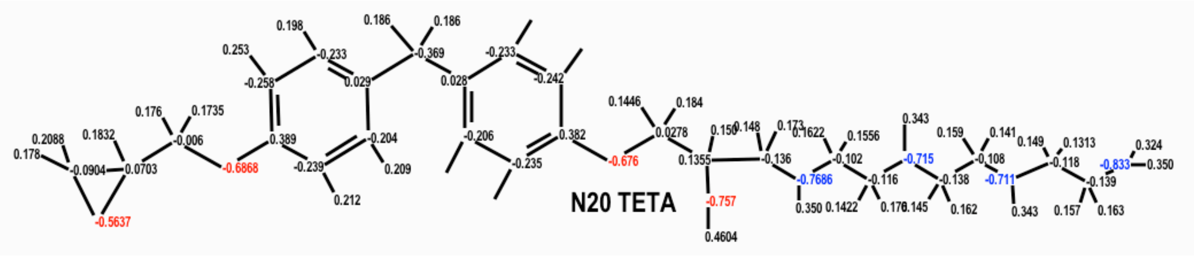

Dimer Charge Change: Primary Amine Initial Reaction

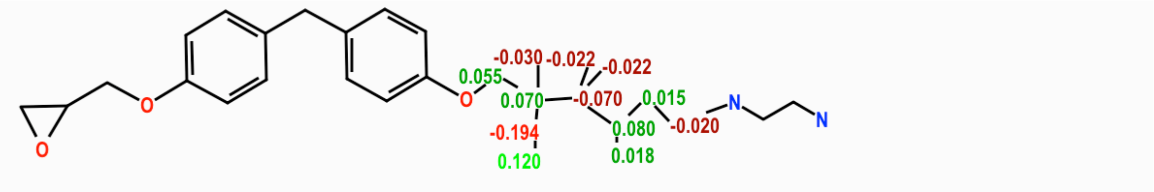

Dimer Charges: Secondary Amine reaction

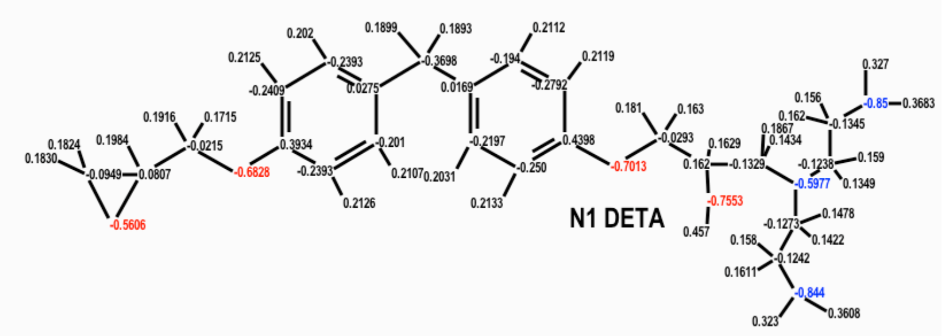

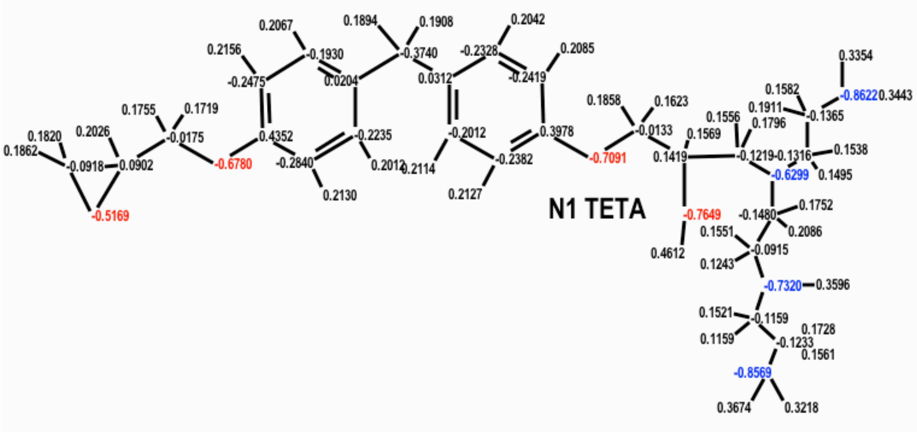

Dimer Charge Changes: Secondary Amine Reaction

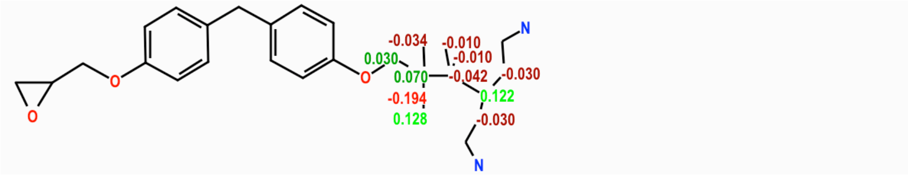

Trimer Charges: Primary Amine Final Reaction

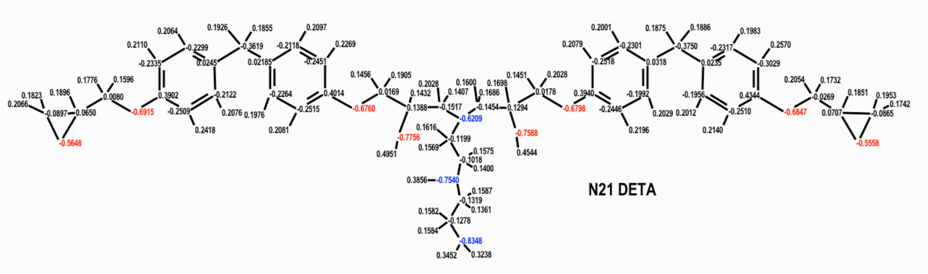

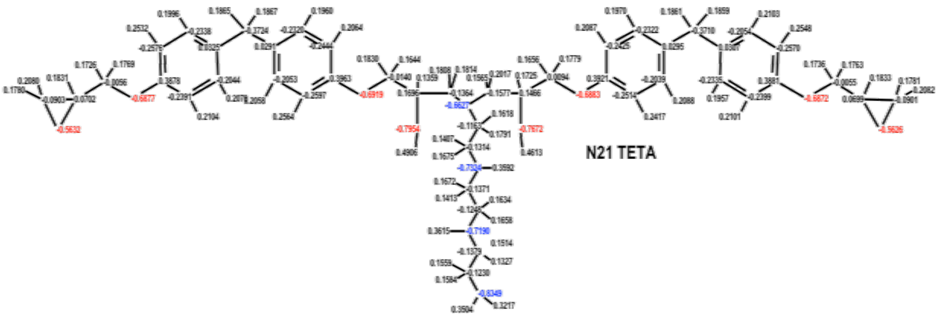

Trimer Charge Changes: Primary Amine Final Reaction

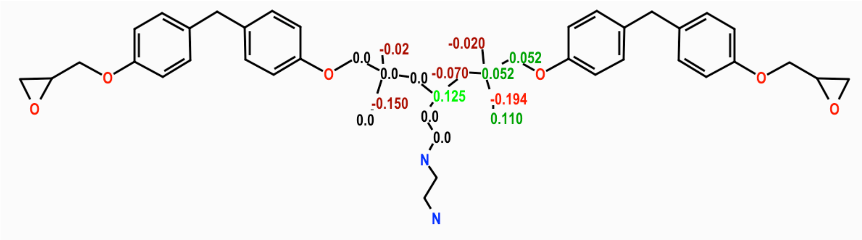

Appendix C: Rules governing topological updates upon reaction in DGEBF-aliphatic amine systems

Primary Amine Initial Reaction

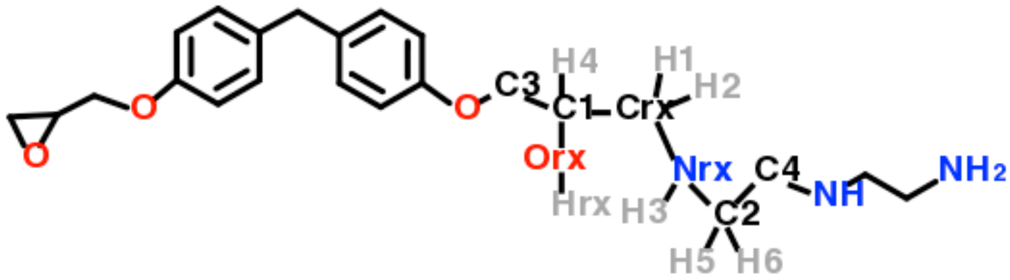

Atoms Modified:

Nrx -> N21,Crx -> CTR, Orx -> OH, Hrx -> HO

Table C-1 Primary Amine Initial Reaction Bonds

Removed	Added	Modified:
Crx- Orx	Crx-Nrx	C1-Orx
Nrx-Hrx	Orx-Hrx	

Table C-2 Primary Amine Initial Reaction Angles

Removed:	Added:
H1-Crx-Orx	C1-Orx-Hrx
H2-Crx-Orx	C1-Crx-Nrx
Crx-Orx-C1	Crx-Nrx-H3
C1-Crx-Orx	Crx-Nrx-C2
C2-Nrx-Hrx	*NRX-CRX-H1
Hrx-Nrx-H3	*NRX-CRX-H2

Table C-3 Primary Amine Initial Reaction Dihedrals

Removed:	Added:
H1-Crx-Orx-C1	Hrx-Orx-C1-C3
H2-Crx-Orx-C1	Hrx-Orx-C1-H4
H4-C1-Orx-Crx	Hrx-Orx-C1-Crx
C3-C1-Crx-Orx	C3-C1-Crx-Nrx
H4-C1-Crx-Orx	H4-C1-Crx-Nrx
C1-Orx-Crx-C1	Orx-C1-Crx-Nrx
Crx-Orx-C1-C3	C1-Crx-Nrx-C2
Hrx-Nrx-C2-H5	C1-Crx-Nrx-H3
Hrx-Nrx-C2-H6	H1-Crx-Nrx-C2

Hrx-Nrx-C2-C4	H1-Crx-Nrx-H3
	H2-Crx-Nrx-C2
	H2-Crx-Nrx-H3

	Crx-Nrx-C2-H5
	Crx-Nrx-C2-H6
	Crx-Nrx-C2-C4

Table C-4 Primary Amine Initial Reaction Charges

Atom	Δq
H1	-0.0220
H2	-0.0220
H3	0.0180
Hrx	0.1200
H4	-0.0300
H5	0.0000
H6	0.0000
Orx	-0.1940
Nrx	0.0800
Crx	-0.0700
C1	0.0700
C2	0.0150
C3	0.0550
C4	-0.0200

Secondary Amine Reaction

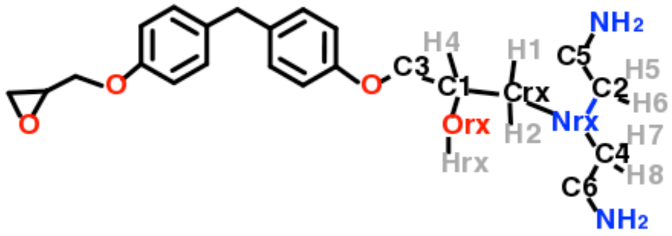

Atoms Modified:

Nrx -> N21,Crx -> CTR, Orx -> OH, Hrx -> HO

Table C-5 Secondary Amine Initial Reaction Bonds

Removed	Added	Modified:
Crx- Orx	Crx-Nrx	C1-Orx
Nrx-Hrx	Orx-Hrx	

Table C-6 Secondary Amine Initial Reaction Angles

Removed:	Added:
H1-Crx-Orx	C1-Orx-Hrx
H2-Crx-Orx	Nrx-Crx-H1
C1-Orx-Crx	Nrx-Crx-H2
C1-Crx-Orx	Crx-Nrx-C2
Hrx-Nrx-C2	Crx-Nrx-C4
C4-Nrx-Hrx	C1-Crx-Nrx

Table C-7 Secondary Amine Initial Reaction Charge Transfer

Atom	Δq:DETA	Δq: TETA	Δq Final
H1	-0.0047	-0.0283	-0.0100
H2	-0.0405	-0.0188	-0.0100
H4	-0.0368	-0.0408	-0.0340
H5	0.0126	0.016	0.0000
H6	0-.0115	-0.0122	0.0000
H7	0.0014	0.0262	0.0000
H8	-0.0042	0.0556	0.0000
Hrx	0.1255	0.1297	0.1280
Nrx	0.1328	0.1066	0.1220
Orx	-0.1890	-0.1986	-0.1940
Crx	-0.053	-0.042	-0.0420
C1	0.0795	0.0594	0.0700
C2	-0.0243	-0.0370	-0.0300
C3	0.008	0.024	0.0300
C4	-0.0298	-0.045	-0.0300
C5	0.0068	-0.0055	0.0000

C6	-0.0315	0.0115	0.0000

Table C-8 Secondary Amine Initial Reaction Dihedrals

Removed:	Added:
H1-Crx-Orx-C1	Hrx-Orx-C1-C3
H2-Crx-Orx-C1	Hrx-Orx-C1-H4
H4-C1-Orx-Crx	Hrx-Orx-C1-Crx
C3-C1-Crx-Orx	C3-C1-Crx-Nrx
H4-C1-Crx-Orx	H4-C1-Crx-Nrx
C1-Orx-Crx-C1	Orx-C1-Crx-Nrx
Crx-Orx-C1-C3	C1-Crx-Nrx-C2
Hrx-Nrx-C2-H5	~~C1-Crx-Nrx-H3~~
Hrx-Nrx-C2-H6	H1-Crx-Nrx-C2
Hrx-Nrx-C4-H7	~~H1-Crx-Nrx-H3~~
Hrx-Nrx-C4-H8	H2-Crx-Nrx-C2
Hrx-Nrx-C2-C5	~~H2-Crx-Nrx-H3~~
Hrx-Nrx-C4-C6	Crx-Nrx-C2-H5
	Crx-Nrx-C4-C6
	C1-Crx-Nrx-C4
	H1-Crx-Nrx-C4
	H2-Crx-Nrx-C4
	~~C1-Crx-Nrx-C4 (duplicate)~~
	C5-C2-Nrx-Crx
	H7-C4-Nrx-Crx
	H8-C4-Nrx-Crx

Primary Amine Final Reaction (H3=Hrx2)

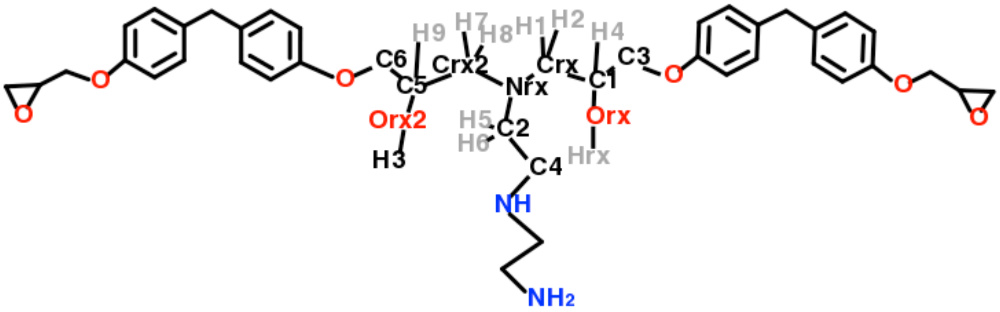

Atoms Modified:

Nrx -> N21,Crx -> CTR, Orx -> OH, Hrx -> HO

Table C-9 Primary Amine Final Reaction Bonds

Removed	Added	Modified:
Crx2- Orx2	Crx2-Nrx	C5-Orx2
Nrx-Hrx2	Orx2-Hrx2	

Table C-10 Primary Amine Final Reaction Angles

Removed:	Added:
Orx2-Crx2-H7	C5-Orx2-Hrx2
Orx2-Crx2-H8	C5-Crx2-Nrx
C5-Orx2-Crx2	Nrx-Crx2-H7
C5-Crx2-Orx2	Nrx-Crx2-H8
Hrx2-Nrx-Crx2	Crx2-Nrx-C2
Hrx2-Nrx-C2	Crx-Nrx-Crx2

Table C-11 Primary Amine Final Reaction Charges

Atom	Δq:DETA	Δq: TETA	Δq Final
C1	+0.0325	0.0641	0.0000
C2	+0.0184	-0.0143	0.0000
C3	0.0076	-0.0418	0.0000
C4	+0.0203	-0.0154	0.0000
C5	+0.0563	0.0641	0.0520
C6	+0.0542	0.0467	0.0520
Crx	+0.0229	-0.0004	0.0000
Crx2	-0.0718	-0.0778	-0.0700
Nrx	+0.1372	0.1059	0.1250
Orx	+0.0015	-0.0384	-0.0150
Orx2	-0.2096	-0.2009	-0.1940
H1	+0.0142	0.0328	0.0000
H2	+0.0082	0.0084	0.0000
H3	+0.0104	0.0302	0.0000
H4	-0.0142	-0.0141	-0.0200
H5	+0.0091	0.0067	0.0000

H6	+0.0013	0.0169	0.0000
H7	+0.0114	-0.0270	-0.0100
H8	+0.0432	0.0103	-0.0100
H9	-0.0545	-0.0252	-0.0200
Hrx	.0008	0.1113	0.1100

Table C-12 Primary Amine Final Reaction Dihedrals

Removed:	Added:
H7-Crx2-Orx2-C5	Hrx2-Orx2-C5-C6
H8-Crx2-Orx2-C5	Hrx2-Orx2-C5-H9
C6-C5-Crx2-Orx2	Hrx2-Orx2-C5-Crx2
H9-C5-Crx2-Orx2	C6-C5-Crx2-Nrx
Crx2-Orx2-C5-C6	H9-C5-Crx2-Nrx
Crx2-Orx2-C5-Crx2	Orx2-C5-Crx2-Nrx
Hrx2-Nrx-C2-H5	C5-Crx2-Nrx-C2
Hrx2-Nrx-C2-H6	C5-Crx2-Nrx-Crx
Hrx2-Nrx-Crx-H1	H7-Crx2-Nrx-C2
Hrx2-Nrx-Crx-H2	H8-Crx2-Nrx-C2
Hrx2-Nrx-C2-C4	H7-Crx2-Nrx-Crx
Hrx2-Nrx-Crx-C1	H8-Crx2-Nrx-Crx
	Crx2-Nrx-C2-H5
	Crx2-Nrx-C2-H6
	Crx2-Nrx-C2-C4
	H1-Crx-Nrx-Crx2
	H2-Crx-Nrx-Crx2